Efficient Terahertz Photoconductive Source

A Thesis
Presented to
The Academic Faculty

by

Joong Hyun Kim

In Partial Fulfillment
Of the Requirements for the Degree
Doctor of Philosophy in the
School of Electrical and Computer
Engineering

Georgia Institute of Technology
December 2008

Efficient Terahertz Photoconductive Source

Approved by:

Dr. Stephen E. Ralph, Advisor
School of Electrical and Computer Engineering
Georgia Institute of Technology

Dr. David Citrin
School of Electrical and Computer Engineering
Georgia Institute of Technology

Dr. John Cressler
School of Electrical and Computer Engineering
Georgia Institute of Technology

Dr. Douglas R. Denison
Signature Technology Laboratory
Georgia Tech Research Institute

Dr. Saibal Mukhopadhyay
School of Electrical and Computer Engineering
Georgia Institute of Technology

Date Approved: Oct. 9th, 2008

ACKNOWLEDGEMENT

First and foremost, I thank Dr. Stephen E Ralph for the opportunity to work in this unique area of research. I believe that his advice, encouragement and time-consuming effort has made it possible to complete this work. I also would like to thank Dr. David Citrin, Dr. Douglas Denison, and Dr. Michael Knotts for THz project contributions and many illuminating discussions.

I cannot sufficiently thank all of the past and present group members of the Ultrafast Optical Science laboratory at Georgia Tech for their encouragement and technical support. The members include Katen Patel, Jeffery Lillie, Shannon Madison, Arup Polley, and more. I especially would like to acknowledge Arup Polley for his contributions to the Hydrodynamic model for THz analysis as well as many discussions regarding this project. I thank Shannon Madion for their assistance with the fabrication of devices. I also would like to acknowledge Dr. Cressler and Kurt Moen for their help with temperature dependent measurements of THz sources.

A large portion of this work is made possible due to financial support from the Georgia Tech Research Institute.

For My Wife Sun Min and Daughter Juha

LIST OF TABLES

LIST OF TABLES

LIST OF FIGURES

LIST OF ACRONYMS

HDM	Hydrodynamic Model
TEF	Trap Enhanced Field Effect
THz	Terahertz
FWHM	Full Width at Half Maximum
SHG	Second Harmonic Generation
PC	Photoconductive
FROG	Frequency Resolved Optical Gating
WKB	Wentzel Kramers Brilouin
TE	Thermionic emission
TFE	Thermionic Field Emission
FE	Field Emission

SUMMARY

Optical excitation of a biased photoconductor is one of the oldest methods for the generation of electromagnetic waves. Upon optical excitation, the existing field accelerates generated carriers to produce an electromagnetic wave. With the availability of sub-picosecond pulsed lasers, the photoconductive source spectrum is extended to the THz regime. The inherent advantages of room-temperature operation, simple geometries, and a broadband spectrum make the THz photoconductive source a popular THz spectroscopic tool. Recently, the THz source has become more attractive with increased interest in security related applications. Unfortunately, the THz photoconductive source has operated at a power level in the order of hundreds of nW. In addition, the conversion of optical to THz energy has remained extremely low.

One of the most efficient THz photoconductive sources is a trap-enhanced field (TEF) effect source. The field is measured to contain more than 90% of the total DC bias within the first 5 μm of an 80 μm gap between the electrodes. Therefore, with only a modest bias, the field strength can reach more than tens of kV/cm. The overall THz power, however, has remained low, due to rapid saturation. To date, there has been a limited understanding of the TEF effect. In this thesis, a detailed experimental investigation of TEF effect current transport and annealing dependent TEF field distribution is presented.

A spatially extended line excitation is introduced to effectively reduce the screening effect while still exploiting the TEF region to maintain high efficiency and

reach the μW regime. The record efficiency of 0.07% reached by this method is demonstrated. An experimental demonstration with a numerical analysis of the line excitation is presented. The spectral analysis of both a point and a line excitation demonstrate that the line excitation spectrum is not only comparable to that of the point excitation, but also extends the range of useful lower frequency content. To further improve the THz efficiency, the line excitation THz array is investigated.

CHAPTER 1: Introduction

The electromagnetic spectrum from 100 GHz to 10 THz is often referred to as the THz gap sandwiched between electronics and optics. The major bottleneck in a THz system is the lack of an efficient room-temperature-operated THz source. There have been many applications proposed in different fields such as space technology [1], the biomedical [2], the imaging [3], impulse ranging [4], and so forth. With the recent increased risk of terrorist threats, the THz spectrum has also attracted the attention of many government and military agencies for the capability of detecting hazardous material. The THz gap is an important bridge between electronics and photonics for obvious reasons. Terahertz pulse imaging (TPI) is an imaging technique based on THz pulse radiation generated and detected using all-optical effects. THz imaging at an early stage is difficult to compete with mature techniques such as X-ray, computed tomography, magnetic resonance imaging (MRI), and ultrasound, but THz provides information that is unique to its spectral range.

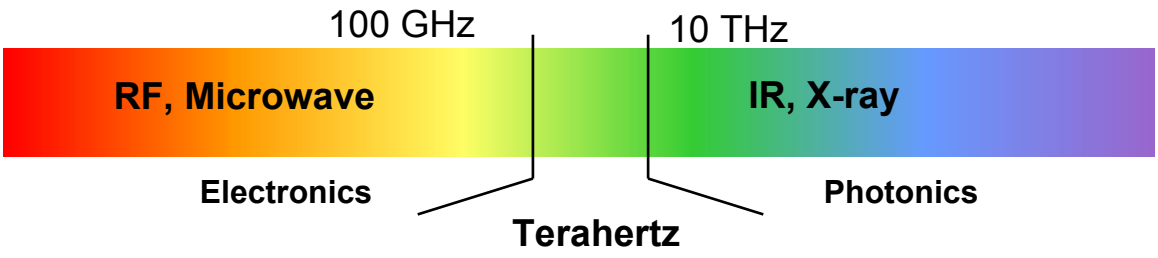

Figure 1. Terahertz (THz) gap spectrum.

1.1. Challenges in THz Sources

While many benefits are realized from the THz spectrum, challenges remain in developing an efficient, compact, and affordable THz source. Below the THz gap, there are commercially-available devices running above 70-110 GHz. Heterojunction bipolar transistors (HBTs), bipolar junction transistors (BJTs), field-effect transistors (FETs), and transferred electron (Gunn) devices are included in this region. The maximum operating frequency of these devices primarily depends on characteristic distances such as base width, gate length, and active region size, which is why they are also called transit-time devices. To achieve higher frequencies, the electronic transit device requires a narrow characteristic distance and high electric field strength in order to accelerate carriers. With narrow distances, even small biases can quickly lead to breakdown effects, limiting the output power of the electronic device. Above the THz gap, transition devices, such as near-infrared diodes and light emitting diodes (LEDs), face other problems. The operation of theses devices depends on the transition between energy states. The energy at 1 THz, 4 meV, is far below the room-temperature thermal energy, 26 meV. As a result, a population inversion cannot occur without cryogenic cooling or an energy level high above the ground state. [1]

There are several successful high-power THz sources available such as the quantum cascade laser and the free electron laser. The quantum cascade laser has the advantage of being compact and not requiring the use of an additional pulsed oscillator. A pulsed output of 248 mW and a continuous wave operation (CW) of 138 mW have been reported with the peak spectrum at ~4.4 THz [5]. Quantum cascade lasers, however, require low-temperature operation at THz frequency in order to subdue thermal noise.

The quantum cascade laser yields high oscillation frequencies compared to other RF sources, but low THz frequencies (~0.1-2 THz) have been difficult to reach. A free electron laser has been reported as generating on the order of hundreds of watts [6]. However, these sources exist in only a handful of research labs due to the need for an expensive accelerator.

1.2. Thesis Problem Statement

The lack of efficient compact THz sources have been identified as the major limitation of an affordable THz system. The THz PC source has the attractive advantages of room-temperature operation and simple geometry. The broadband spectrum of the THz PC source has also been an important feature for THz spectroscopic study. The THz PC source has operated mostly at ~nW regime due to screening effects. Moving PC sources to higher power often requires a high-voltage power supply, high magnetic field magnet, and water-cooling source in order to reach high power and efficiency, adding complexity to a THz system.

The objective of the proposed research is to develop efficient photoconductive THz sources. The primary focuses are a) overcoming screening limitations, b) understanding the trap-enhanced field effect, and c) investigating limiting factors in the TEF THz array.

1.3. Thesis Outline

Chapter 1 introduces a brief explanation of the challenges in THz technology. Chapter 2 discusses the origin and history of the problems relating to different THz sources. Specifically, different types of THz photoconductive (PC) sources, their

respective methods of generation, and their advantages and disadvantages are discussed. Chapter 3 primarily focuses on ultrafast optical issues, including the generation and diagnosis of femto-second pulses. In Chapter 4, the trap-enhanced field effect is closely investigated. Many experimental observations are drawn from annealing dependent field distributions as well as from the analysis of the current-voltage response. Sentaurus Device simulation results are included in order to explain the contact behavior in TEF THz sources. Chapter 5 presents an analysis of spatially extended line excitation performance as compared to a typical point excitation. Chapter 6 addresses the spectral analysis of both line and point excitation geometry. The low frequency content extension of the line excitation is explained. Chapter 7 presents an analysis of the performance of a THz line excitation array. The scaling of the THz array and its limitations are investigated.

CHAPTER 2: THz Photoconductive Source

This chapter introduces THz photoconductive sources. The chapter begins with basic descriptions and definitions, followed by a brief review of the various types of THz photoconductive (PC) sources. The chapter introduces the basic operation of different types of photoconductive sources and their mechanisms. For detailed descriptions, references are cited. Finally, major limitations in THz emission power and efficiency are discussed.

2.1. Terahertz Photoconductive Sources

The THz PC source is one of the oldest methods by which THz radiation has been generated. Its advantages include room-temperature operation, compactness, simple geometry, and broadband output spectrum. These advantages are also the reason why the THz PC source has been a common choice for commercial systems. As the name implies, the THz PC source utilizes the photoconductivity of semiconductor materials. A typical THz PC source consists of two coplanar metal electrodes that are deposited on semiconductors such as GaAs, InP, InAs, or Si. The above-band-gap sub-picosecond optical pulse excitation generates carriers that are accelerated by internally or externally supplied electric fields, subsequently generating THz radiation. Figure 2 shows a typical geometry of THz PC source and an excitation pulse. Recently, a readily-available

commercial Ti:Sapphire oscillator has facilitated THz PC generation in many research labs. Since the primary radiation mechanism is the transient photocurrent, the THz power is principally supplied by the electric field. Therefore, it is not intrinsically limited by the incident optical power [7]. Consequently, the efficiency of a THz system strongly depends upon the electric field strength. A hyper-hemispherical silicon lens is attached to the back of the substrate to collimate the THz beam and couple it into free space. The silicon lens is reported to cause the frequency-dependence of the radiation [8].

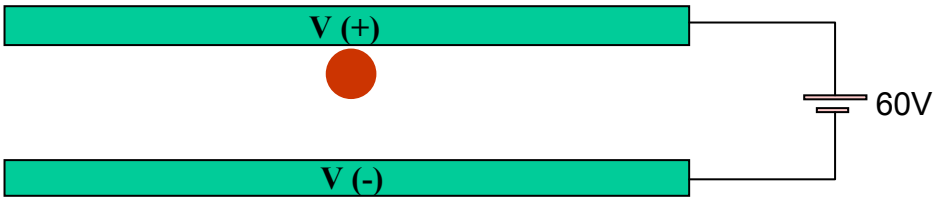

Figure 2. THz PC source geometry: Parallel metal electrodes biased by DC power supply.

The first demonstration of transient current radiation dates back to the Hertz experiment; therefore, it is often referred to as a Hertzian dipole. More recently, the first successful demonstration of THz radiation by optical gating was reported by Auston, et al [9]. Figure 3 shows a typical temporal pulse shape and the spectrum from THz PC source.

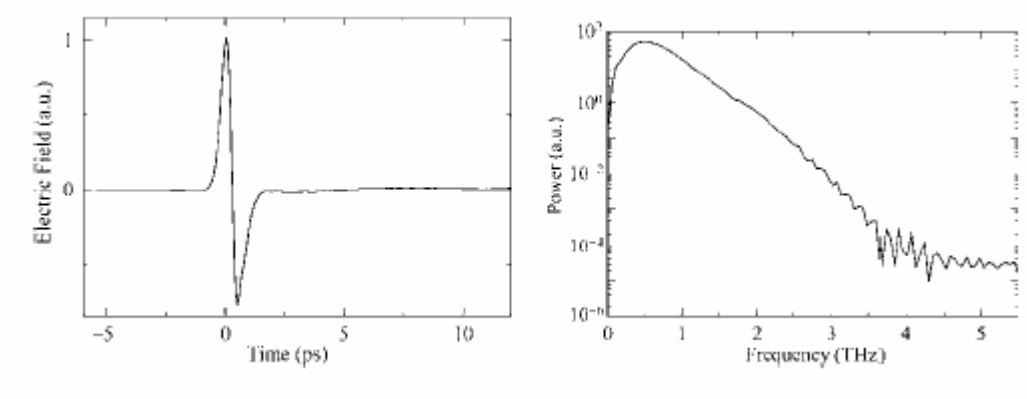

Figure 3. Typical THz pulse (left) and spectrum (right) of a PC THz source [10].

2.2. THz Photoconductive Switches and Solutions

2.2.1. Large Aperture THz Sources

The first optically-gated structure for a THz PC source is the large aperture source demonstrated by Auston et al. [9]. The large aperture source consists of two parallel electrodes with gap ranging from ~0.5 mm to 3 cm (electrode separation > λ) [31, 11]. As described in the previous section, an unfocused large excitation beam, typically occupying the whole gap, is advantageous because of the negligible influence of the space-charge screening effects. The large aperture source can avoid the laser damage threshold of a high-intensity amplified laser by scaling the electrode gap. As a result, large aperture sources are able to generate a high THz power due to the use of amplified lasers [33]. On the other hand, in order to reach a high field on the order of ~kV/cm, a high-voltage DC power supply is required. Higher efficiencies have been reported, but in these cases a water-cooling source was required [11]. The amplified laser and water-cooling add complexity to a THz system, raising overall system cost.

The dependence of THz power on bias voltages is studied by Benicewicz and Taylor, using an InP large aperture source to demonstrate the direct proportionality of the peak THz radiation on the bias field up to 12 kV/cm [34]. This result indicates that the high-field mobility effect does not influence the peak THz power.

2.2.2. Trap-Enhanced Field Effect Photoconductive Sources

The trap enhanced field effect originates in the formation of a highly condensed field distribution near the anode of a biased pair of coplanar metal lines that are fabricated on semi-insulating material [12]. The DC bias of electrodes increases the electron density at the anode. As a result, the larger capture cross-section of electrons vs. holes in EL2 defects leads to the accumulation of a large number of uncompensated holes, generating the TEF effect. It has been estimated that 90 % of the total biased field resides in the first 10 μm adjoining the anode. One of the most efficient electrode configurations uses the TEF effect, which develops a field strength in excess of 200kV/cm with modest applied voltages of ~60V.

However, even these sources are limited to a few hundred nWs of THz power when using the spot excitation of a conventional ~82 MHz repetition rate femto-second source, corresponding to an efficiency of ~0.002 % that is impeded by severe space-charge screening, saturating at a lower optical excitation than other PC THz sources [7].

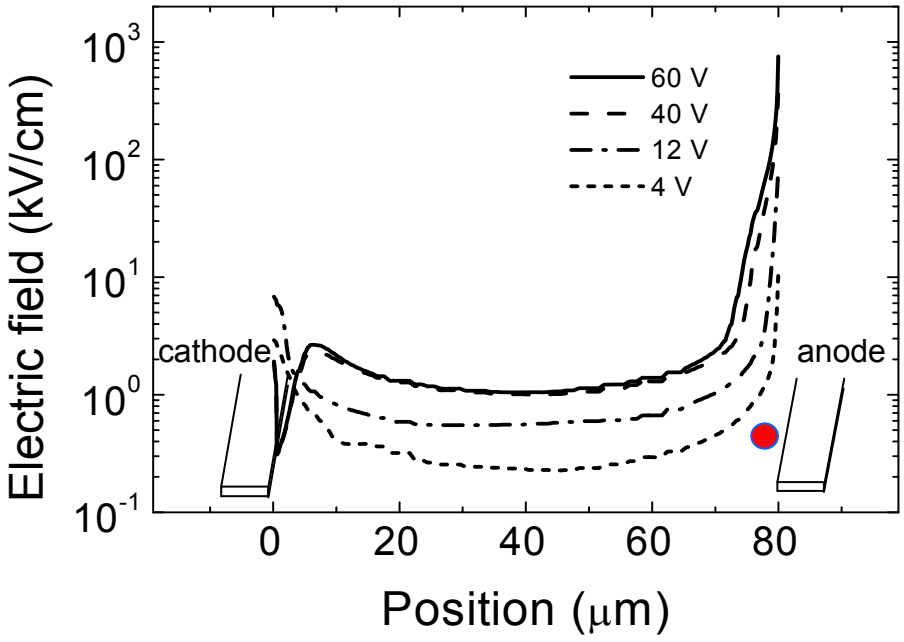

Figure 4. Optical excitation geometries of point excitation and electrodes overlaid on calculated field strength across the electrodes for 60 V bias.

2.2.3. Microstructured Large-Area Photoconductor

The microstructured Large-area photoconductora with an interdigitated design demonstrates high-intensity THz radiation [13,14]. The THz PC sources are arranged in a linear array geometry with 5-10 μm separation between electrodes to produce constructive interference. With the small separation, a bias of 30V can generate ~kV/cm field strength. To prevent deconstructive interference, every other gap is covered with opaque material so only the electric fields with the same direction contribute to the THz radiation. Inevitably, the opaque material reflects the optical incident energy, resulting in less than 50% of the surface area contributes to the THz radiation. A conversion efficiency of 0.025% has been reported. [13]

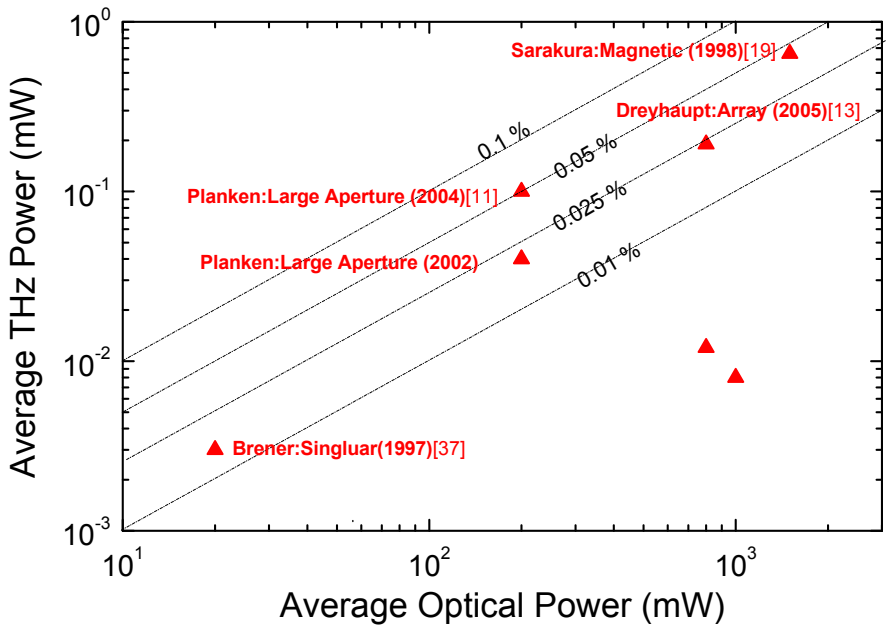

Figure 5. THz photoconductive efficiency record; optical excitation power, THz power, years published, methods, and the first author of the record.

2.2.4. Built in field

Fermi level pinning at the air/semiconductor interface cause band banding that creates a charge depletion region reported to generate the THz radiation Upon ultrafast excitation on the surface [15]. Naturally, the radiation strength and polarity have a strong angular dependence with respect to the optical excitations. A photo-Dember field generated by the differences in the diffusivity of carriers upon optical excitation at the semiconductor surface is also a suggested source of THz radiation [16]. Different materials including GaAs, InP, and InAs, are investigated for this mechanism. InAs exhibited the best performance due to its high mobility.

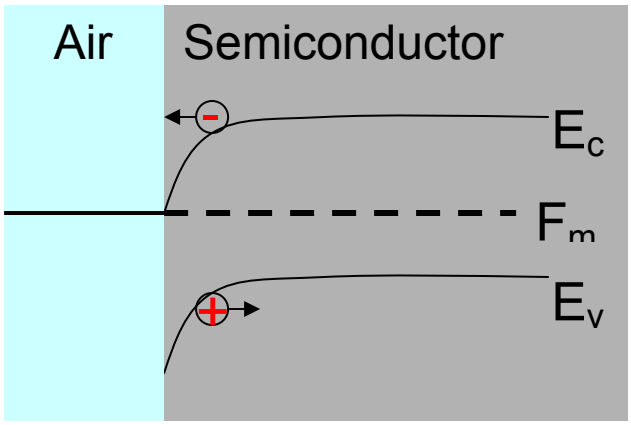

Figure 6. Fermi pinning effect at Air/Semiconductor interface

The PIN structure contains a thin insulating layer and heavily doped region that creates a built-in depletion region. Small DC biases can produce high electric field strengths in the depletion region. The THz generation mechanism is similar to other PC sources in that the ultrafast optical excitations generate carriers that are accelerated by electric field to radiate THz [17]. One of the largest spectrums, 0.1 THz to 70 THz, has been reported using PIN structure [18].

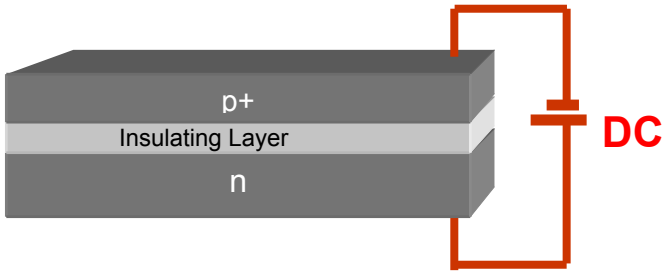

Figure 7. PIN Structure THz source

2.2.5. Magnetic Field Enhancement

Magnetic field-enhanced devices have produced one of the highest THz powers yet (~650 μW) reported [19]. The THz generation mechanism is the surface depletion region excitation described in section 2.4.4. Magnetic field enhancement is the result of

the optimization of transient current direction caused by the Lorentz force, as opposed to the enhancement due to accelerating field strength. The spectrum is quite similar to other large aperture sources [20].

2.2.6. Other THz PC Sources with a high repetition rate laser

There are several other PC sources reporting μW output powers with a high repetition rate laser. Y. Cai investigated the effects of different geometries with a 5 μm separation between electrodes. He reported that a sharp triangular tip with an enhanced electric field generated 3 μW of average THz power with 20 mW of the optical excitation [21]. Darmo et al reported 7 μW of THz power from an intracavity biased Lt-GaAs emitter grown on a Bragg mirror with the optical excitation of 900 mW [22]. Andrew et al reported 30 μW at 170 mW pump power using line focus [23].

2.2.7. THz- Time Domain Spectroscopy (THz-TDS)

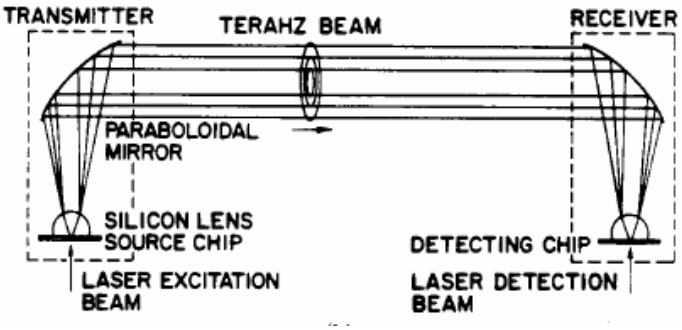

Figure 8. THz Time-Domain Spectroscopy experimental set-up [24].

THz-TDS is the most dominant application using the THz PC sources. Figure 8 illustrate the procedures. Freely propagating THz pulses generated by the THz PC sources are focused onto a sample using a paraboloidal mirror. The transmitted pulses are collected in the same manner using the photoconductive receiver. The collected

information including the phase and intensity is compared with free space data to determine absorption characteristics. The THz-TDS measures the field amplified and delayed itself, and it is possible to extract the complex dielectric constant with a simple numerical calculation. The THz-TDS has progressed since it was first introduced [24]. The examination of water vapor, water mixture, and molecular vapor have been recorded. Far IR properties of semiconductors, dielectrics, and other compounds have also been studied using this method in order to identify their unique signature in the THz regime. More recent research includes plasma oscillations, utilizing information such as phonon frequency and radiating phonon decay time as revealed by the THz-TDS. .

2.2.8. Summary

The room-temperature operation and simple geometry of the THz PC source is well suited for practical THz systems. Large aperture sources often require THz source-water-cooling, amplified lasers, and high voltage DC power supplies, which impose additional restrictions on potential compact THz systems. The magnetic field enhanced source also faces similar challenges. On the other hand, the TEF THz source has the inherent advantage of generating a high field with only modest biases and without additional cooling or a high DC voltage supply. The TEF THz source has the best chance of reaching high efficiency.

2.3. Challenges and Limitations in THz Photoconductive Sources

2.3.1. THz Photoconductive Radiation Process

An electromagnetic radiation can typically be derived directly by coupling Maxwell-Faraday equations:

$$\nabla \times E_{THz} = -\frac{\partial B}{\partial t} \tag{1}$$

$$\nabla \times H_{THz} = J(t) - \frac{\partial D}{\partial t} = J(t) - \frac{\partial(\varepsilon(t)E_{THz})}{\partial t} \tag{2}$$

In our case, it is extremely difficult, if possible at all, to solve analytically directly. Some numerical analysis is required to estimate the THz radiation. This section briefly discusses the basic idea of the THz photoconductive source.

The THz radiation is a result of transient photocurrent in semi-conductor. Transient time current is as followed:

$$J(t) = \sigma(t)E = q\mu_n(t)n \cdot E(t) \tag{3}$$

The mobility, and the conductivity, is no longer constant. It is depends on the electrical field strength. It is reasonable to assume that the contribution from holes is not significant due to the substantial lower mobility of holes vs. electrons. Only electrons are considered in following discussion. The time-dependent carrier density is determined by

$$\frac{\partial n}{\partial t} = -\frac{n}{\tau_n} + G_n(t) \tag{4}$$

where $G_n(t)$ is the injected optical carriers, τ_n is carrier lifetime. The carrier lifetime is typically much longer than the temporal profile of the optical pulse width. Upon excitation, carriers are generated. The absorption depth is in the order of ~1 μm. Then, they are accelerated according to the instantaneous electrical field strength.

Time dependent average velocity ν(t) can be calculated from Drude-Lorentz model is

$$\frac{\partial v(t)}{\partial t} = -\frac{v(t)}{\tau_s} + \frac{q}{m^*} E(t) \tag{5}$$

where E(t) is the field that the carriers experience, m* is the effective mass and τ_s is the scattering rate. We can add additional restriction on the electrical field strength by adding the space charge screening term:

$$E(t) = E_{bias} - \eta_{sc} \frac{P_{sc}}{\varepsilon} \tag{6}$$

$$\frac{\partial P_{sc}}{dt} = -\frac{P_{sc}}{\tau_r} + J(t) \tag{7}$$

where τ_r = recombination lifetime, by coupling above equations,

$$\frac{\partial v^2(t)}{\partial t^2} + \frac{v(t)}{\tau_s} = \frac{q \eta_{sc} P_{sc}}{m^* \varepsilon \tau_r} \tag{8}$$

This is rather simple one-dimensional analysis. Many complications arise from semi-conductor air interface, field dependent mobility, scattering rates, so forth. In addition, other limiting factors such as screening effects and field distribution in the THz source needs to be considered as well.

2.3.2. THz TEF PC source structure

A practical THz PC source must be both compact and efficient. Figure 9 shows a detailed schematic of a TEF PC source. A sub-picosecond pulse is focused down to a small spot in order to excite the anode of the TEF PC source. When carriers are accelerated, the resulting transient current generates THz radiation. THz emission is isotropic, especially for a circular point excitation. The details of optical excitation sources and geometries are discussed in later chapters of this document. A silicon lens is used for two purposes: to match the index of the THz source and to collimate the THz radiation. Therefore, the optical excitation geometry determines the structure of the silicon lens.

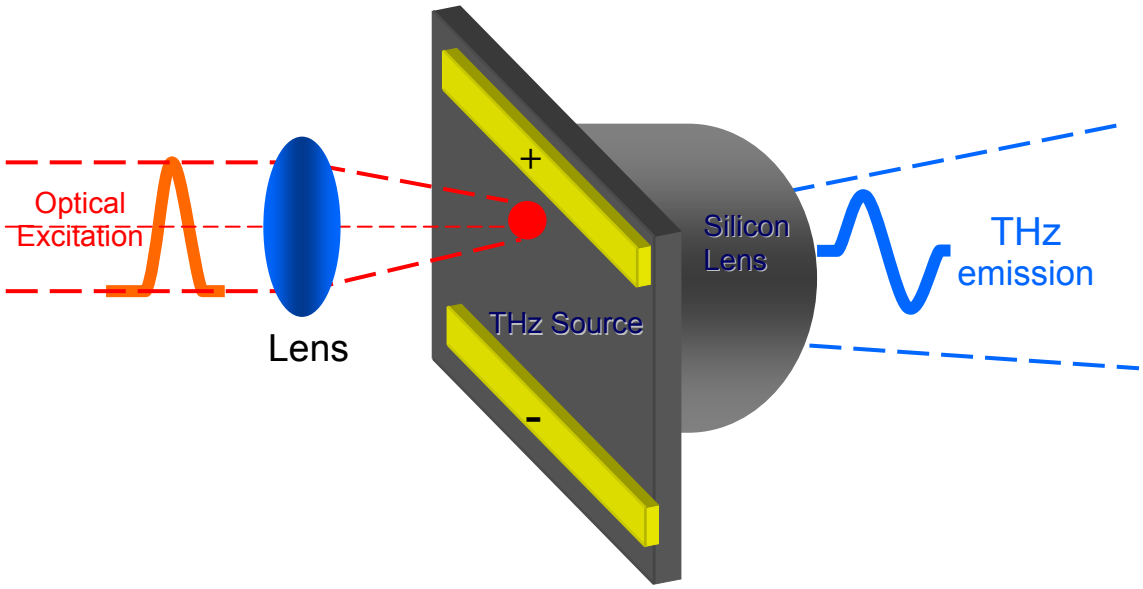

Figure 9. THz photoconductive source excitation schematics

2.3.3. Expected THz power: Larmor Result

The radiated power from an accelerated charge is proportional to the square of the acceleration, as given by the Larmor Result [25].

$$P_{THz} = \frac{\mu_0 n^2 \langle a \rangle^2}{6\pi c^3} \tag{3.9}$$

It can be extended to describe an ensemble of charge carriers by using the ensemble acceleration, $\langle a \rangle$, and the number of charge carriers, n, when the charge volume is small with respect to the radiated wavelengths; thus, $P_{THz} \propto n^2 \langle a \rangle^2$. Therefore, the THz radiation energy is principally supplied by the DC power supply, and the optical-to-THz power efficiency rises with the increasing optical excitation when saturation is not in effect. In low-power excitations (< 1 mW), the THz radiation follows a square dependence, consistent with the Larmor result; however, all photoconductive generation techniques exhibit saturation, yielding substantially lower efficiencies at high optical excitation.

2.4. Power Limitation: Space-Charge & Radiation Screening

2.4.1. Space-Charge Screening

The most significant limiting mechanism of the THz radiation is the screening effect, which directly influences the effective field strength, causing saturation. The space-charge electric field is formed by the separation of photo-generated carriers under the influence of a biased electric field. The direction of the space-charge field is opposite that of the DC bias, which effectively reduces the overall biased field strength. Therefore,

the space-charge screening is closely related to the incident optical carrier density and the photo-generated carriers. The reduced field decreases the carrier acceleration, generating less THz peak power [26,27]. The temporal shape of the THz pulse shifts from unipolar to bipolar behavior because of the space-charge screening at high excitation densities. Under certain conditions, the space-charge field causes collective plasma oscillation, shifting the spectral content of the THz radiation to higher plasma oscillation frequencies [28,29].

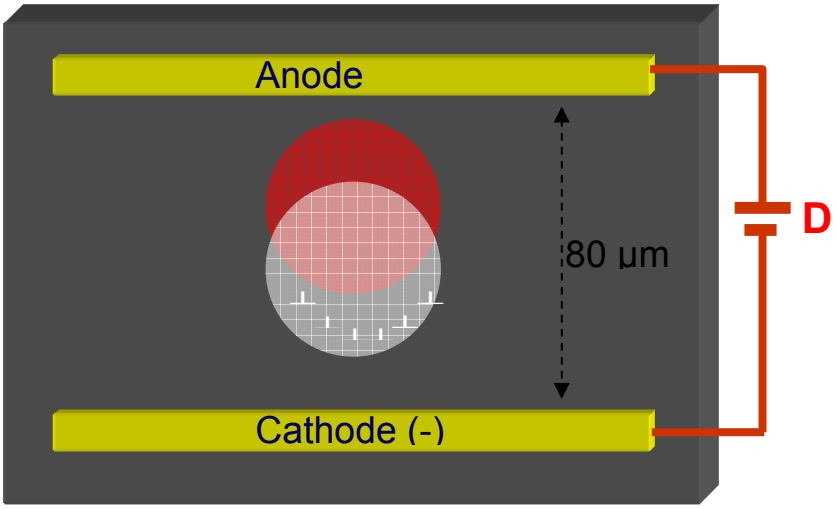

Figure 10. Illustration of space charge screening.

2.4.2. Radiation Screening

Radiation screening is another type of screening caused by the reverse action of the generated THz radiation. The polarity of the THz radiation is opposite that of the DC bias field, effectively screening the biased field. The radiation screening has been well studied using a large aperture THz source, since the large aperture uses a large unfocused excitation for which space-charge screening is negligible [30].In fact, the saturation property of THz power with respect to the optical excitation was first reported by J.T. Darrow, et al, using a large aperture source [31]. The saturation properties of different

materials such as semi-insulating GaAs, low-temperature grown GaAs, InP, and radiation damaged silicon-on-sapphire have also been studied [32,33].

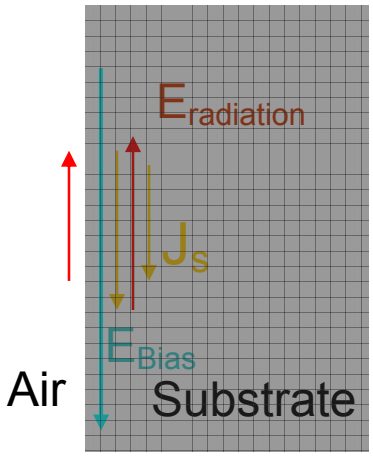

Figure 11. Illustration of Radiation screening.

The detailed saturation behavior of the THz large aperture source with respect to DC bias has been reported using InP and GaAs large aperture sources [34]. The saturation point primarily depends upon the optical excitation power and is independent of bias field strength. There is little or no angular dependence of incident optical power on THz generation, which confirms that the THz generation mechanism in large aperture sources is primarily the transient current and not the optical rectification process.

CHAPTER 3: Optical Excitation

The THz photoconductive emission setup can be divided largely into two parts: the optical excitation and the material response. The absorbed optical carriers directly influence total radiated power and efficiency. A temporal profile of the optical excitation with the material response determines the spectrum of the emission. As described previously, a high optical excitation density can limit the total average THz radiation power. Therefore, an accurate assessment and analysis of ultrafast pulsed excitation is critical to understanding THz efficiency as well as improving the power and efficiency. Photoconductive switches are not used exclusively for THz generation. They are often used to generate broadband microwave emission. The ultrafast sub-picosecond pulse excitation is the means by which to expand the spectrum into THz regime. While THz photoconductive radiation has been demonstrated in past, the availability of commercial ultrafast systems has facilitated the use THz systems in many research labs. This chapter introduces a description of an ultrafast pulsed-laser system and an autocorrelaton ultrafast pulse measurement technique used in all THz experiments included in this document.

3.1. Ultrafast Pulse Generation

An ultrafast pulse is typically defined as a pulse duration Δt of picosecond or shorter pulse duration. The pulse duration Δt is a full-width at half maximum of the

intensity profile. These types of lasers usually operate at a high repetition rate depending on the length of the cavity. We will define a pulse as followed:

$$\widetilde{E}(t) = \hat{e}E(t)e^{j(k_0 z - \omega_0 t)} \tag{10}$$

where $E(t)$ is the pulse complex envelope, $\hat{e}$ is arbitrary unit polarization, ω_0 is the carrier frequency, and k_0 is the freespace wavevector. The pulse envelope typically fits well with either Gaussian or hyperbolic secant, which is an important information for an autocorrelation system.

Titanium doped sapphire is a crystalline material that has an absorption spectrum between 400 to 600 nm and a fluorescent output spectrum from around 600 nm to 1100 nm, with a peak gain around 800 nm. This is the most widely used gain medium to generate ultrafast pulses. The vibrational broadening of the electronic state of Ti^{+3} ion allows for the tunability of this type of laser. The Ti:Sapphire laser is often referred to as a Kerr Lensed Mode-locked laser because the Kerr self-focusing effect leads to an intensity dependent index of refraction. In the past, an Argon laser has provided necessary pump, but the Nd:YVO_4 laser has proven to be a more efficient source of pump at ~532nm. The Ti:Sapphire laser does have some tunability within the gain medium output spectrum range, but its efficiency falls as the wavelength deviates from the peak wavelength of 800 nm. An acousto-optic modulator provides a passive mode-locking system at ~82 MHz.

The diode laser directly pumps a lasing medium, Nd:YVO_4. The resulting 1064 nm energy is converted through a frequency doubling crystal, LBO. A major advantage of the LBO crystal is its non-critical phase matching condition that allows collinear propagation of the frequency double beam and the fundamental beam. In order to

achieve the high conversion efficiency of the LBO crystal, the crystal temperature needs to be held at an optimum value, achieved through action feedback to the laser controller. All experiment data presented in this document have been produced using a Spectra-Physics (now Newport) Millenia Xs diode pumped Nd:YVO_4 laser with Spectra-Physics Tsunami Ti:Sapphire laser .

3.2. Ultrafast Pulse Measurement

3.2.1. Intensity Cross Autocorrelation

A typical method of temporal measurement of the pulse width is a pump-probe method where the gating shorter probe pulse is already known. If no shorter pulse exists, then a pump-probe method is no longer an option, which is often a case for the ultrafast system. One of the most popular methods for ultrafast pulse measurement is an autocorrelation. Without a known shorter gating pulse, the autocorrelation uses the input pulse itself to generate an autocorrelated signal. A nonlinear interaction of second-harmonic generation is the key to an intensity autocorrelation. This nonlinear interaction is short enough that contribution to autocorrelated signal is negligible. The simplest form of autocorrelation is the intensity autocorrelation shown in Figure 12. A 50-50 beam splitter sends two pulses into a Michael interferometric setup with one optical path varied to provide temporal delay. A lens focuses both pulses inside of a SHG crystal that generates an autocorrelated signal:

$$\widetilde{E}_{SHG}(t,\tau) \propto \widetilde{E}(t)\widetilde{E}(t-\tau) \tag{3.11}$$

where $\widetilde{E}_{SHG}(t,\tau)$ is the second-harmonic field and τ is temporal delay. The autocorrelation utilizes SHG crystals, such as BBO and KDP, to convert the wavelength of 800 nm to 400 nm. A photomultiplier tube (PMT) signal measures intensity:

$$I_{SHG}(t,\tau) = \left|\widetilde{E}_{SHG}(t,\tau)\right|^2 \tag{12}$$

Therefore, the autocorrelation signal is

$$A^{(2)}(\tau) = \int_{-\infty}^{\infty} I(t)I(t-\tau)dt \tag{13}$$

where $A^{(2)}(\tau)$ is the autocorrelated signal and $I(t)$ is the intensity of the pulse being measured. In order to separate the autocorrelated signal from the fundamental beams, a blue passing colored filter is used to block the fundamental beams. Figure 13 shows the measured auto-correlated signal and the spectrum with a $\text{sech}^2(x)$ fit. The obtained autocorrelated signal is then de-convolved to estimate the temporal pulse width.

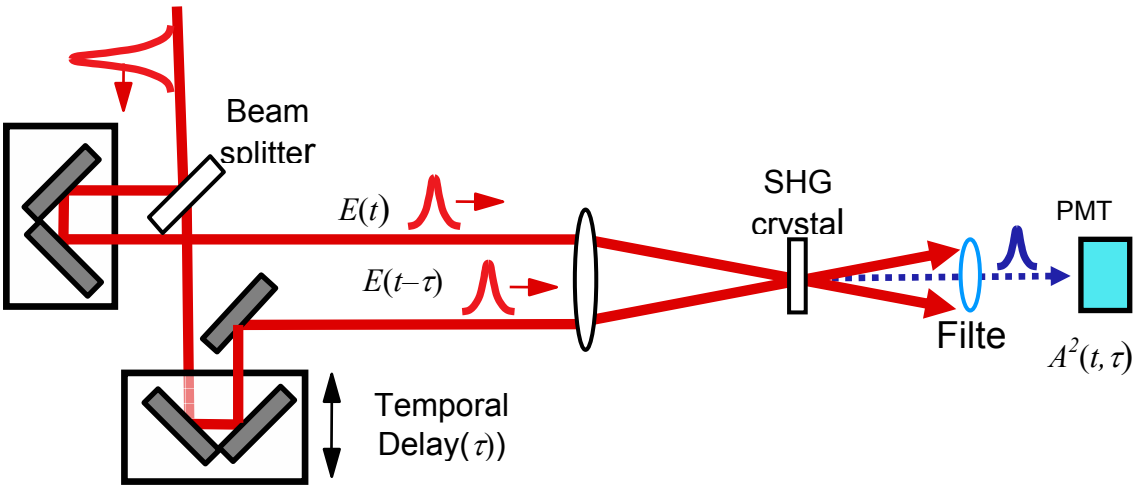

Figure 12. Cross Intensity Autocorrelation Setup.

There are several problems regarding the autocorrelation measurements. The most obvious one is time ambiguity, since $A^2(\tau) = A^2(-\tau)$. The direction of asymmetry of the pulse profile cannot be resolved. Also, de-convolution requires knowing the envelope of the pulse, which in this case is guessed to be a Gaussian or hyperbolic secant squared. Usually, it is good guess especially when the spectrum information is available. However, any structure that deviates from a simple Gaussian or sech^2 can easily lead to large errors. One method by which to estimate the uncertainty is to compare a time bandwidth product, $\Delta t \Delta f$, of a transform-limited value based on a guessed shape of the envelope of the pulse, where Δf is spectral bandwidth in frequency. A transform-limited pulse width assumes a constant phase term in order to produce a temporal width for a given spectral width for a known pulse envelope. Therefore, a transform-limited time bandwidth product estimates how close the measured pulse is close to ideal assumed pulse envelope.

$$\Delta t_{ideal} \Delta f_{ideal} \leq \Delta t_{measured} \Delta f_{measured} \tag{14}$$

A spectrometer or monochromator measures $\Delta\lambda$; consequently, Δf can be calculated using the following relation:

$$\Delta f = \frac{c}{\lambda^2} \Delta\lambda \tag{15}$$

The presence of any chirp or increasing or decreasing phase will broaden the spectrum that leads to $\Delta t \Delta f$ to be greater than the transform limited value. Table 1 lists the time-bandwidth product values of typical pulse envelope.

Table 1 Time Bandwidth product and autocorrelation factor (FWHM)

Pulse Envelope Profile	Time Bandwidth Product	Autocorrelation factor
Sech^2	0.3148	0.6482
Gaussian	0.4413	0.7071
Lorentzian	0.2206	0.500
Square	0.8859	1.000

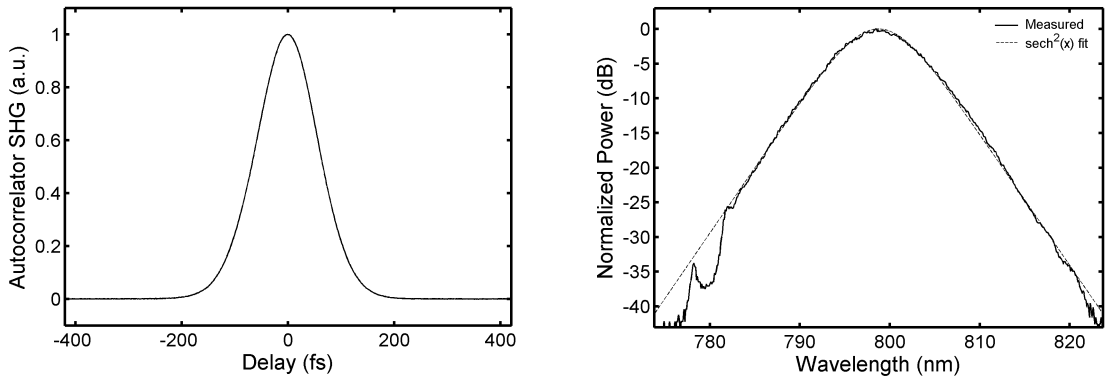

Figure 13. Measured Ti:Sapphire oscillator Intensity (a) Autocorrelation trace & (b) spectrum.

There are other types of autocorrelation such as an interferometric autocorrelation, third-order autocorrelation, fringe resolve autocorrelation, etc, that have some improvements over the original intensity autocorrelation, but only limited information can be extracted. Recently, a better solution has been introduced, called Frequency Resolved Optical Gating (FROG) [35]. FROG is an improved method for ultrafast measurements that overcomes limitations of phase information by retrieving a spectrogram of the gated pulse. There are many variations of FROG available. The PC THz source excitation is only necessary to generate carriers; therefore, it is not critical to obtain the phase information, or the direction of chirp.

3.2.2. SHG non-collinear Phase Matching Conditions

The intensity autocorrelation is made possible because of existence of SHG crystals. There are certain limitations and conditions that require attention in order to prevent errors in autocorrelation measurements. This section takes a closer look at these limitations.

A second harmonic generation is a nonlinear frequency doubling process, $\omega_{sig} = 2\omega$, where ω is an angular frequency. The simplest form of second harmonic generation (SHG) is a monochromatic plane wave, $\widetilde{E}(t) = Ee^{-i\omega t} + c.c.$(complex conjugate), passing through a nonlinear medium in which $\chi^{(2)}$, the second-order susceptibility, is nonzero, where the induced polarization is expressed as.

$$\widetilde{P}(t) = \chi^{(1)}\widetilde{E} + \chi^{(2)}\widetilde{E} + \chi^{(3)}\widetilde{E} + \cdots \tag{3.16}$$

For a wavevector of second harmonic, $k^{2\omega}$, and a fundamental beam, k^{ω},

$$k^{\omega} = \frac{n(\omega)}{c}\omega = \frac{2\pi n(\lambda)}{\lambda} \tag{3.17}$$

$$k^{2\omega} = \frac{n(2\omega)}{c}2\omega = \frac{2\pi n(\lambda/2)}{\lambda/2} \tag{3.18}$$

where the phase mismatch is

$$\Delta k = k^{\omega} - 2k^{2\omega} = \frac{4\pi}{\lambda}(n(\lambda/2) - n(\lambda)) \tag{3.19}$$

The maximum efficiency of SHG is achieved when $\Delta k = 0$.

For most materials, dispersion does not permit $n(\lambda/2) = n(\lambda)$. Birefringent materials, however, have polarization dependent refractive indices; along with ordinary and

extraordinary refractive indices [36]. The difference in the indices of these materials does allow $n(\lambda/2) = n(\lambda)$ to be satisfied.

Ultrafast pulses by nature have a large spectrum that expands more than tens of nm. Therefore, phase-matching bandwidth also needs to be considered for pulse measurements. SHG intensity has the following relation to SHG crystal thickness L[36]

$$I_{SHG}(L) \propto (\frac{L}{\lambda})^2 \operatorname{sinc}^2(\Delta k \frac{L}{2}) \tag{3.20}$$

Therefore, the SHG signal efficiency increases with L^2 while the phase-matching bandwidth scales as $1/L$, since the sinc^2 function decreases by factor of 2 when $\Delta k \frac{L}{2} = \pm 1.39$.

There are other considerations such as depletion of fundamental beam and group-velocity mismatch that prohibit the use of a thick crystal. Typically, a SHG crystal, KDP and BBO, of thickness less than 100 μm is suitable for the intensity autocorrelation

3.3. Spatial Filtering

Photo-excitation of TEF PC source requires precise alignments in order to inject optical carriers at the desired location. The quality of the beam profile, therefore, plays an important role in the efficient injection of optical carriers. A spatial filter uses a lens to focus the beam, which is two-dimensional Fourier transformed plane at focus. A pinhole placed on the center of focal plane selects only the central part of the Airy distribution or TEM_{00} mode. Any imperfection or other frequency component focuses outside of the pinhole and accordingly is filtered out spatially. The size of the pinhole

depends on the wavelength and the size of incoming beam. The filtered part of the beam is collimated or expanded by a lens. By altering the intensity profile at the focus, a transverse intensity profile of the incoming beam can be close to a perfect Gaussian beam. Figure 14 shows the intensity profile taken by a Sony XC-75 CCD camera before and after the spatial filter. The spatial filter clearly exhibits an improved beam profile with a more uniform intensity profile and more rounded pulse shape.

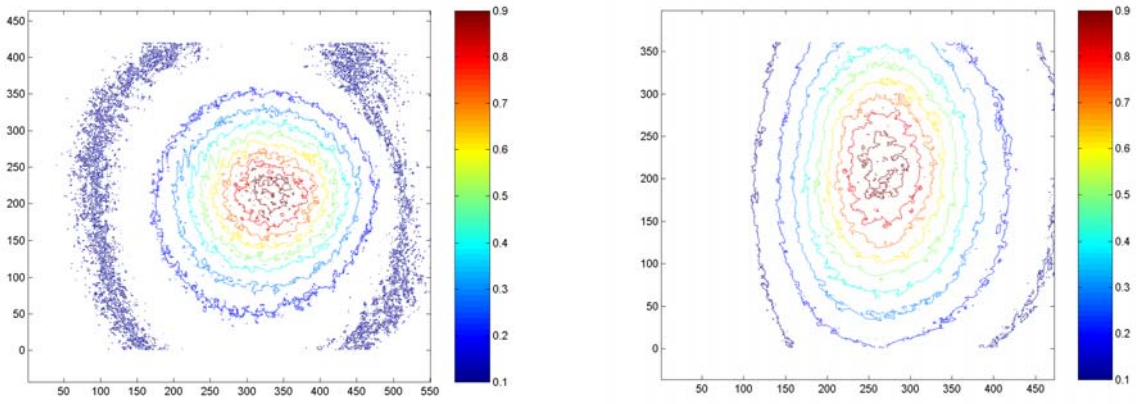

Figure 14. CCD image of the optical excitation beam; (a) after and (b) before the spatial filter setup.

Figure 15 shows the THz response before and after the spatial filter. It is not surprising to see improvements in total average power with the spatial filter, knowing the TEF region is confined to a small region. More importantly, the spatial filter provides a more diffraction-limited focus. As the optical power increases, the THz response is smoother when the spatial filter is used. The spot size estimation in this document is based on a diffraction-limited focus.

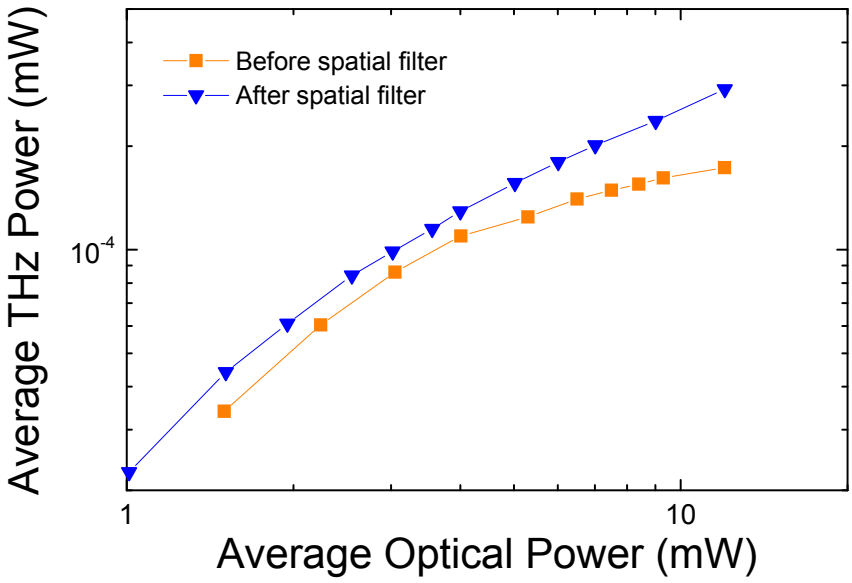

Figure 15. Experimentally observed THz power using a point excitation of THz sources before and after the spatial filter setup.

CHAPTER 4: Trap Enhanced Field effect

Chapter 3 reviews the optical pulse generation, pulse width measurements and the improved beam quality with the spatial filtering. Once optical carriers are injected into the semiconductor, the carrier dynamics inside the material determine the character of the subsequent THz emission. To increase the optical-to-THz efficiency, maintaining high-field regions is critical. One of the most efficient electrode configurations uses the TEF effect which develops fields in excess of 200 kV/cm with modest applied voltages of ~60V and provides a self limited mechanism that insures robust performance. However, even these sources [7] are limited to a few hundred nWs of THz power when using spot excitation of conventional ~82-MHz–repetition-rate femto-second sources corresponding to an efficiency of ~0.002% due to severe screening effects. Larger efficiencies and power have been reported using a variety of electrode configurations; however, these electrode geometries are not readily scalable to both larger powers and improved efficiencies [37,38]. This chapter closely examines the trap-enhanced field (TEF) effect in details beyond the original theory. Especially, the annealing dependence of the TEF effect is investigated in details. The chapter begins with the basic theory of metal-semiconductor contacts, which play an important role in generating TEF. Experimental data is then presented, including field scans, IV response, and THz power vs. optical power measurements to help demonstrate and explain some of the limitations as well as the TEF mechanism itself. Numerical simulations using the Sentaurus Device TCAD

simulator are also included to explain the TEF current transport. We will also establish the Quasi-Ohmic behavior of TEF.

4.1. Metal Semiconductor Contact Theory

This section reviews the metal-semiconductor contact and carrier transport theory. A more comprehensive study of metal-semiconductor contacts is given by Rhoderick [39]

4.1.1. Schottky Contact Theory

The equilibrium condition states that the Fermi levels of a semiconductor and a metal must coincide when they are in contact. The work function, Φ, is the difference in energy between the vacuum level and the Fermi level. Because the semiconductor and metal have different work functions, a barrier between the two materials is necessarily created to form an equilibrium condition. Figure 16 illustrates the Schottky barrier, defined by:

$$\Phi_{bi} = \Phi - \chi_s \tag{21}$$

where, Φ_{bi} is zero bias Schottky contact barrier height, Φ_m is work function of metal, and χ_s is zero bias Schottky contact barrier height

$$\chi_s = \Phi_s - (E_c - E_f) \tag{22}$$

where Φ_s is a work function of the semiconductor

Naturally, the schottky contact has the rectifying behavior.

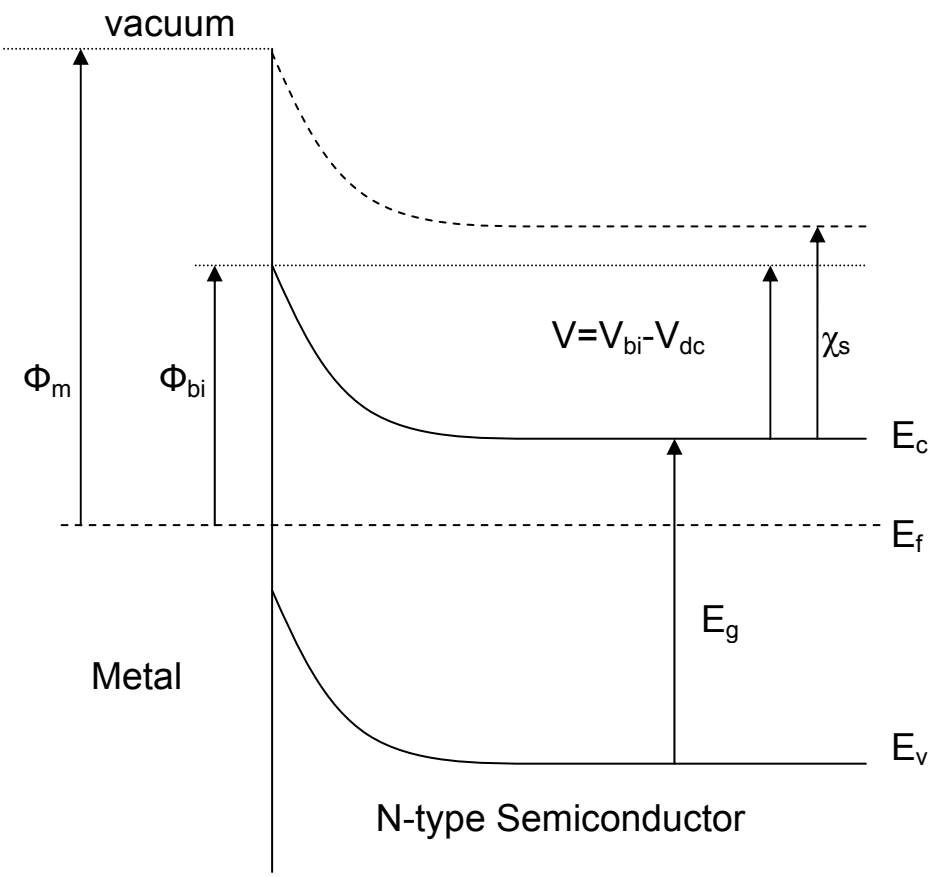

Figure 16. Unbiased structure of ideal metal/N-type semiconductor Schottky contact

The above theory assumes a simplistic ideal case of both the semiconductor and metal band diagrams. In practice, there is a thin oxide layer on the top of the semiconductor surface before it comes in contact with a metal layer. Furthermore the Fermi level of the metal is a often "pinned" at some position near the semiconductor bandgap due to surface states and other mechanisms.

4.1.2. Ohmic Contact

An ohmic contact refers to a contact with a linear IV characteristic. The ideal ohmic contact, also, has negligible contact resistance compared to the active region resistance of a semiconductor device. In practice, there is a typically acceptable contact

resistance that has a small voltage drop at a sufficient current density for a particular device operation. A typical method of creating an ohmic contact is to create a high doping region near the contact to allow sufficient tunneling through the thin depletion region. Another possible approach is to reduce the potential barrier, but this has been difficult to achieve for III-V materials such as GaAs due to the previously mentioned pinning effects. GaAs uses an alloyed metal contact, AuGeNi; many variations of temperature and annealing duration are used, such as annealing for ~30 min at 450 ºC. The specific composition and annealing process of AuGeNi alloy have been more art than science in that the optimal contact resistance has been achieved by trial-and-error.

4.1.3. Metal Semiconductor Contact Current Transport

The current transport in metal-semiconductor junction differs from that of p-n junctions in that majority carriers are dominant. There are three mechanisms to describe current transport in a metal-semiconductor junction: thermionic emission, thermionic field-emission, and field-emission. These transport mechanisms are based on Wentzel-Kramers-Brillouin (WKB) approximation, which is derived from a doping dependent tunneling probability. Thermionic emission (TE) is the carrier transport over a Schottky barrier, therefore primarily relating to the built-in barrier height. When the depletion width is too large due to a low doping concentration in the semiconductor, tunneling is unlikely to occur. For an intermediate level of doping the depletion region is reduced enough to allow some tunneling through the barrier, both TE and tunneling can contribute to their current density, called thermionic-field-emission (TFE). TFE includes an increased probability of tunneling through the barrier in addition to the TE process. Finally, when the contact region is heavily doped, the depletion layer is thin enough that

electrons can readily tunnel through the whole barrier. This process is known as field-emission (FE) [40, 41]. The specific contact resistance R_c is given by:

$$R_c = (\partial J / \partial V)_{V=0}^{-1} \tag{23}$$

TE
$$R_c = (k / qA)T \exp(q\phi_b / kT) \tag{24}$$

TFE
$$R_c = C_2 \exp(q\phi_b / E_{00}) \tag{25}$$

FE
$$R_c = C_3 \exp[\frac{\phi_b}{\sqrt{N_d} \coth(E_{00} / kT)}] \tag{26}$$

$$E_{00} = \frac{q\hbar}{2}\sqrt{\frac{N_d}{m^* \varepsilon}} \tag{3.27}$$

where q is the electronic charge, $\hbar$ is Plank's constant, m^* is the effective mass of electron, ε is the dielectric constant of the semiconductor, N_d is doping concentration, and T is temperature in Kelvin (K). There are two ways to lower the contact resistance down to ohmic region; one is to lower the barrier height, ϕ_b, or increase the N_d. For a wide band gap material such as GaAs, lowering the barrier height has been difficult to achieve. Therefore, FE leads to the ideal ohmic contact in which the carriers can readily tunnel through the barrier without creating a significant voltage drop across the depletion region. Figure 17 shows a band diagram and the current transport illustration.

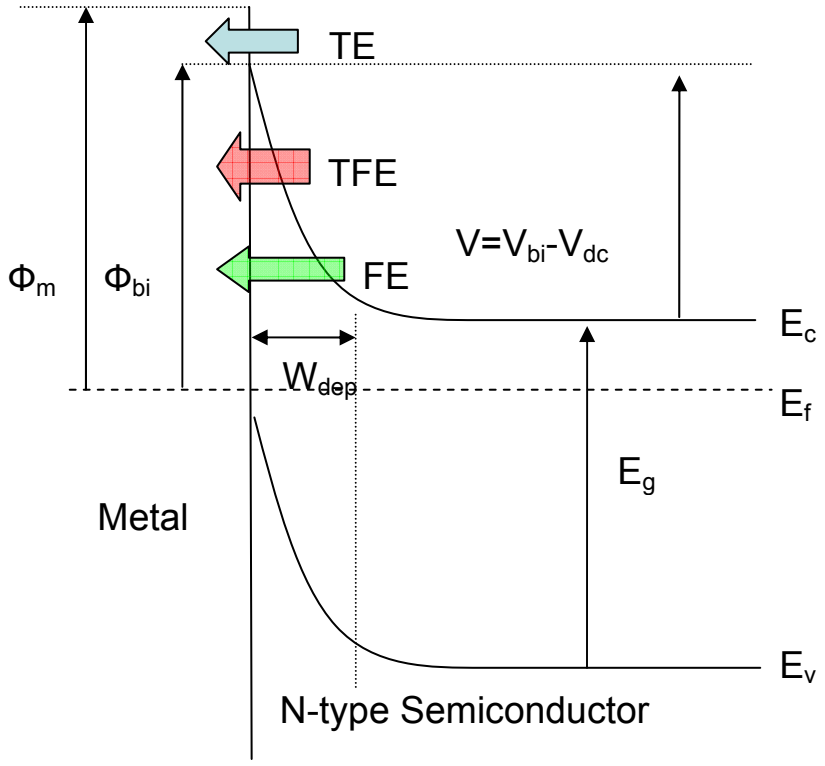

Figure 17. Unbiased structure of ideal metal/N-type semiconductor contact with three method of current transport

4.2. Trap Enhanced Field Effect

The trap enhanced field effect is a position dependent field enhancement at the anode of a DC biased metal-semi-insulator-metal structure on semi-insulating GaAs. The importance of the effect can be appreciated by considering that for an 80 μm separation, where TEF is pronounced, 90% of the bias voltage is found within the first 5 μm from the anode. With a modest 60 V bias, more than 40kV/cm can be generated. The field enhancement is demonstrated using THz illumination as a probe beam, where the anode produced more than 50 time greater THz power than the cathode. There are a number of physical mechanisms that contribute to the enhancement, including "(i) the quasi-static nonlinear field distribution (geometric effects), (ii) electron velocity saturation, (iii) space

charge of uncompensated residual acceptors resulting from the increasing occupancy of deep traps, and (iv) field-enhanced carrier injection."[12] Traps are initially occupied by holes at zero bias equilibrium. When a small current is introduced, the trap occupancy changes to mostly electrons due to a larger capture cross-section for electrons than holes. As a result, large number of uncompensated ionized acceptors create a space-charge region. Figure 18 illustrates stead state and electron occupied ELs traps due to current flow.

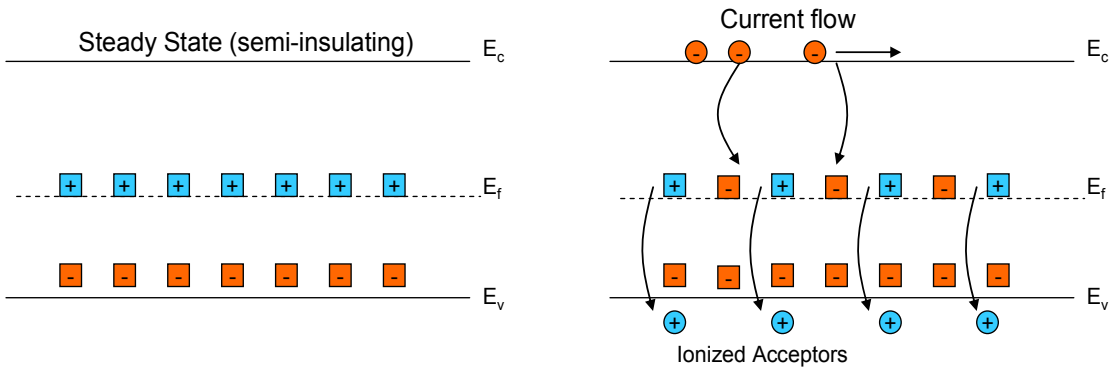

Figure 18. Band diagram for TEF. Steady-state semi-insulating & electrons occupying EL2 traps leaving uncompensated ionized accepters behind.

4.2.1. Trap Enhanced Field Effect Anode and Cathode THz Power Difference

The THz power from a THz photoconductive source has a square-law dependence on the number of carriers injected and accelerated carriers as described in the Larmor result. When the magnitude of the optical carrier injection is fixed, the total average THz power measurement can directly compare to the relative strength of the existing field strength. Figure 19 compares the directly measured THz power from excitation of both the anode and the cathode. The optical excitation is optimized at the anode to produce

the maximum THz power. The cathode excitation data is obtained by changing the polarity of the DC power supply in order to eliminate the alignment dependence. All the other experimental parameters remain the same. It is obvious from the data that there are at least three orders of magnitude difference in THz power measured. The difference in the mobility of the carriers or the geometric effect alone is not sufficient to explain the enhancement.

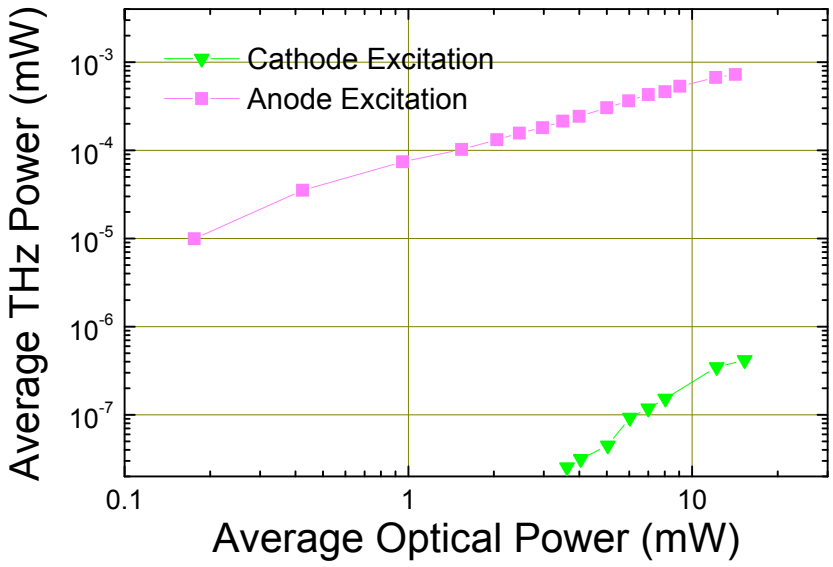

Figure 19. Experimentally observed THz power from both anode and cathode excitation. The DC bias polarity is switched without changing alignment.

4.2.2. Semi-insulating GaAs

Gallium Arsenide has been a subject of many studies as a possible alternative to silicon in VLSI, and it continues to hold its position in specialized applications including optoelectronics and microwave electronics. This results from the direct bandgap and the attractive electrical properties which are superior to that of silicon, such as a high carrier

mobility. Furthermore GaAs can be made semi-insulating by exploiting the relative ease of creating mid-gap states. The resistivity can typically be of the order of 10^7-10^8 Ω·cm.

The semi-insulating property is a direct result from the naturally occurring EL2 defect that compensates the unintentional doping of carbon during liquid-encapsulated Czocharlski growth. The carbon carrier density is of the order ~10^{15} cm^{-3}, which is less than the typical EL2 trap density of 10^{16} cm^{-3}. The EL2 defects acts as a deep trap compensating the carbon which is incorporated as a shallow acceptor

There are several reasons that semi-insulating GaAs is a well-suited material for an efficient THz photoconductive source. First, high resistivity is desirable to limit the amount of dark current that can heat up the source. Also, high carrier mobility allows higher acceleration that directly ties to THz radiation power. Moreover, the bandgap of GaAs is smaller than the photon energy of a typical femto-second Ti:Sapphire laser pulsed laser. The most important fact, however, is the existence of the EL2 deep traps that allow TEF to form. There are other materials that can be used to fabricate a THz PC source, such as InP, which has a higher carrier mobility than that of SI-GaAs; however, InP does not produce the high field enhancement found in semi-insulating GaAs. Semi-insulating GaAs trap parameters are listed in Table 2.

Table 2 Semi-insulating GaAs trap parameter at T=300 K

Traps	Values
Carbon trap	
Concentrations	$2x10^{15}$ cm^{-3}
Junction Depth	0.12 μm
Type	Shallow acceptor
Energy Level	Ev+0.026 eV
Degenerate factor ($g=g_1/g_0$)	0.25
EL2 trap	
Concentration	10^{16} cm^{-3} at 0.691 eV
Hole capture cross section (σ_p)	$6.5x10^{16}$ cm^2
Electron capture cross section (σ_n)	$2x10^{18}cm^2$
Type	Deep Donor
Energy Level	Ec-0.691 eV
Degenerate factor ($g=g_1/g_0$)	0.845

4.2.3. Poisson Charge Distribution in Semi-Insulating Material

P.M. Solomon and Weiser studied the trapping kinetics using Schokley-Read-Hall trap descriptions in conjunction with the current continuity equations [42].

The minority carrier lifetime is defined as

$$\tau_n^{-1} = \sigma_n N_t v_n \text{ and } \tau_p^{-1} = \sigma_p N_t v_p \tag{28}$$

where σ_n and σ_p are the electron and hole capture cross section.

a compensation ratio is defined as

$$r = \frac{N_a}{N_t} \tag{29}$$

Poisson equation from a small signal analysis as follows:

$$\frac{\rho}{q} = \alpha_p (p - p_0) - \alpha_n (n - n_0) \tag{30}$$

Assuming that the substrate is neutral and in equilibrium when $p=p_0$ and $n=n_0$.

$$\alpha_n = \frac{N_t \tau_p r^2 (1-r)}{n_0 \tau_p r + p_0 \tau_n (1-r)} \tag{31}$$

$$\alpha_p = \frac{N_t \tau_n r \ (1-r)^2}{n_0 \tau_p r + p_0 \tau_n (1-r)} \tag{32}$$

where N_t is trap density, and N_a is an acceptor density.

The amplification factor α_n and α_p is quiet substantial. For semi-insulating GaAs parameters, $\alpha_n=5\text{x}10^7$ and $\alpha_p=3\text{x}10^6$. Small increases in current (electron) density demands substantially large changes in holes. Therefore, the large enhanced field of the TEF is not unreasonable based on the above estimation.

4.3. Current Transport in TEF

High performance TEF THz PC sources have exhibited IV behavior shown in Figure 20. Four regions of current transport are identified. The first linear regime is where the current is restricted by the high resistivity of semi-insulating GaAs. The second regime is a space-charge limited current regime with a V^2 response. The third regime is a Gunn oscillation regime associated with a negative differential resistivity. One of the most distinct features of the I-V behavior is a current surge after the oscillation regime. The fourth and final part shows a sudden current surge into a double injection regime due to V^3 IV characteristics. This fourth regime is of the most interest because THz radiation operates and TEF is most pronounced in this regime.

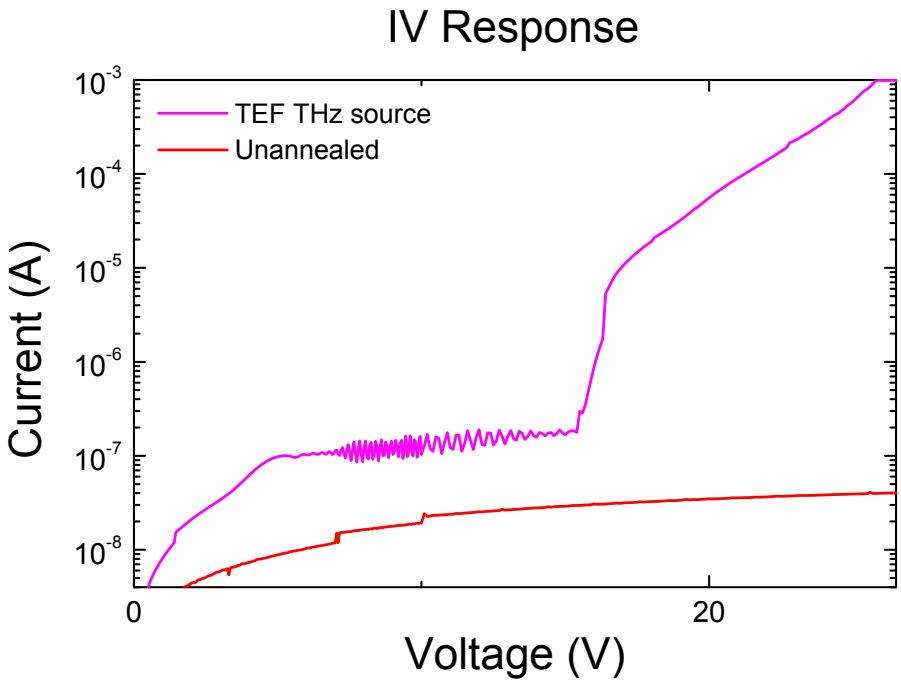

Figure 20. IV measurements for THz source with an optimum annealing temperature and insufficient annealing.

4.3.1. Bias Dependence: Enhancement and Limitation of the Field

The total radiated THz power comes from the acceleration of the carriers, and the acceleration of injected carriers is due to an existing DC bias field. Therefore, the THz energy is coming from the DC bias. TEF is a highly nonlinear effect, so the DC bias does not necessarily have a linear relationship. Therefore, an optical-to-THz efficiency number without a DC bias is not really a correct comparison. It is also a reason to understand the field strength distribution of a THz source based on varying DC bias voltage.

To directly compare the field-enhancement dependence of DC bias voltages, a point excitation of a focused 5 μm circular excitation and a calibrated helium cooled bolometer

directly measured the THz response vs. the excitation point. An actuator, a Newport CMA-25CCCL, accurately moved the position of an excitation spot perpendicular to the electrodes with 1 μm increments, scanning from the anode to the cathode. THz response of each position is recorded using a Labview-controlled lock-in amplifier. The silicon collimating lens behind the source is removed to avoid any diffraction and frequency dependent collection efficiency. All other experimental conditions remain the same except for the bias voltage. Figure 21 shows the THz response stepped across a THz source from the anode to the cathode. From the Larmor result with a fixed number of carrier injection, the recorded THz response is a direct response to the carrier acceleration, thus the relative field strength.

One of the obvious observations is the field enhancement around the anode. The two high peaks represent both edges of the metal electrodes; the separation of the two electrodes corresponds to the actual physical separation between the electrodes. Even at 20 V bias, the discrepancy of the field strength enhancement between the anode and the cathode is evident. As the bias voltage increase, the field continues to build around the anode reaching more than three orders of magnitude difference in THz power between the two electrodes.

With a bias voltage of up to 50 V, the field enhancement at the anode increases at a much faster rate than that of the cathode. The field strength, however, begins to saturate at 55 V bias. As the bias voltage continues to increase, the cathode starts to increase in field strength with only limited enhancement in the anode. The result has significance in the total THz emission. There is an efficient and optimum bias point for TEF sources.

Therefore, increasing the bias voltage beyond 60V does not effectively improve the field strength, or average THz power, with an 80 μm separation TEF PC source.

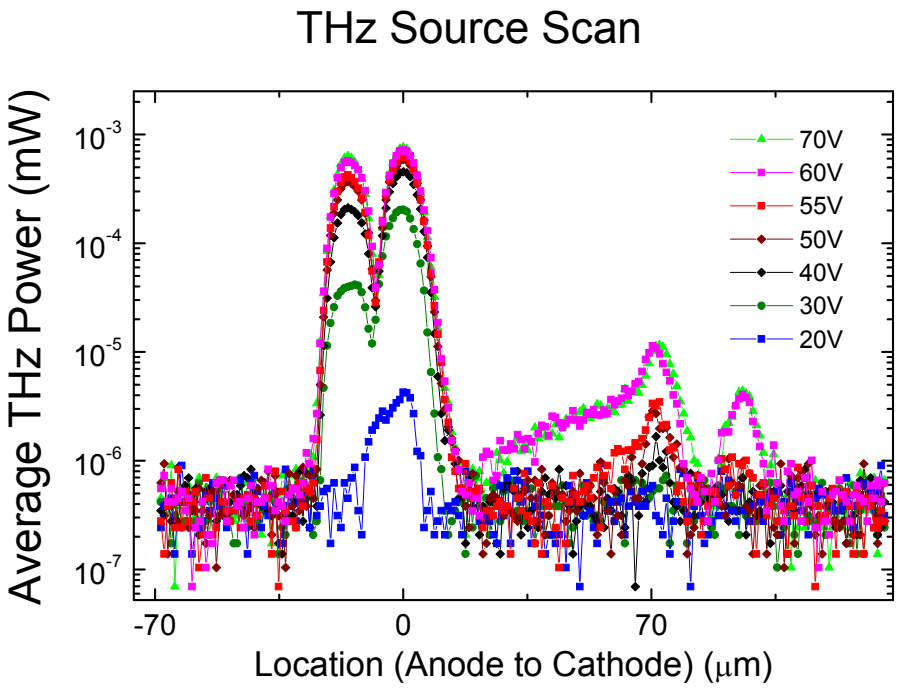

Figure 21 Bias dependent TEF field strength

4.4. THz Source Development

This section explains some of the experimental observations relating to parameters including the metallization, annealing, and resistivity.

4.4.1. Annealing Process

The annealing process has been a critical step to produce a good TEF contact and current-voltage relation (I-V) with the sharp transition regime. For earlier series of sources annealing was done using a rapid thermal annealer (RTP) located in MiRC cleanroom at the Georgia Institute of Technology. A 30 second ramp up, 30 second

anneal, and 30 second ramp down at temperature around 390 ºC was used. Unfortunately, RTP produced inconsistent results. A custom designed resistive heating annealer was used to replace the RTP. Nitrogen flow of 12 SCFH was used to minimize any impurity attached to the source surface during the annealing as well as cooling time. The annealing temperature quoted in this document indicates the peak temperature set. Ramp up temperature was set to move rapidly until five degrees below the desired temperature, then the ramp up speed was reduced to ~2 °C/min. The optimum annealing temperature is experimentally found to match the I-V behavior of a known, previously characterized THz source. There was no noticeable difference in THz source performance between the two annealing methods, however the custom-resistive heater produced more consistent performance.

4.4.2. Contact Metallization

Two metallization recipes have been tested to compare THz performance. Both recipes are often used to create ohmic contacts for n-type GaAs. Two recipes are shown on Table 1 from the substrate up, including layer thicknesses. Recipe B uses alloyed AuGe with an 88-12% ratio.

Table 3. Metallization recipes for recipes.

Recipe A	Recipe B
Substrate 50 Å Ni 100 Å Ge 800 Å Au 100 Å Ge 300 Å Ni 1000 Å Au	Substrate 800 Å AuGe (88-12) 100 Å Ni 1000 Å Au

THz sources were fabricated with both metallization recipes on the same wafer for a comparison study. The optimum annealing temperatures found and the corresponding procedure is described in the previous section. High performance THz PC sources exhibited the I-V behavior shown in Figure 22. This I-V behavior has proven to be a good indicator of THz performance. The I-V response of Recipe B exhibited a sharper transition into high current regime. THz sources with both metallization schemes were tested and their performance is recorded in Figure 23. Clearly, the metallization used in Recipe B generated higher THz power than Recipe A, as suggested in the I-V response.

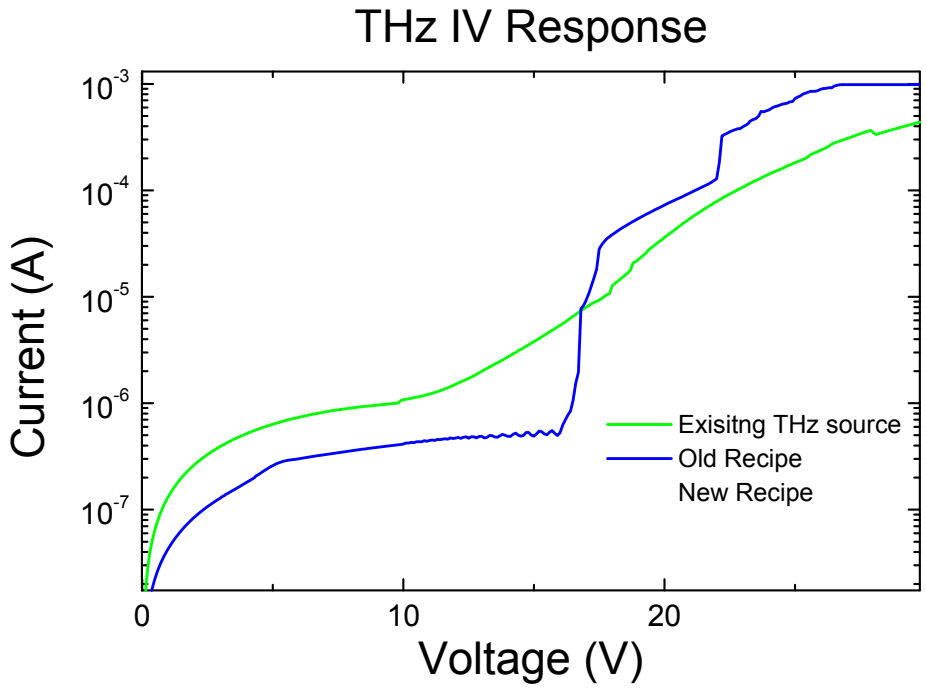

Figure 22. IV response comparison between recipe A and B with the existing THz source.

We have also noticed that Recipe A required a higher annealing temperature. Recipe A required less then 10 °C accuracy for the annealing temperature, while Recipe

B had a range of more than 20 °C. Also, the metallization used in Recipe B has fewer steps than Recipe A. The temperature difference could be due to more accessible Ge in the metallization stack from Recipe B, which allows easier diffusion into GaAs than in the case of Recipe A, which contains an additional Ni layer on top of the substrate.

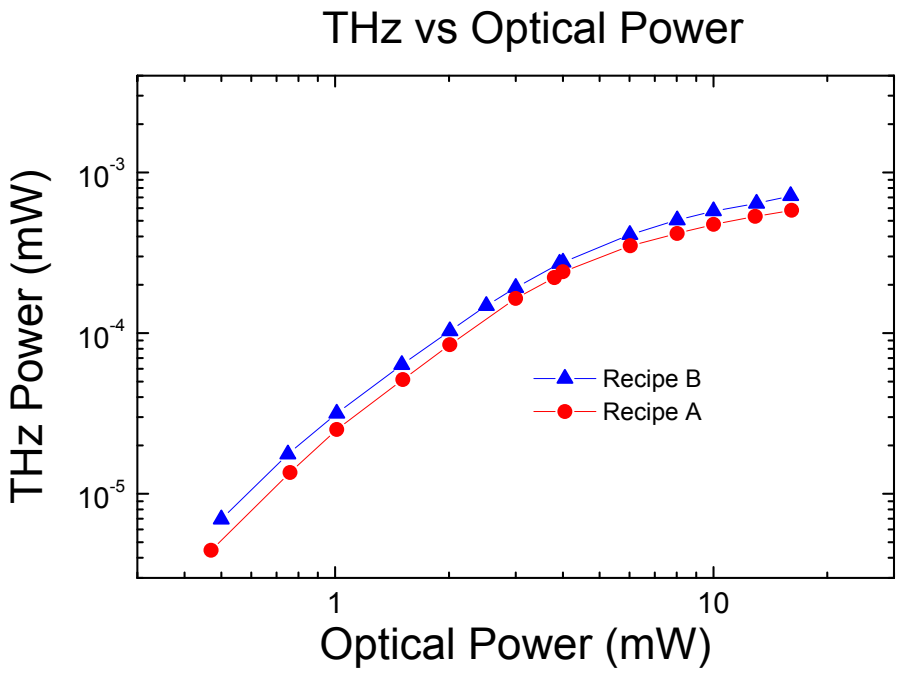

Figure 23. Experimentally observed THz power using a point excitation of two different metallization.

4.4.3. Resistivity Relation

Three different resistivity values of SI-GaAs are chosen for a direct comparison of THz performance. All three types were purchased from AXT. Each wafer was cleaved in quarters in order to allow all samples to be processed at the same time. All three THz sources were annealed at the same temperature and conditions. Figure 24 shows that THz sources fabricated on KF578 consistently performed better over other two wafers. The result, however, fails to relate resistivity directly to THz performance, because the

lower-resistivity KD510 source performed better than the higher-resistivity KJ832 source, while the highest-resistivity KF578 source produced the highest THz power among all of the samples. Differences in resistivity might be insufficient to explain the differences in THz performance.

Table 4. Material property for tested Semi-insulating GaAs.

	Semi-Insulating undoped GaAs; Vendor : AXT		
Ingot Number	KD510	KJ832	KF578
Resistivity (ρ)	2.9-4.1 x 10^7 Ω cm	8.6-9.5 x 10^7 Ω cm	1.2-1.7 x 10^8 Ω cm
Thickness	600 μ m	600 μ m	600 μ m
Diameter	4”	4”	4”
Mobility	6800 cm^2/Vs	6200 cm^2/Vs	5290 cm^2/Vs

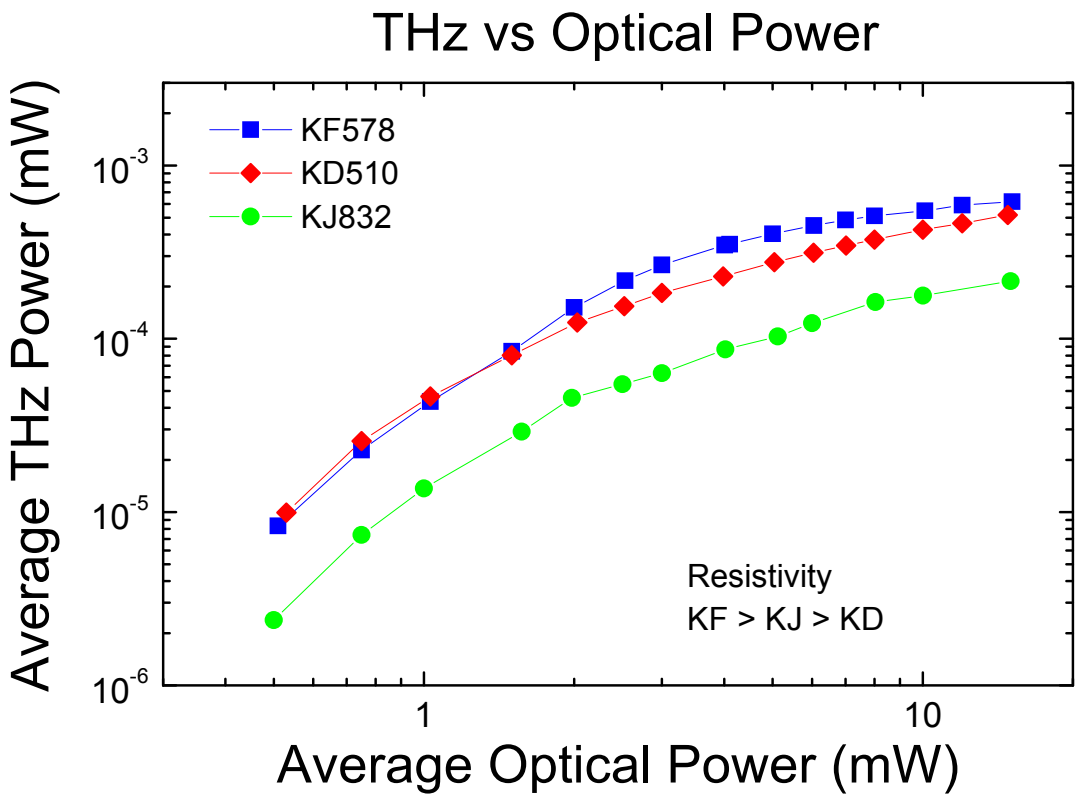

Figure 24. Experimentally observed THz power using a point excitation of THz sources with different resistivity values.

4.5. Quasi-Ohmic Contact of TEF

Most THz PC sources have used an ohmic contact metallization that is typically followed by annealing process. The emphasis in creating these contacts has been to reduce the specific contact resistance so that the bias voltage has maximum contribution to semiconductor region, turning into ohmic contact. The TEF THz source, however, behaves differently than other THz PC sources in that the optimum annealing temperature exists where the field enhancement is maximized. In fact, the optimum annealing temperature is found experimentally to match the I-V behavior shown in Figure 20. The

TEF I-V current consistently exhibits a sudden current surge into the double-injection regime. An over-annealed or ohmic contact did not necessarily produce a better THz source. The annealing dependence of the THz source has never been directly quantified in order to describe THz performance.

4.5.1. Experimental Setup: Annealing dependence of TEF

In order to relate the THz annealing temperature, I-V response, and TEF field enhancement magnitude, the THz PC source consists of two coplanar metal electrodes on semi-insulating GaAs with 80-μm separation and is processed on a single wafer. Four sources are prepared; one undergoes no annealing, while three are annealed at different temperatures: 320 ºC, 340 ºC, and 370 ºC. The results from these sources are recorded in Figure 25. The 320 ºC annealing temperature produces the typical TEF source and current surge. As the annealing temperature increases, the I-V behavior begins to resemble an ohmic contact, while the unannealed IV remains saturated. The 370 ºC annealed TEF source I-V response begins to approach that of ohmic behavior. Also, the onset voltage into high current region decreases with increasing temperature.

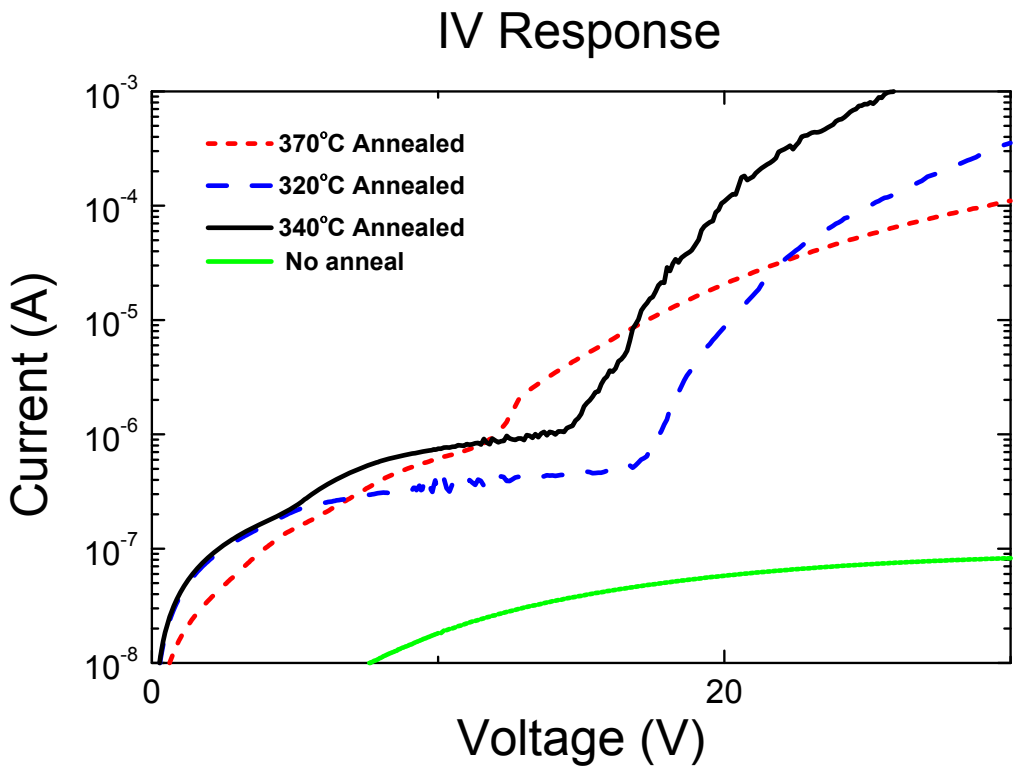

Figure 25. IV measurements of THz source with a different annealing temperature and unannealed source

To directly compare the TEF field enhancement dependence on the annealing temperature, a point excitation of a focused 5 μm circular excitation and a calibrated helium cooled bolometer directly measured THz response across both electrodes of each source with different annealing temperatures. An actuator, the Newport CMA-25CCCL, accurately moves the position of an excitation probe beam perpendicular to the electrodes with 1 μm increments, scanning from the anode to the cathode. The THz response of each position is recorded using a Labview-controlled lock-in amplifier. The silicon collimating lens behind the source is removed to avoid any diffraction and frequency dependent collection efficiency. Optical excitation power is a fixed at 5 mW for all sources with a 60V DC bias.

4.5.2. Experimental Results and Analysis

Figure 26 shows the THz response across a THz source from the anode to the cathode. An annealing temperature of 320 ºC clearly produces the highest THz power, corresponding to the highest field enhancement of TEF. As the temperature increases, the field enhancement starts to degrade, as is shown in the 340 ºC and 370 ºC cases. This result occurs despite the higher steady-state current found in the I-V responses of the 340 ºC and 370 ºC cases. Also, the unannealed source does not show any field enhancement at the anode. In fact, the cathode produced higher THz power than that of the anode. There are a several conclusions to be reached from these observations. An optimum annealing process is a necessary step in order to generate good TEF contacts. While annealing is necessary, over-annealing is not desirable.

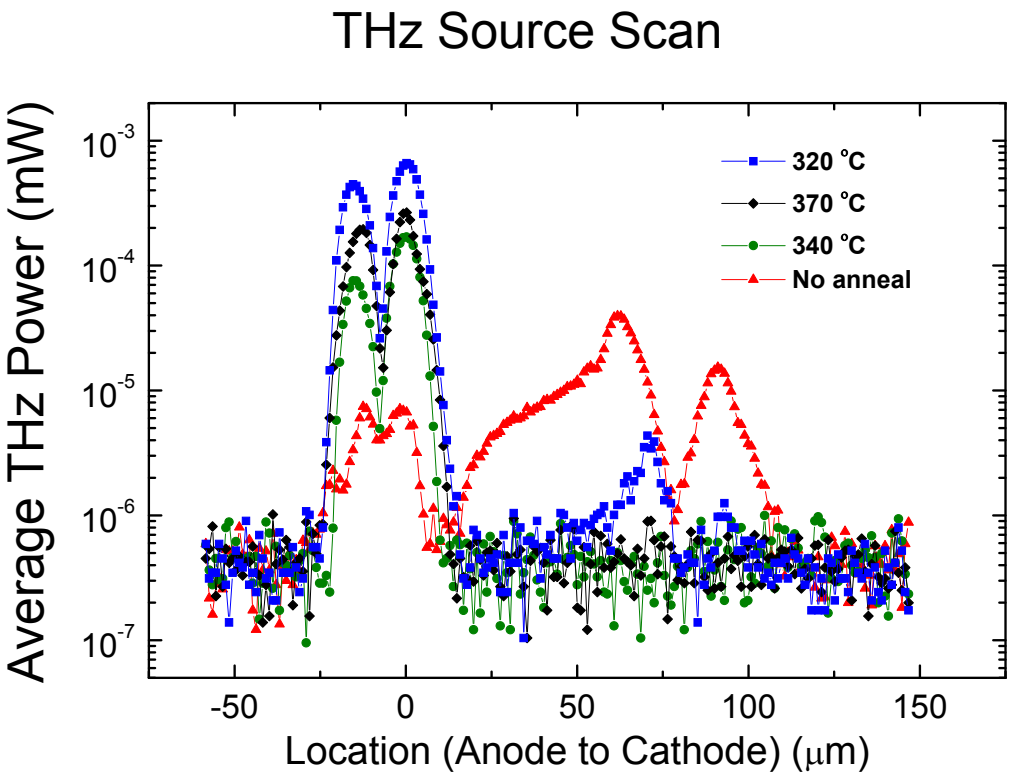

Figure 26 THz Annealing Temperature Dependence

The result is quite obvious that the TEF THz source contact is quasi-ohmic rather than ohmic or Schottky. There have been a number of studies carried out in order to analyze AuGeNi ohmic contacts. One of the effects of the annealing process is the diffusion of Ge, acting as a donor, into Ga vacancies. In the ohmic contact, the density of Ge is measured up to the order of 10^{19} cm^{-3} [43]. The presence of Ni improves the adherence to GaAs and assists the diffusion of Ge and Ni into GaAs. Also, Rutherford backscattering spectra show that the in-diffusion of Au and out-diffusion of Au in Ohmic AuGeNi contact [44].

The annealing temperature of 320 ºC is below the eutectic temperature of AuGe. Also, it is evident from the experimental results above that the TEF contact is not ohmic.

Nonetheless, the annealing results suggest that there could be some low-level diffusion that creates a doping region underneath the metal electrodes for the TEF sources.

4.5.3. Experimental Setup: Bias dependence of unannealed THz source

It is apparent from Figure 26 that the annealing is an important factor in determining the field distribution for THz PC sources. A direct comparison to unannealed device field distribution can provide further insight into understanding TEF mechanism. To directly compare the field enhanced dependence on DC bias voltages, a point excitation of a focused 5 μm circular excitation and a calibrated helium cooled bolometer directly measure the THz response vs. the excitation point. An actuator, the Newport CMA-25CCCL, accurately moves the position of an excitation probe perpendicular to the electrodes with 1 μm increments, scanning from the anode to the cathode. The THz response of each position is recorded using a Labview-controlled lock-in amplifier. A silicon collimating lens behind the source is removed to avoid any diffraction and frequency-dependent collection efficiency. This setup is identical to the previous bias dependence setup of TEF THz source in section 4.3.1 except that an unannealed TEF source is used instead of TEF source.

Figure 27 shows the THz response across a THz source from the anode to the cathode. It is apparent from a low bias that the field is enhanced at the cathode. As the bias voltage continues to increase, the cathode field begins to expand toward the semi-insulating region, unlike the TEF source in which the field enhancement exists close to the anode. The slope of the I-V behavior in semi-insulating region appears to be linear ohmic behavior. Another interesting observation is that anode side enhancement

surpasses the cathode region enhancement once the bias voltage reaches 70 V. In fact, when the bias voltage increases to 80 V, the anode region field strength improves.

There are number of conclusions can be drawn from the result. The TEF is not solely dependent on the accumulation of the charges. The TEF bias scan demonstrate that the 20 V bias is sufficient to cause the anode region enhancement. Even if we allow additional 40 V voltage drop across the contact, the field enhancement of the TEF is not present. The anode field enhancement finally shows up at 70V bias and above. This is due to the possible onset of the TEF effect in the unannealed source. At such a high bias voltage, the barrier-lowing effect becomes significant enough to allow the source to reach the threshold current flow to onset the TEF effect.

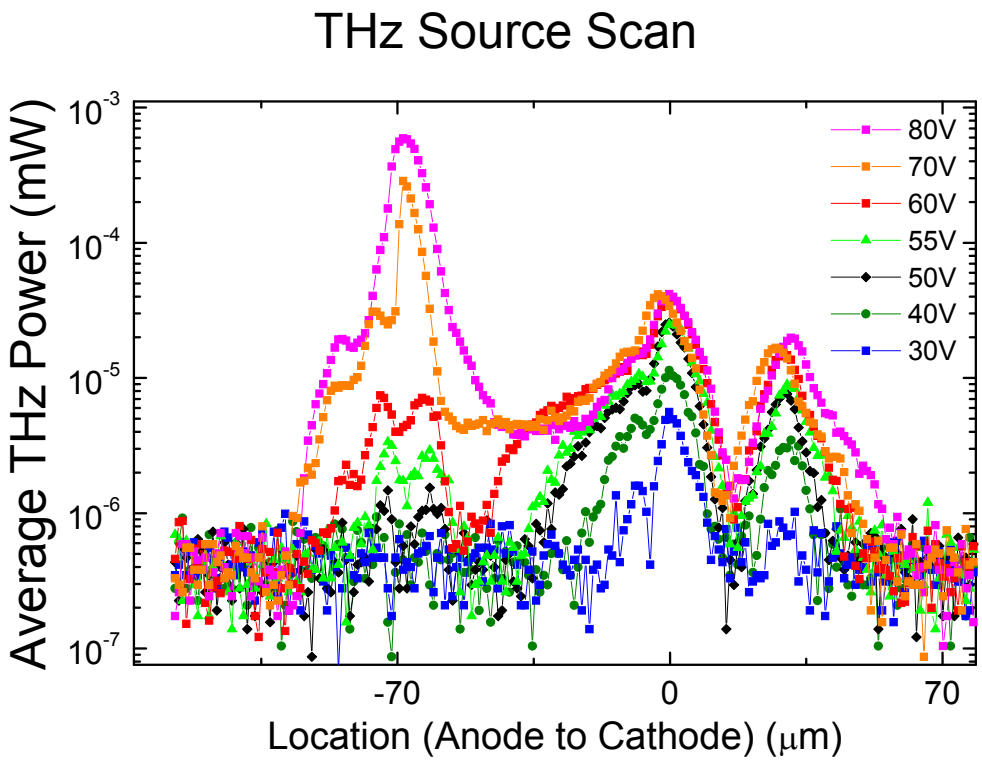

Figure 27. Bias dependence of THz source scan of unannealed

4.6. Sentaurus Device Simulator

In order to evaluate the underlining physics of the trap-enhanced field effect, the Sentaurus Device TCAD simulator is used. Sentaurus Device is a widely used and commercially available multi-dimensional numerical device simulator [45]. It is primarily designed for simulating the thermal, electrical, and optical characteristics of silicon devices, but it is also capable of simulating compound semiconductor materials such as GaAs. Terminal currents, voltages, and charges are computed based on a set of physical device equations based on the carrier distribution and conduction mechanism. Sentaurus can adopt various 1D, 2D & 3D mesh sizes, generated by the Sentaurus Device Editor software. Sentaurus Device self-consistently solves Poisson's equation and two current continuity equations in order to calculate the carrier densities, potential, field strength, and carrier distribution. In addition, one of the major advantages is an ability to selectively include specific numerical model functions such as mobility, tunneling effects, bandgap narrowing, etc. The structure of TEF THz source is symmetric; therefore, a 3D model is not necessary for our purposes.

4.6.1.1. Simulation Parameters

One of the most important characteristics of TEF is the current surge in the I-V response. There is evidence that there is diffusion of Ge into the GaAs that creates the high doping region underneath both contacts. Ohmic contacts contain a carrier density of as much as 10^{19} cm^{-3}. Considering that TEF sources contain quasi-ohmic contacts, the doping density can be assumed to be less than that of an ohmic contact. Ranges of peak doping concentration from 10^{17} cm^{-3} to 10^{19} cm^{-3} are simulated along with an undoped case. An 80-μm gap THz source has the most pronounced TEF effect, but this large of a

structure requires a long computation time. As a preliminary analysis, 10-µm gap structures are tested. Figure 28 shows the simulated structure along with the mesh used by the simulator. The doping region near the contact includes at least 10 mesh points. A command line example of an actual simulation is included in the Appendix.

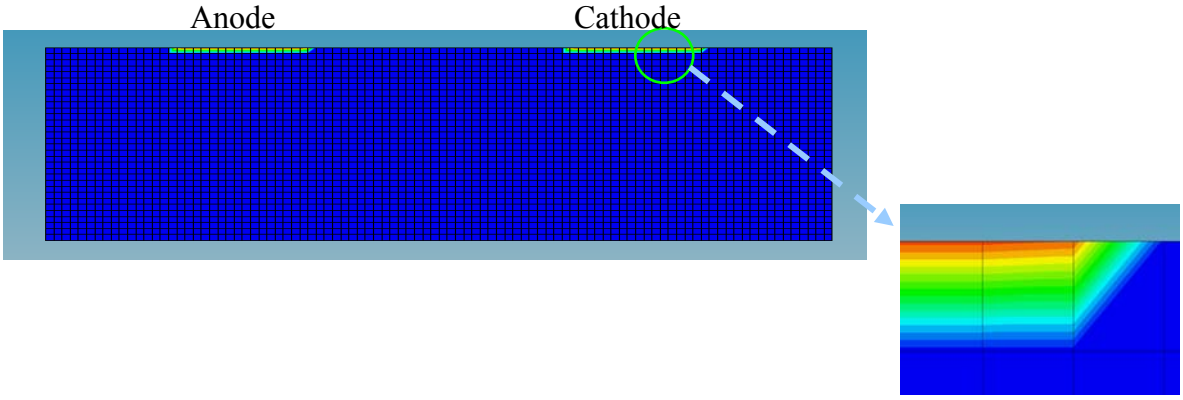

Figure 28. 10 µm structure mesh with doping and two electrodes are shown

Table 5 Simulation Parameters

Parameters	Values
Contacts	Schottky Barrier = 0.55 eV
Doping	Ge
Doping Concentrations	10^{17}, 5x10^{17}, 10^{18}, 5x10^{18},10^{19} cm^{-3}
Junction Depth	0.12 µm
Trap Density (EL2)	10^{16} cm^{-3} at 0.691 eV
Hole capture cross section	6.5x10^{16}
Electron capture cross section	2x10^{18}
Electrode width	10 µm
Sample Thickness	10 µm

4.6.1.2. Doping Concentration Variation Results

The main goal of this simulation is to emulate the I-V behavior of the TEF effect. Figure 29 shows an I-V response up to 150 V, along with the field strength at 150 V for a

10 µm structure without any doping region near the contacts. The anode field enhancement is present, but the current surge does not occur. The peak electric field is reaches almost 400 kV/cm, but the current seems to remain saturated. In many aspects, this result closely follows the experimental results of the unannealed THz source behavior. The field distribution also has a similar structure to the experimental results.

However, some problems do arise when comparing the simulation results with the actual experimental data. In order for field enhancement to occur at the anode, the metal semi-conductor contact barrier height had to be kept at 0.55 eV or below. Figure 30 shows the same structure and parameters as Figure 29 with the exception that the barrier height increased to 0.6 eV. In this case, the peak field shifts to the cathode and the current is quite different from that of the 0.55 eV barrier height case. In practice, a typical barrier height of a GaAs metal contact is measured to be ~0.6 to 0.8 eV.

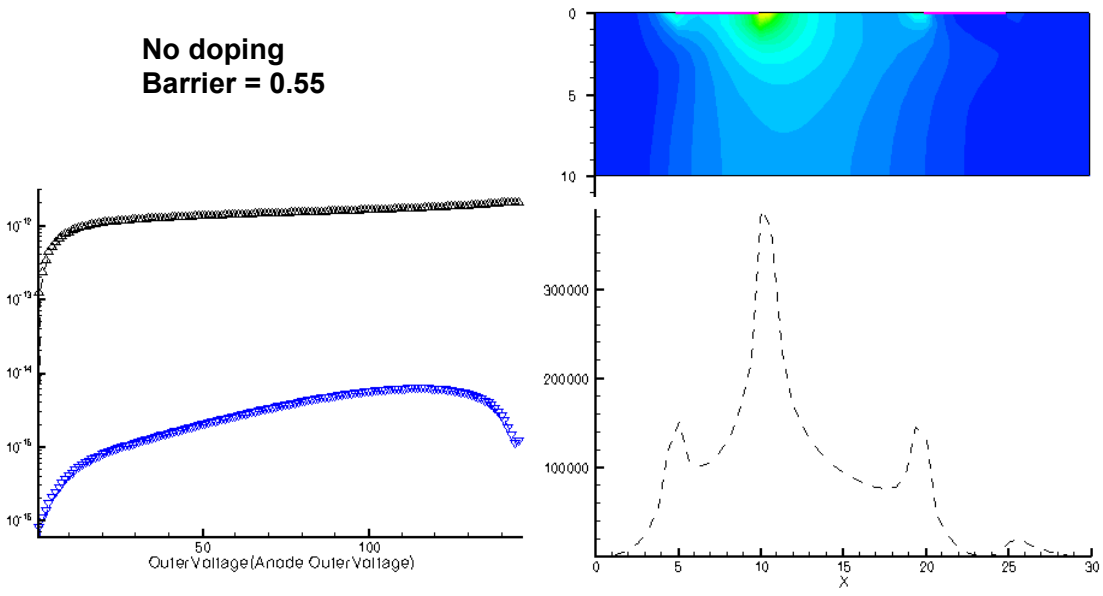

Figure 29 Simulation Results, IV response, E-field distribution without a shallow doping region with barrier height of 0.55 eV. Black line: Total current density; Blue – hole current density

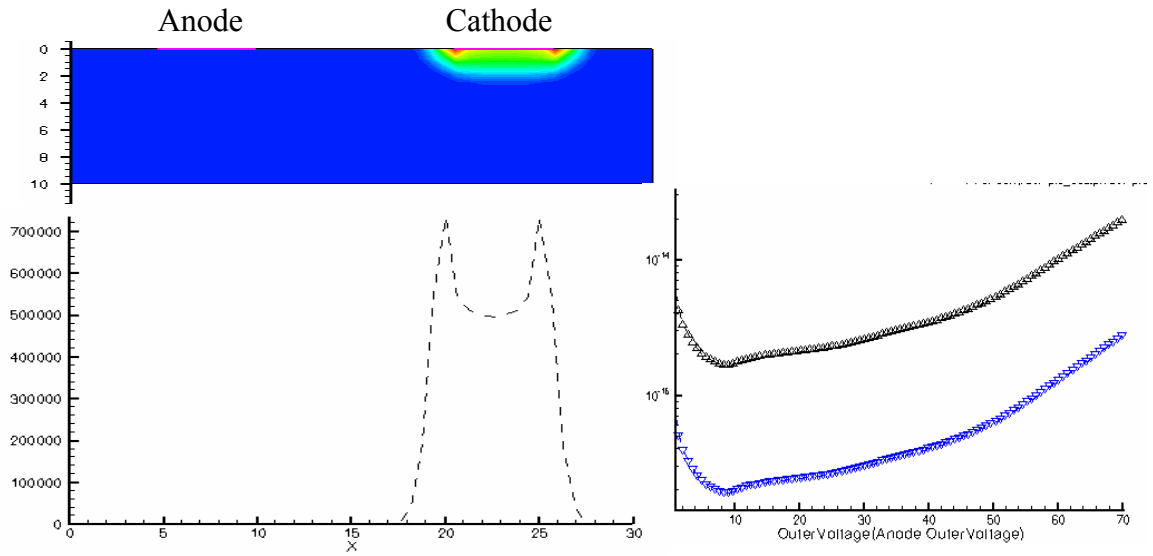

Figure 30. 10 µm structure mesh without diffused doping region, barrier high = 0.7 eV

One of the most important conclusions that the simulation has confirmed is that a doping region must be present for any current surge in the I-V response, validating the conjecture that the quasi-ohmic region must indeed include a shallow doping region beneath the contact. Without a shallow doping region, the I-V response followed the unannealed THz source I-V response. Figure 31 shows the simulated I-V response for different doping concentrations of the shallow high doping region. The I-V response is quite similar to the experimentally obtained I-V response. All four doping concentrations simulated result in a similar current behavior where the total current density is nearly identical. Electron current dominates the current flow for all cases. This result somewhat contradicts the double injection theory, which predicted that dominant hole injection current is the cause of the V^3 response. There is another problem comparing the simulation to the actual experimental results. The I-V response shown in Figure 31 indicates more than 100 V bias for only 10 µm electrode spacing is necessary to see a

current surge. The 80 μm THz source exhibites the current surge in the ~25 V range. It is reasonable to believe that a 10 μm source would require a far lower bias voltage to exhibit the current surge due to the smaller semi-insulating region.

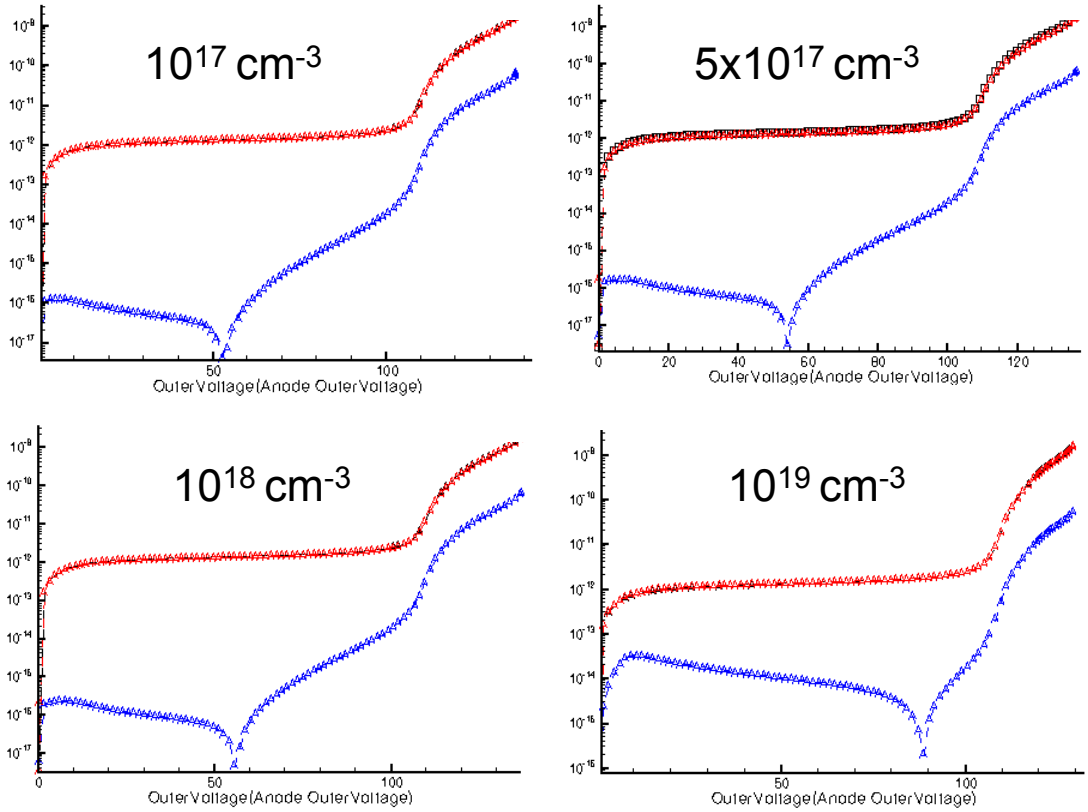

Figure 31 10 μm structure IV response. Red line indicates electron current and the blue line indicates hole current.

Figure 32 shows the magnitude of the electric field at a bias of 140 V, along with the field strength at the surface of the sample where the field strength is the highest. In typical operation, TEF occurs at biases immediately following the current surge. Therefore, a bias of ~140 V should generate similar field behavior as an 80 μm gap source operating at a bias of 60 V. All four different doping concentrations produced almost identical field strength. The field enhancement at the anode is present, but the

magnitude of the enhancement is much smaller compared to the cathode field strength. Also, the width of the enhanced field region is smaller than experimental data demonstrates.

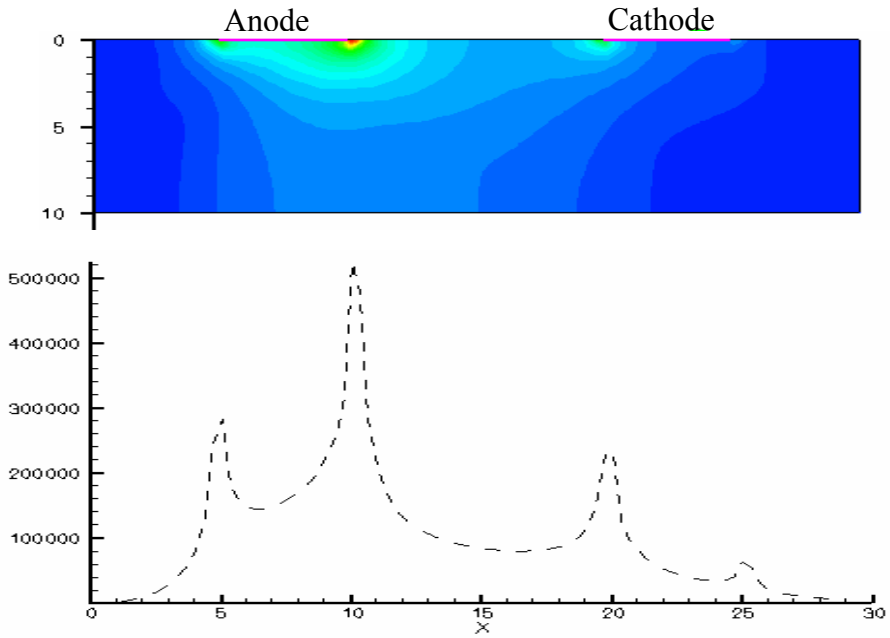

Figure 32. 10 µm structure mesh with doping and field strength at the surface is plotted

Figure 33 shows the DC bias dependence of the field distribution at the surface of a simulated source. Even at first glance, it is apparent that the field distribution does not resemble the experimental data of the 80 µm gap THz source scan. One important observation is that a high field resides in the insulating region. The result does, however, show the field saturation at the anode as the bias voltage increases. At 120 V, the field begins to increase at the cathode. It is not unreasonable for punch-through to occur in a source with a small 10 µm gap, because such a high bias voltage would cause a large voltage drop in the semi-insulating region; however, Figure 32 does not show the extended depletion region necessary to corroborate the presence of punch-through.

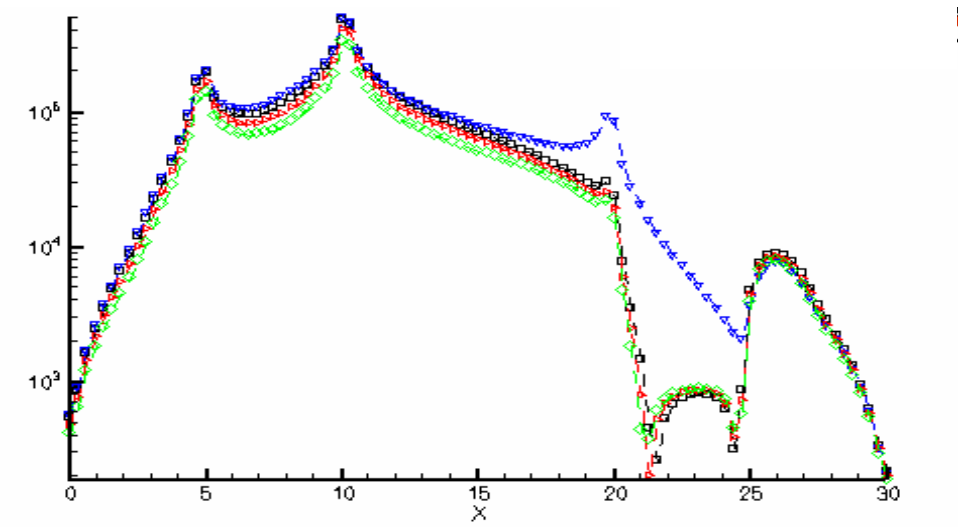

Figure 33. E-field variation (doping carrier density 5^{17} cm^{-3}) Blue 120 V, Black=105 V, Red=90V, Green=75V.

4.6.2. Model Limitations

Sentaurus Device has demonstrated some success in emulating the I-V behavior of a 10-μm TEF source structure, distinguishing annealing effects. Most importantly, the necessary inclusion of a thin high-doping region under the contact is consistent with the annealing dependent THz source field distribution. However, the simulated source requires a much larger voltage, in the order of 100s of volts, than is demonstrated by the experimental system. A larger gap of 40 μm and 80 μm gap has been tested, but the simulation was unable to be completed due to the high voltage required to reach a steady-steady solution. A larger voltage drop across the insulating region is not expected in the actual system, but the model is unable to configure such solutions requiring large bias voltage to reach sufficient current density. The major shortcoming of the software is its inability to calculate the resistivity variation. There are only two included models for resistivity, either a constant resistivity or a temperature dependent resistivity. On a

separate test, a simple n-type GaAs with a top and bottom contact fail to emulate Gunn oscillation. Sentaurus Device does include negative differential conductivity, yet was nevertheless unable to produce Gunn oscillation. Initially, the software was developed to handle silicon devices whose operating voltages are only several volts. The Sentaurus simulator does not appear to properly handle high level majority-carrier injection and is incapable of explaining the TEF effect in its entirety.

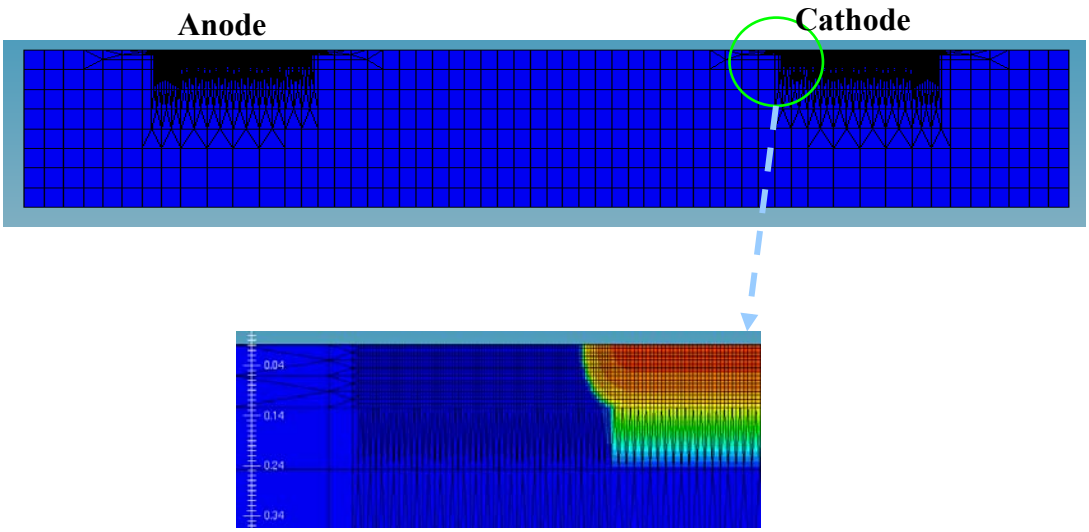

Figure 34. 40 µm structure mesh with doping and two electrodes are shown

4.7. Temperature dependent behavior of THz TEF source

There are several reasons why the TEF I-V response demonstrates the presence of avalanche breakdown. The first and most apparent reason is a high field region near the contact beyond normal geometric effects, reaching hundreds of kV/cm. The second reason is the quasi-ohmic contact behavior of the TEF source, in which the I-V response consistently produces a sudden current surge. Lastly, the Sentaurus model requires an avalanche model in order to exhibit the TEF I-V response.

Avalanche breakdown occurs when a carrier with sufficient kinetic energy collides with the lattice, generating electron-hole pairs that proceed to collide with the lattice, generating more electron-hole pairs that go on to do the same until the kinetic energy is no longer sufficient to create any more electron-hole pairs. Therefore, when the avalanche-breakdown threshold field strength is reached, there is a sudden jump in current far beyond the ohmic behavior of the material. A bulk GaAs material typically possesses a threshold field strength of more than 400 kV/cm.

One of characteristics of impact ionization is a temperature dependent enhancement of the avalanche multiplication factor. The temperature dependence of impact ionization strongly depends on the scattering of optical phonons. Increasing the temperature, therefore, requires a higher breakdown voltage to compensate for the increased phonon scattering rate [46]

4.7.1. Experimental Setup

The THz sources of a single pair with 80 μm gap with three different annealing conditions are compared. Each source is wire-bonded. A mechanical pump reduces the chamber pressure before the temperature reduced. Once the desired temperature is reached, data is taken after ~ 5 min to stabilize the temperature. The IV measurements are automated using Matlab controlled HP4155 semiconductor analyzer.

4.7.2. Results

Figure 35 shows the temperature dependent I-V response of an over-annealed TEF source. Measurements were carried out from 20K to 320 K, but below 150 K the I-V response ceased to vary with temperature. From 260 K to 320 K, current-surge

threshold voltages increase with the increasing temperature. This result is consistent with the avalanche behavior found in p^+in^+ avalanche diode [46]. At temperatures below 240 K, however, the I-V responses no longer exhibit the current surge observed at higher temperatures. This does not necessarily invalidate the avalanche process in TEF. As the temperature decreases the dark current is reduced below the necessary current density to produce the TEF and high field is no longer present at these temperatures. This observation is, therefore, in accordance with the TEF effect condition that sufficient current injection is required to fill the EL2 defects and create high field enhancement. In fact, the I-V response at low temperatures closely resembles the unannealed THz source I-V response. The unannealed source IV, Figure 35, shows no significant change in IV response other than the expected overall reduction in dark currents.

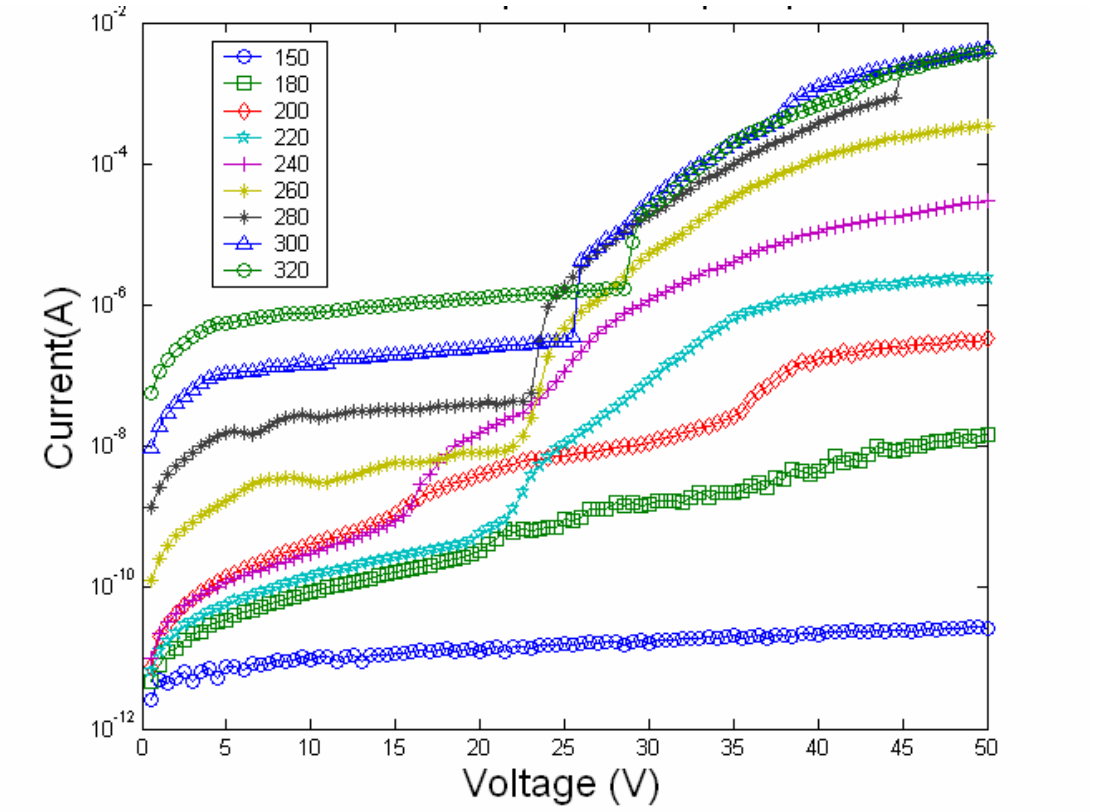

Figure 35 Temperature (K) dependence of over-annealed TEF THz source. Number in legend is in Kelvin.

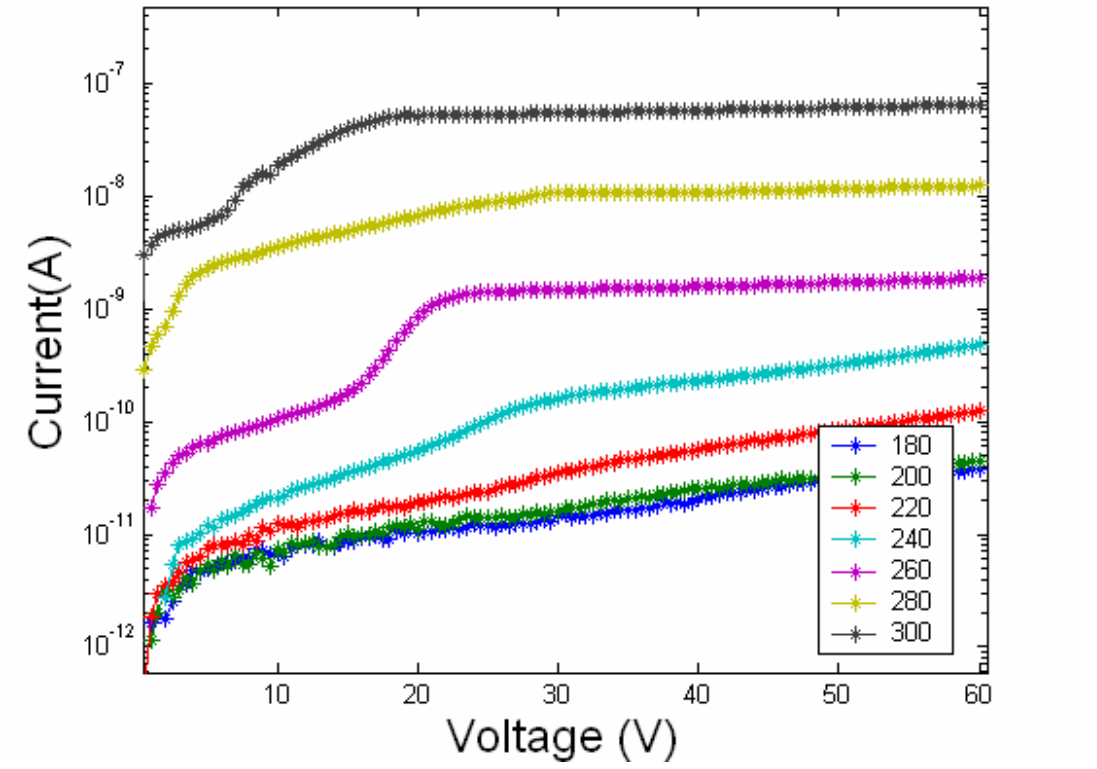

Figure 36 Temperature (K) dependence of un-annealed TEF THz source.

The 300 K IV response of Figure 37 demonstrates what we consider to be a high quality TEF source (shown in dotted line). Experimental data presented in previous sections already demonstrated that a higher electrical field resides compared to the over-annealed case of Figure 35. The I-V response from 300 to 260 K seems to agree with an expected avalanche driven process of lowering threshold effects. However, temperatures below 240 K give somewhat inconsistent results. More complex structure began to appear as the temperature decreases. Another observation is that the 140 K I-V response still produced a significantly larger current than that of the unannealed and the over-annealed cases.

The temperature dependent measurement results demonstrate some evidence that is consistent with impact ionization in the TEF THz source. A high quality TEF source

with its high field strength, the strongest avalanche behavior was expected. All three results are consistent with the impact ionization theory. However, it cannot be definitively concluded that the current surge mechanism is due to the impact ionization process.

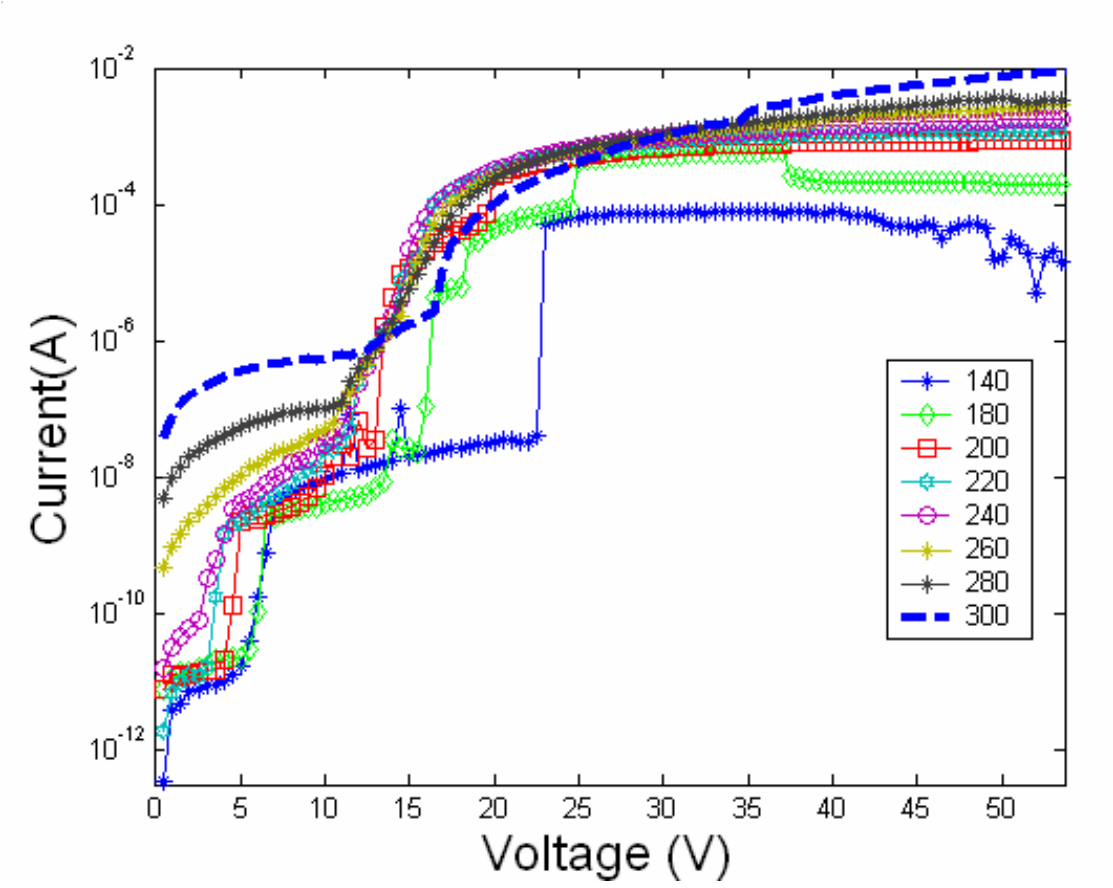

Figure 37 Temperature (K) dependence of good TEF THz source.

4.8. Summary: TEF Theory

There are several conclusions to be made from the experimental results. The first is the annealing dependence of TEF enhancement factor. Simulation results and other published records confirm that a doped region near the contact must be present, and that

the proper annealing is a necessary condition for a pronounced TEF effect. The second is the annealing temperature dependence. While a highly-doped region is necessary, the doping must not be so great as to create an ohmic contact. In fact, any deviation from the optimum annealing temperature reduced the total THz power.

There are two important conditions to explain this behavior: a high current density and the charge accumulation near the contact. One of the important characteristics of ohmic contact is their non-rectifying behavior. While this is not the case for most practical applications, ohmic contacts allow greater carrier injection through the contact before any significant charge accumulation occurs near the contacts, field emission process. TEF requires a large accumulation of electrons near the anode in order to fill the EL2 traps with electrons; this leads to uncompensated ionized acceptors and produces a large space charge region. The second condition to meet is to reach a threshold current density. The I-V response of the unannealed source not only lacks a sudden current surge region, but in addition, the current density remains low and saturated. If the unannealed source merely requires a larger voltage drop across the contact than TEF and ohmic contacts, we should see a shifted version of the bias dependence, but this is not the case. The high DC bias will cause the accumulation of electrons near the anode, but current density is not sufficient to increase the EL2 trap occupancy and change the charge distribution. The low current injection, therefore, generates resistive behavior in the semi-insulating region. The shifting of the peak-field region of the unannealed source can be explained in the same manner. At high biases, the thermionic emission current is enhanced due to the barrier lowering effect, and therefore the current density threshold is met at 70 V bias for the onset of TEF at high bias voltages. The quasi-ohmic contact

provides a balance between the two conditions for the most efficient field enhancement. These results are consistent with TEF theory. The current level, once greater than the threshold, does not seem to influence the anode enhancement. We have seen this in the 340 ºC annealed source, which produces greater current but less THz power when compared to the 320 ºC annealed source.

CHAPTER 5: Line Excitation

5.1. Spatially Extended Line Excitation

A TEF PC source is a high efficiency THz source that does not require a high voltage power supply or water-cooling. To utilize the TEF, most of the optical carriers need to be injected within the first 10 μm from the anode. A microscope objective focuses the light down to a small circular spot approximately 5 μm full-width-half-max (FWHM), called a point excitation. The focused spot, however, dramatically increases the optical carrier density. Consequently, THz power saturates even at modest optical excitation power, resulting in severe space-charge screening and a low efficiency. The Larmor result presents the square dependence of THz power on the acceleration and the optical injection, showing that there are two ways to improve power and efficiency: increase the total carrier injection or increase the existing field strength. The material breakdown voltage limits increases in the field strength. Increasing the optical carrier injection causes significant screening effects, reducing carrier acceleration. To mitigate the space-charge screening effects arising from a point excitation, we spatially shape the optical beam into a line excitation instead of the circular point excitation [23,47]. This spatially extended line reduces the optical carrier density without sacrificing total optical carrier injection while still utilizing the high field strength of the TEF.

5.1.1. Experimental Setup

The THz PC source consists of two coplanar metal electrodes on semi-insulating GaAs with 80-μm separation; the THz radiation is collimated by a hyper-hemisphere silicon lens attached to the back of the substrate [7]. The incident pulse is generated by a Ti:Sapphire oscillator operating at an 82-MHz repetition rate. A microscope objective generates a point excitation geometry of ~5 μm FWHM. The spatially extended line excitation geometries, ~6 μm x120 μm line and ~6 μm x 180 μm, are formed using two orthogonally oriented cylindrical lenses [48]. The THz power is directly measured using a separately calibrated liquid-helium-cooled bolometer power detector.

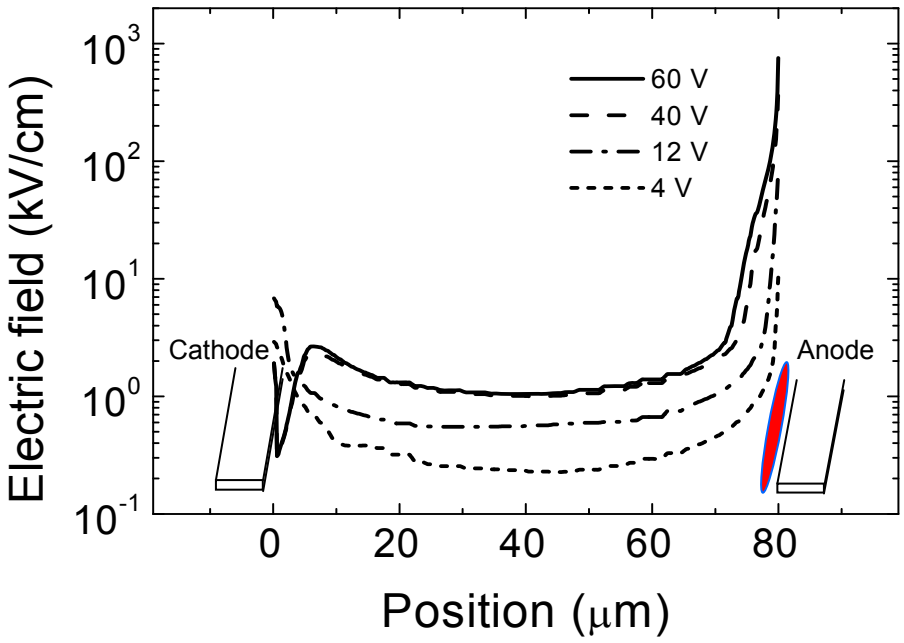

Figure 38. Optical excitation geometries of line excitation and electrodes overlaid on calculated field strength across the electrodes for 60 V bias.

5.1.2. Experimental Result

The average THz power observed from the three excitation geometries on the same source chip is shown in Figure 39. The point excitation response saturates near 1mW of optical power. In contrast, the line excitations retain a square-law dependence of the Larmor result, producing more than an order of magnitude higher THz power compared to the point excitation. At ~20 mW optical illumination, the line excitations reproducibly generate greater than 10 μW of THz power. The longer 180-μm line excitation produces a higher efficiency and power compared to the 120-μm line. This number represents an efficiency of ~0.1%, which is greater than previously reported photoconductive switches [21]. A THz large aperture source with a similar efficiency was reported but a water-cooled source and a high voltage source were required [11]. The larger power available from line source excitation is sufficient to use a room-temperature pyroelectric detector with excellent signal to noise instead of a helium-cooled bolometer.

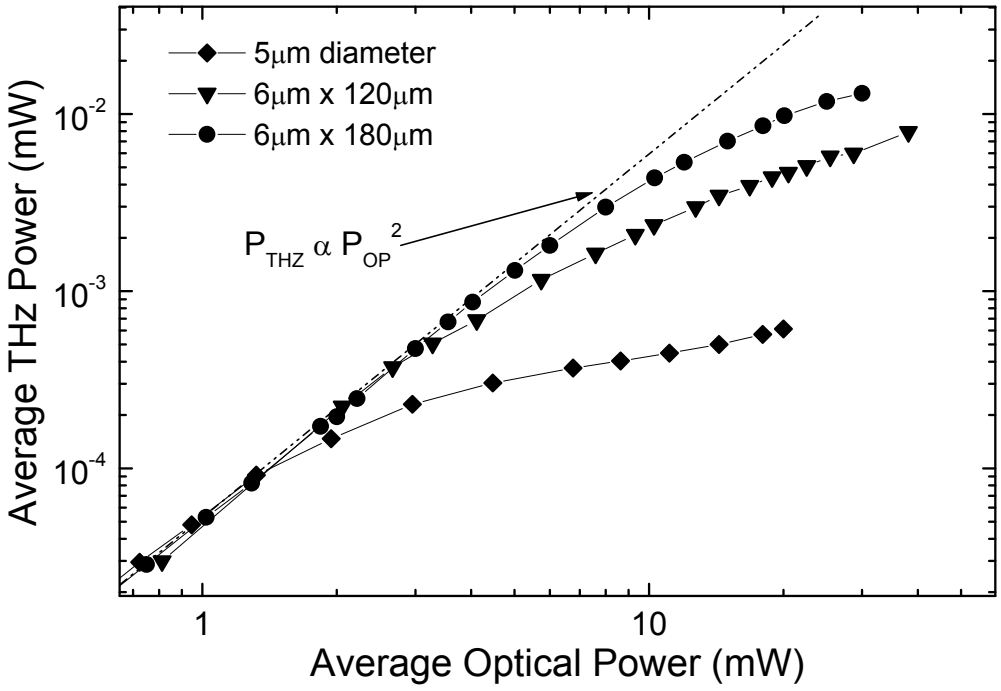

Figure 39. Experimentally observed THz power using a point excitation and spatially extended line excitations. Dashed line indicates the expected square law dependence.

Figure 40 displays other THz PC sources with an optical excitation power and a corresponding THz power. The efficiency, defined as the incident optical power to THz radiation power ratio, is also shown. The power supply ultimately supplies the necessary energy to the overall THz radiation. In fact, the Larmor result predicts a square dependence of the total carrier acceleration that is principally supplied by residing field strength. Therefore, the fact that high efficiency is reached at lower optical illumination without a high voltage DC power supply adds significance beyond the efficiency quoted.

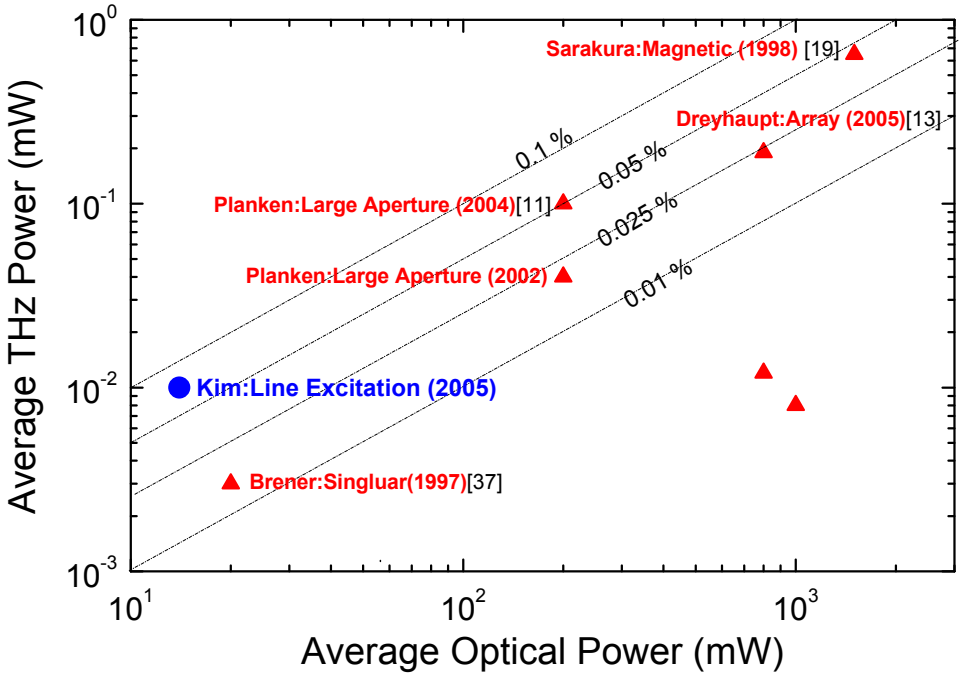

Figure 40. THz efficiency comparison with other photoconductive source types.

5.1.3. Line Excitation Scaling

The point excitation saturation fluence of 97 μJ/cm^2, which is independent of bias field, agrees with previous reports that range from ~40 to 280 μJ/cm^2 [30, 32, 49]. The saturation fluence of 14 μJ/cm^2 and 20 μJ/cm^2 for the 120-μm and the 180-μm line excitations respectively, do not scale directly with area compared to the point excitation because of the one dimensional uniformity of line excitation, which results in larger average charge densities. This result is confirmed by the numerical results that we present in the next section. We do observe, however, that THz power saturation from line excitations scale with line length for line excitations to 180μm in length.

5.1.4. Line Excitation Limitation

The line excitation demonstrates the scalability of the THz power, but it does not exactly follow the saturation fluency of the point excitation result. One reason is that line excitation retains a Gaussian density profile. Longer lines do not produce a commensurate increase in THz power because of the decreased collection efficiency of the silicon collimating lens. Alternate collection structures such as cylindrical collimating lenses should allow improved collection efficiency when using longer line excitations. Also, it is expected that the lines longer than a half wavelength demonstrate an interferometric effect on the total average power.

THz energy originates from the energy stored in the electric field of the electrode structure. We have separately analyzed the energy available for THz radiation by accounting for all energy paths including kinetic, thermal, and radiative. We find the stored energy is ~1 pJ/μm of anode length which is more than sufficient to support the measured 0.12 pJ per THz pulse.

5.2. Hydrodynamic Model Analysis (HDM)

There have been only limited reports regarding optimization of THz power efficiency [50] although some of the limitations due to screening effects have been considered [51, 52]. Here we report the results of a two-dimensional multi-band hydrodynamic model of the transient transport and quantitatively identify the effects of transport, spatial non-uniformities, space-charge screening, radiation field screening and spectral filtering effects. We find that our numerical assessment of the THz power predicts our experimental results with excellent quantitative agreement. The role of space-charge screening, radiation field screening, spatial non-uniformities, and spectral

filtering was investigated by a two-dimensional analysis of the PC THz sources based on a hydrodynamic model (HDM) of highly non-equilibrium carrier dynamics [53].

5.2.1. Hydrodynamic Model Description

A 2-D HDM of the photoconductive source is developed based upon a hydrodynamic model of carrier dynamics [54]. HDM yields conservation equations for carrier density, energy, and momentum of the carrier ensemble for each of the Γ, X and L bands [55]. The accuracy of the HDM arises from the use of Monte-Carlo simulations to determine the energy dependent scattering rates found in the rate equations. The speed and efficiency of the HDM enable the modeling of extended structures that require distinct transport solutions across the area subject to non-uniform photo-excitation and nonuniform screening. Using the HDM, we determine the transient electron density, ensemble drift velocity, and average energy on a 1μm × 1μm grid. The HDM self-consistently computes the effects of the screening fields using a time step of 0.1fs. The carrier dynamics are classified in two regimes. During the first ~100fs (velocity overshoot regime), the electrons initially accelerate quasi-ballistically, and then scatter to L and X bands, producing a strong velocity overshoot and recovery. In the second regime, space-charge screening increases with increasing carrier density, producing a collective plasma oscillation [28]. More detailed information are included in appendix II.

5.2.2. Screening Effects: Space-charge & Radiation Screening

The space-charge screening is given by $E_{\text{space charge}} = \eta_{sc} P/\varepsilon$, where P is the local polarization density and ε is the dielectric constant of the GaAs substrate. The screening efficiency, η_{sc}, is less than unity because of the metal-semiconductor interaction and

retardation effects. Importantly, the space-charge screening produces a net carrier acceleration that varies with carrier density. As a result, the contribution to the radiated power varies across the emitting area.

Screening the bias field may also result from the near-field electric field (radiation screening) given by $E_{\mathrm{NF}} = \eta_{\mathrm{rad}}\,\eta_0 J_s \Big/ \left(1+\sqrt{\varepsilon}\right)$, where J_s is local surface current density and η_0 is the free space impedance. The radiation screening efficiency, η_{rad}, depends on aperture geometry and has been shown to be exactly unity for the large apertures source [32]. The effective electric field acting on the carriers is updated at each grid point using the initial static TEF and the two screening fields. The summation of the weighted ensemble electron acceleration at each grid point is used within the Larmor result to determine the total radiated power. The simulation exhibits the best fit with the measured result when $\eta_{sc} = 0.15$ and $\eta_{rad} = 1$.

5.2.3. Numerical Estimation and Experiment result comparison

Figure 41 shows the numerical estimates of the effects of screening and filtering mechanisms for a Gaussian point excitation. The experimentally observed THz power is also shown. For absorbed optical power less than 1 mW, the screening effect is negligible for both the simulated and experimental THz powers. Consequently, THz powers increase as the square of the optical power, which is consistent with the Larmor result. The simulated THz power includes all mechanisms except the collection efficiency since we are interested in the total power in the freely propagating beam. Thus the numerical estimate is the maximum power that we expect to be able to detect at the bolometer. There are few attempts to quantitatively compare simulations with measured

THz power and considering that there are no adjustable parameters in the low-power regime, our observation of 10-20% collection efficiency is very good. Ultimately, the collection efficiency is limited because of imperfect collimation and diffraction of the silicon lens.

The saturation from space-charge screening for powers above 1 mW results from spatial inhomogeneities in the carrier distribution and the corresponding variation in plasma frequency. Thus the ensemble behaves incoherently in the plasma oscillation regime (dashed-dot). Radiation screening reduces the THz power generated at higher optical power (short dash). Frequency-dependent attenuation resulting from multi-phonon absorption in the substrate and the bolometer low pass filter contributes to the spectral filtering. The increase in plasma oscillation frequency at higher optical powers together with spectral filtering results in an apparent saturation in the measured THz power (solid line). These effects each contribute to the saturation observed. Importantly, we have treated both space-charge screening and radiation field screening mechanisms in TEF PC antenna.

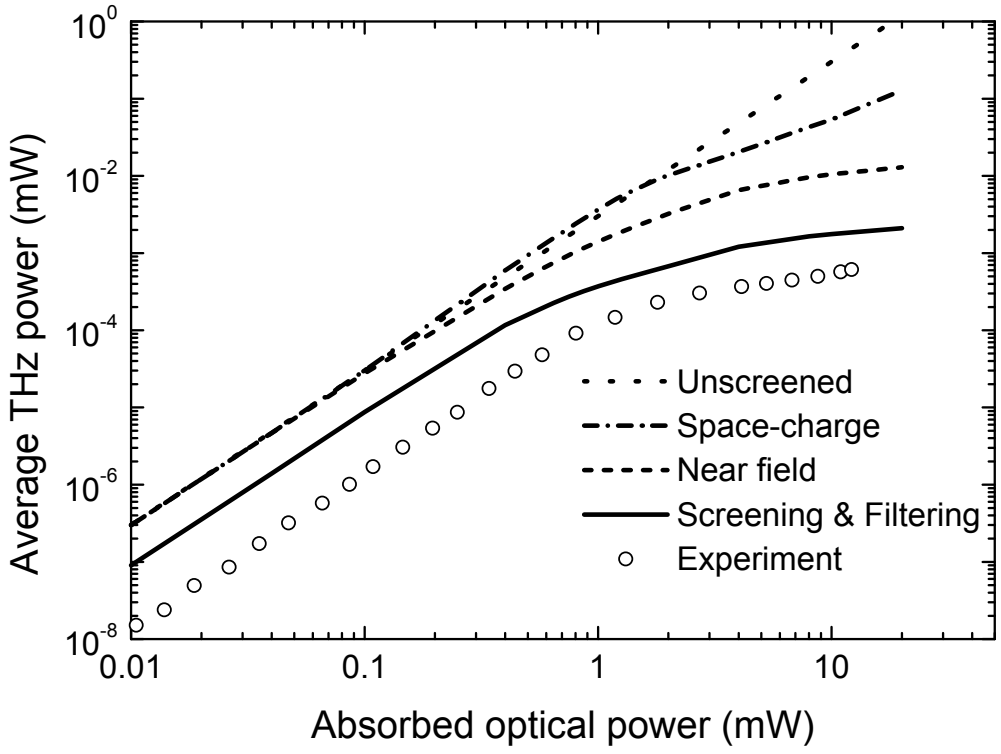

Figure 41. Hydrodynamic model of THz power for unscreened, space-charge screening, near-field radiation screening, and both screenings with spectral filtering. The experimental result is also shown.

5.2.4. HDM Line Excitation Analysis

Using the hydrodynamic screening model, we also estimate the THz power generated using a line excitation. Figure 42 shows the same close agreement with the experimental result as shown for the point excitation. Importantly, the screening parameters used in the numerical simulations are the same as in the point excitation. The constant efficiency contours in Figure 42 demonstrate experimental efficiencies near 0.1%. We also note that for each of the three excitation geometries, the onset of saturation occurs near a carrier density of $3x10^{18}$ cm^{-3} and power saturation from line excitations scale with line length. However, the use of line excitations longer than 180 μm did not produce a commensurate increase in THz power. This results from decreased

collection efficiency of the silicon collimating lens when exciting long lines. Alternate collection structures such as cylindrical collimating lenses should allow improved collection efficiency when using longer line excitations, leading to efficiencies greater that 1 % and power greater than 1 mW.

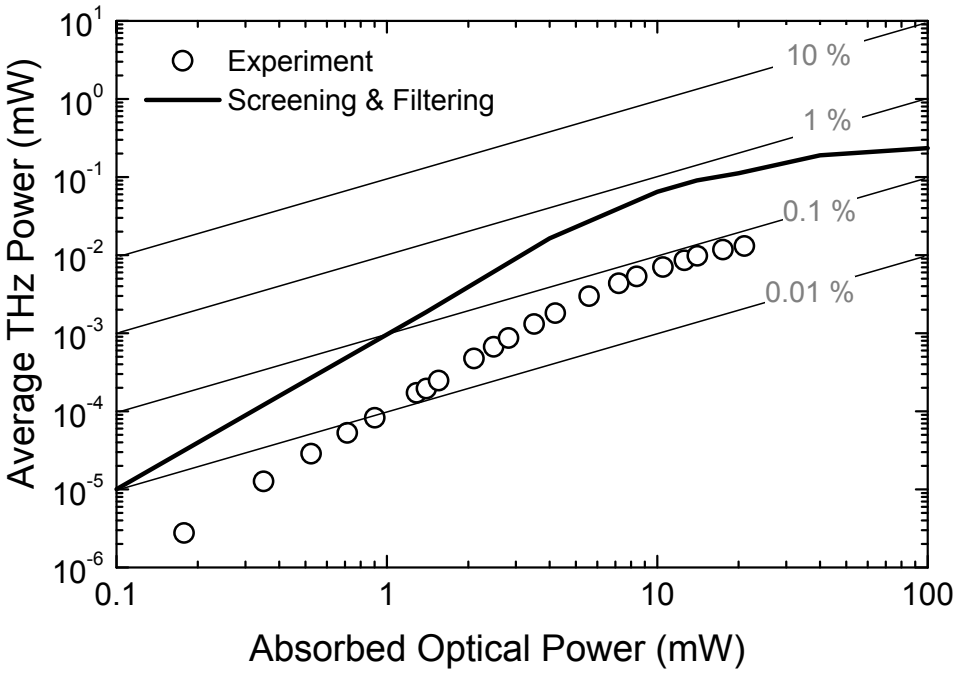

Figure 42. Numerical simulation and experimentally observed THz power for 180 µm line excitation. Constant efficiency contours are also shown.

CHAPTER 6: Spectral Analysis: Point & Line Excitations

While the line excitation provides significant improvements in total THz power and scalability, it cannot be a suitable substitution if the spectrum of the line excitation is different from that of the point excitation. This chapter investigates the spectrum of both a point excitation and a line excitation using THz optoelectronic interferometry. Both spectrums are obtained experimentally. Not only does the line excitation produce comparable frequency content across the majority of the spectrum, it also produces extended low frequency content compared to the point excitation. This result is attributed to the enhanced directivity of the line excitation.

6.1. *THz Optoelectronic Interferometry*

Interferometry is a technique used to compare two or more waveforms by superimposing the waves. Relative phase information can be retrieved by introducing a temporal delay. The most common interferometric method is the Michaelson interferometer. The THz-TDS has been the most popular method of THz spectral analysis because the THz-TDS directly measures the electric field response. The bandwidth of the THz-TDS, however, is limited by the bandwidth of a photoconductive receiver. In order to investigate the spectral content of the line excitation, we use the previously reported two-source optoelectronic interferometry setup [56]. When properly

aligned, this method has excellent bandwidth that is not limited by the bandwidth of a photoconductive receiver, which is required for the spectral analysis of broadband sources [7].

6.1.1. Experimental Setup

A THz PC source is constructed using the same geometry as previously described, a single electrode pair deposited on semi-insulating GaAs. The incoming optical excitation is split into two separate beams before each beam enters the setup. For point excitations, we estimate the spot diameter to be ~5 μm. For a line excitation created with two crossed cylindrical lenses, we estimate the excitation area to be ~6 μm x 180 μm. The same type of microscope objective and the same set of cylindrical lenses are used for all excitation geometries. The THz radiation was collimated using a hyper-hemisphere silicon lens attached to the back of the GaAs source chip with 60 V bias [7,9]. The freely propagating beams from two separate THz sources are combined using a double zone refined high-resistivity (10 kΩ·cm) silicon beam splitter at 45° (~50-50 split) to provide collinearly propagating beams to the calibrated liquid-helium-cooled bolometer, which is located 200 mm from the THz sources, shown in Figure 43. Interferograms are obtained by measuring the amplified bolometer output using a lock-in amplifier, while a high-resolution linear mechanical stage is used to provide a temporal resolution of 33 fs with an integration time of 100 ms for each point. The interferometry setup is located inside a box in order to allow a nitrogen purge to minimize the THz absorption by water vapor [57]. The bolometer detector window is also directly connected to the box to allow purging as well.

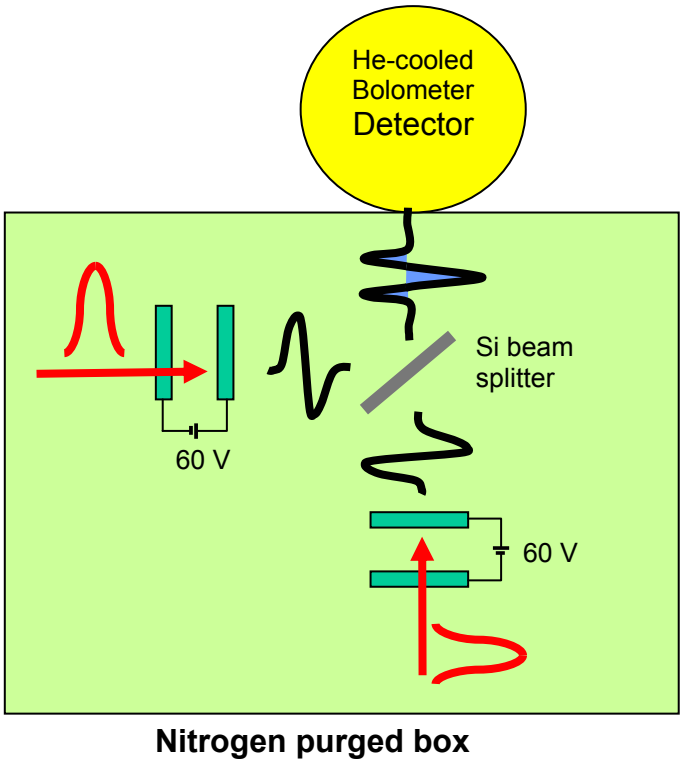

Figure 43. THz Optoelectronic Interferometry Setup.

The THz optoelectronic interferometry is a cross-correlation from a signal processing point of view where $E_{THz1} \neq E_{THz2}$ where E_{THz1} and E_{THz2} represents THz emission from each source. In this experiment both sources and excitations, which determine the spectrum, are under the same condition $E_{THz1} \cong E_{THz2}$. Under this assumption, the obtained interferogram is an autocorrelation of the THz pulse:

$$A(\tau) = \int_{-\infty}^{\infty} I(t)I(t-\tau)dt \qquad (6.33)$$

where $I(t)$ is the detector response. Subsequently, a Fourier transform of the interferogram reveals the power spectrum of the THz source based on the convolution theorem:

$$G^{(2)}(\omega) = \int_{-\infty}^{\infty} A^{(2)}(\tau) e^{-j\omega\tau} dt \tag{6.34}$$

In fact, a point excitation spectrum obtained from this setup demonstrates a comparable power spectrum with other published records of the same THz source structure. $G^{(2)}(\omega)$ contains no phase information, solely providing the power spectrum; therefore, the power spectrum is the only comparison made here for the two excitation geometries. Optoelectronic interferometry, however, is capable of obtaining a complex index of materials when a reference and transmitted interferogram are available. [Appendix III]

6.1.2. Enhanced Low Frequency Content

Figure 44 shows experimentally obtained interferograms for (a) the point and (b) the line excitation. Both interferograms exhibit ~320 fs FWHM with an excellent extinction ratio, which indicates good wavefront matching. Oscillations at longer delay result from residual water absorption because of an insufficient purge. Importantly, all the experimental conditions are the same except excitation geometry for two interferograms.

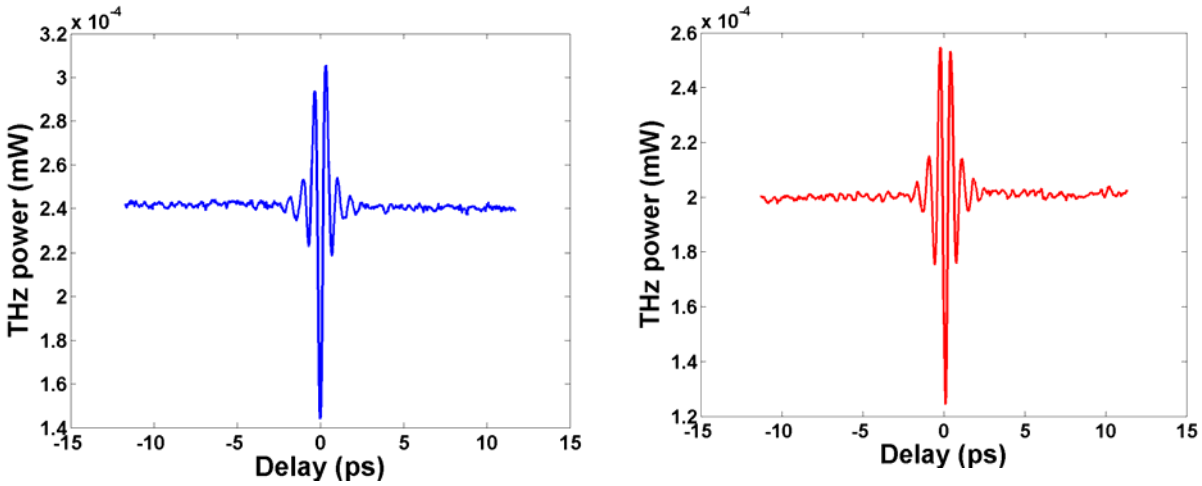

Figure 44. Experimentally obtained interferogram of (a) the line excitation and (b) the point excitation geometry.

Figure 45 shows the relative THz power spectral density of both excitation methods, obtained via the numerical FFT of the interferograms. The line excitation clearly exhibits ~ 50% or more improvement in the low frequency (up to 1.1 THz) compared to the point excitation, thus expanding the overall useful bandwidth beyond the point excitation spectrum. This observation was independent of particular alignment and excitation intensity. This result is significant for the measurements that require the investigation of lower-frequency content since the line excitation already demonstrated more than an order of magnitude improvement in total THz power. Therefore, the power spectral density in this regime can reach up to 15 times that of the point excitation.

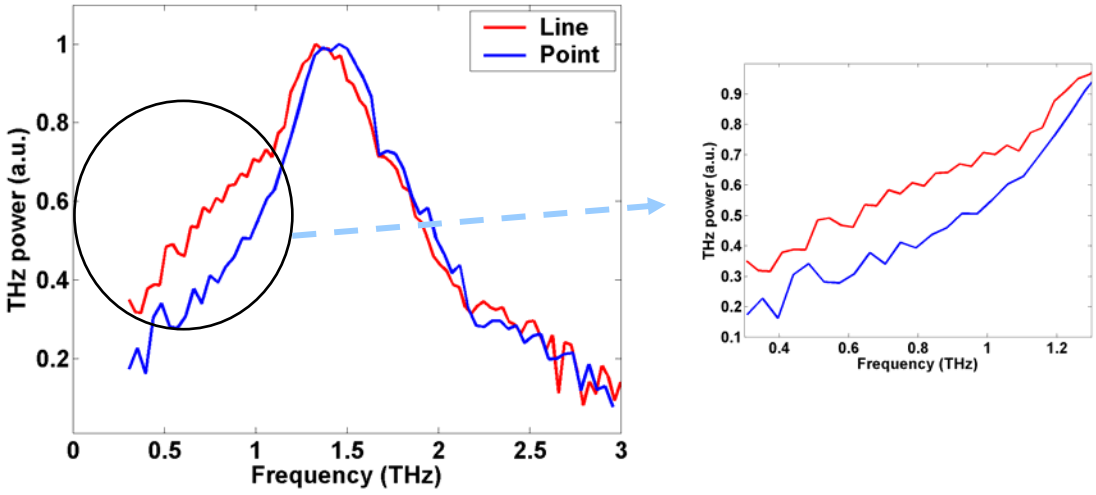

Figure 45. Line and Point excitation spectrum obtained from numerical FFT of the measured interferogram.

6.2. *Enhanced Directivity of the Line Excitation*

The enhanced low-frequency content of the line excitation can be understood in terms of the enhanced directivity of the line source. Specifically, the directivity of the line excitation allows higher collection efficiency in the low-frequency region. The experimental data show greater improvement as the frequency decreases.

The point source results show a divergence similar to that reported by Jepsen who has reported that the main lobe can be described via Gaussian beam optics to have a wavelength-dependent divergence angle of $\theta = 83 \cdot \lambda$ with a beam waist w_0=3.82 mm for a lens with diameter 5.0 mm[8]. For our geometry, this suggests that wavelengths lower than 1.1 THz experience significant attenuation as a result of diffraction. Thus, an enhanced directivity will preferentially enhance the collected power for wavelengths longer than 1.1 THz. This is consistent with the results of Figure 45.

6.3. Plasma Oscillation

The usefulness of the line excitation is limited if the spectrums has the excitation density dependence. There have been reports optical excitation dependence of THz spectrum. The photo-carriers are initially separated and pulled by an existing field. Then the restoring force causes carriers to go through plasma oscillation with a frequency represented by:

$$\omega = \sqrt{\omega_p^2 - \frac{\gamma^2}{4}} \tag{35}$$

and the plasma frequency:

$$\omega_p = \sqrt{\frac{ne^2}{\varepsilon\varepsilon_0 m^*}} \tag{36}$$

where the plasma frequency ω and damping rate γ [29]. These equations suggest that the center frequency of the spectrum increase with the increasing carrier density. The THz spectrum for both the point excitation and the line excitation did not show any significant change even when the optical pump power increased more than ten- fold, as shown in Figure 46. We note specifically that we observe neither changes nor plasma oscillations at high pump powers. The uniformity of the spectra extends beyond the intensity where the power saturates. Thus, both radiation screening and charge screening do not appreciably change the radiation signature in these sources.

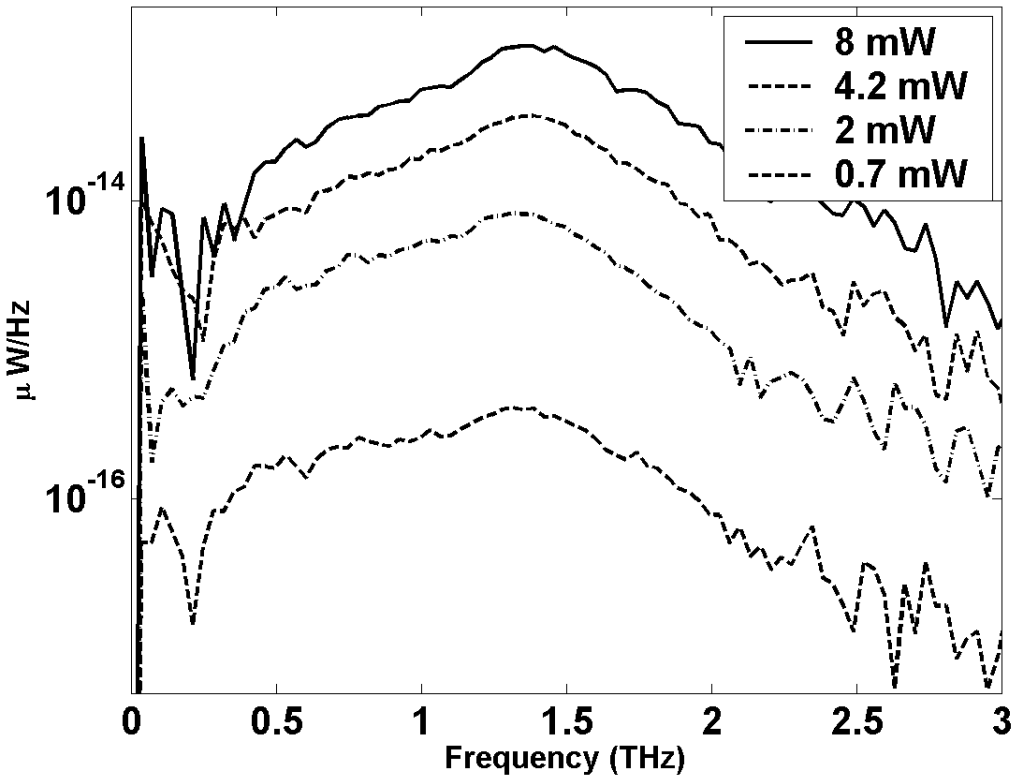

Figure 46. Power spectral density of the line source excitations with increasing optical pump power. The optical power is held same for each THz source.

These improvements are inherent to the line excitation source geometry itself, so it can be easily implemented for other THz spectroscopic applications using the photoconductive antenna as the THz pulse source, without adding any complex equipment besides substituting the microscope objective with two cylindrical lenses.

6.4. Summary

The first THz line excitation interferogram is presented. The line excitation spectrum exhibits enhanced spectral intensity in comparison to a point excitation in the frequency region below 1.1 THz. We also demonstrate the insensitivity of the spectral content to excitation intensity.

CHAPTER 7: THz Line Excitation Array

The line excitation successfully demonstrated its effectiveness in reducing the space-charge screening, but the scalability of the line excitation only for the line length up to the half of the longest wavelength. Therefore, the next logical path to improve THz power and efficiency is the array excitation.

This chapter introduces the TEF THz line excitation array in interdigitated format. Unlike other THz sources, where the high field strength is achieved by a small gap and a high bias, the array introduced here utilizes TEF field strength to improve the efficiency of overall system. In addition, an array lens controls the optical injection into a high field region. Experimental power scaling of TEF THz array is demonstrated. An experimental investigation of 40 μm and 90 μm THz array results is presented. A direct comparison between a single pair source and the array is included to discuss the THz array limitations.

7.1. Scaling of TEF THz Line Excitation Array

7.1.1. Expected Array Performance

The line excitation successfully demonstrated its effectiveness in reducing the space-charge screening. The scalability of the line excitation only extends to the line length up to the half wavelength. Therefore, the next logical path to improve THz power and efficiency is the array excitation.

We can consider simple linear array theory to estimate the expected THz power improvement from an array. Assume that the radiated THz field from an element is defined as $\vec{E}_n = AE_n(\theta_n, \phi_n)$ where A is a field magnitude. If we assume that all the elements produce the same radiation in the same polarization as illustrated in Figure 47, the far field radiation is:

$$\vec{E}_n = A\frac{e^{-jkr}}{r}E_n(\theta_n, \phi_n) \times AF \tag{7.37}$$

For N number of linear array elements with the separation, d, array factor, AF, wavevector, k, and the phase difference, β , the array factor is:

$$AF = \sum_{n=1}^{N} e^{j(n-1)(kd\cos\theta+\beta)} \tag{38}$$

Therefore, the total field of an array is a vector superposition of the radiated field of each array element. An array can effectively increase the total radiated average power as well as increase the directivity by controlling a phase term. If $\beta = 0$ and $\theta \cong 0$, then the amplitude of the far-field radiation becomes AN. The THz power then become $P_{THz} \propto \left|E_n\right|^2 = A^2N^2$. If this scaling law holds, then scalability of the line excitation with just 10 THz elements can generate ~1 mW of THz power.

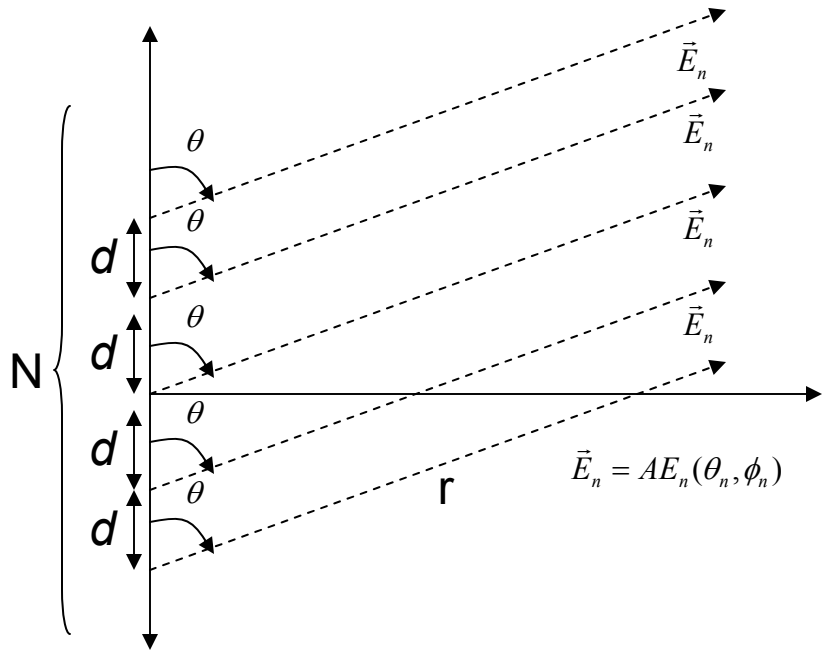

Figure 47. Linear array schematic.

7.1.2. Trap-enhanced field in THz Array

A critical requirement of a highly efficient compact THz photoconductive source is to maintain TEF as described in previous sections. Therefore, the existence of high field region of TEF in THz array is important to maintain high efficiency.

7.1.2.1. Experimental Setup for THz Array Field Scan

The 40 μm THz source array consists of twenty 10 μm wide and 2 cm long coplanar metal electrode pairs that are separated by 40 μm and deposited on semi-insulating GaAs. Similarly, The 90 μm THz source array consists of 10 μm wide and 2 cm long coplanar metal electrode pairs that are separated by 90 μm and deposited on semi-insulating GaAs. These designs resemble a single pair THz PC source except that they are in an interdigitated array form. The array spacing is determined to fit the available off-the-self cylindrical micro-lens of 100 μm and 200 μm pitch. The THz array

source is illuminated by 75-fs pulses (800nm) generated by a Ti:Sapphire oscillator. A 20X microscope objective is used to focus the beam into a ~6 μm spot. This focused spot is scanned across the THz array perpendicular to array element pairs using a Labview-controlled motorized actuator (Newport CMA-25CCCL) with 1 μm increment. THz radiation with respect to the scanned position is directly recorded using a calibrated liquid-helium-cooled bolometer and lock-in amplifier. The Si lens is removed to eliminate frequency dependent collection efficiency. The recorded THz power is directly related to the field strength of the scanned position.

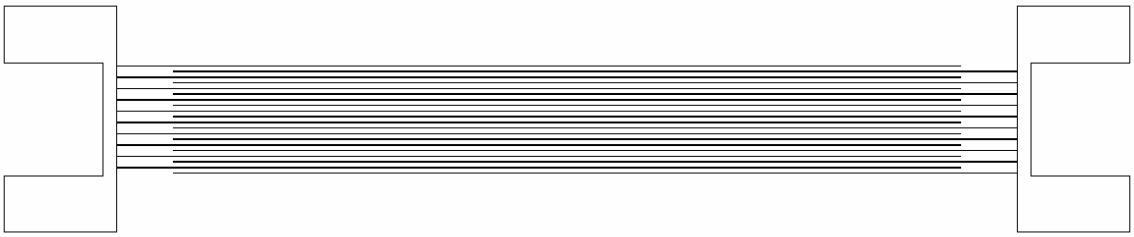

Figure 48 TEF THz array design. The 90 μm gap source is shown. Two pads at each end of the array are directly connected to the DC power supply

7.1.2.2. Trap Enhanced Field in the Array

To improve total average THz power, while maintaining high efficiency of the line excitation, requires the existence of TEF. Figure 49 shows the anode section of the 90 μm THz array scan. This result clearly identifies the field enhancement of TEF at both edges of the anode extending ~10 μm, which is consistent with a single pair result. The enhancement, however, is not as pronounced as a single pair that produced more than three order of magnitude difference in total radiated THz power as described in the chapter 6. The 40 μm THz array scan has also provided the similar anode field enhancement.

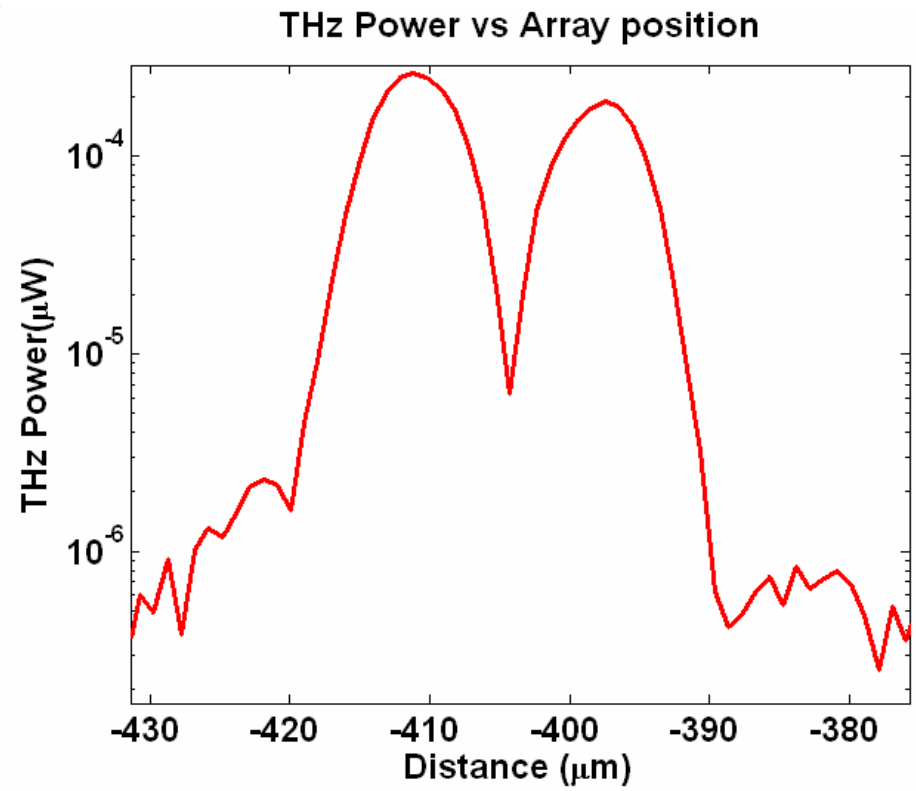

Figure 49 Anode scan of THz array source with a point excitation

7.2. THz Array Power Scaling

One of the assumptions of the THz array power scaling is a constructive interference of THz emission from each element. A focused normally incident optical excitation has a short pulse in the order of ~100 fs, which means that no phase difference for each element, $\beta = 0$, can be assumed. Therefore, each additional THz array element should constructively interfere. The separation between the array elements is determined by an array lens. The array factor shows that the smaller the distance between the array elements the more efficient the array is, $\theta \cong 0$. When the number of array elements or the separation increases, the interference needs to be considered.

7.2.1. Experimental Setup

The THz source array consists of twenty conventional 10 μm wide coplanar metal electrode pairs, separated by 40 μm and deposited on semi-insulating GaAs. The THz array source is illuminated by 75-fs pulses (800nm) generated by a Ti:Sapphire oscillator. One cylindrical lens is used to focus the beam width to ~150 μm. An orthogonally-oriented cylindrical micro-lens array with 100 μm pitch is used to create an array of 15 μm x 150 μm line-shaped regions. The excitation beam array is positioned near the anode of each electrode pair. Another advantage of this configuration compared to previously published THz arrays is that all of the optical excitations are directly injected into the high field region, increasing the efficiency. THz radiation is directly measured using a calibrated liquid-helium-cooled bolometer and lock-in amplifier.

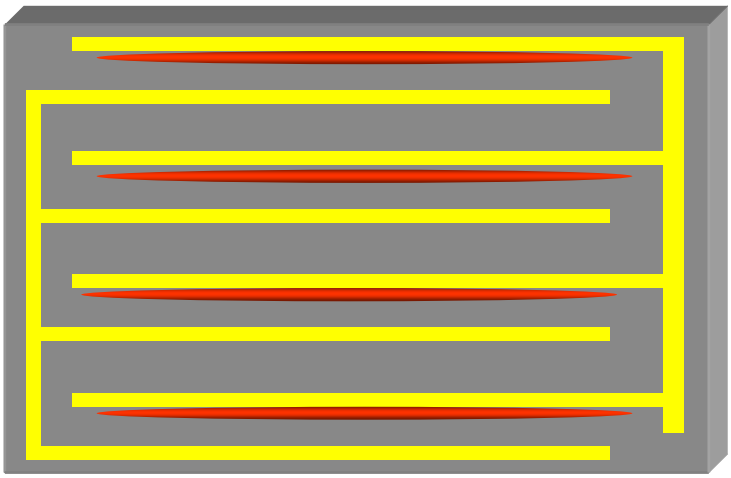

Figure 50 THz array scan by array excitation

To compare the THz radiation generated by an increasing number of THz antenna elements, we accurately scan the THz array source in a direction perpendicular to the linear electrodes. A motorized actuator moves the THz array source in 1 μm increment.

This process effectively adds (or removes) additional electrode pairs one at a time as well as positioning the array beam across the THz array. No silicon lens is used on the backside of the GaAs. While sacrificing the total amount of THz power coupled into free space, the collection efficiency sensitivity of the Si lens focusing and collimating properties is eliminated.

Figure 51 shows the measured THz power vs. scan position. The THz power decreases with the decreasing number of array elements illuminated. The THz power represented in the figure is a superposition of each THz array element. The plot clearly identifies the enhanced anode, insulating, and cathode regions with a resolution high enough to identify both edges of the anodes.

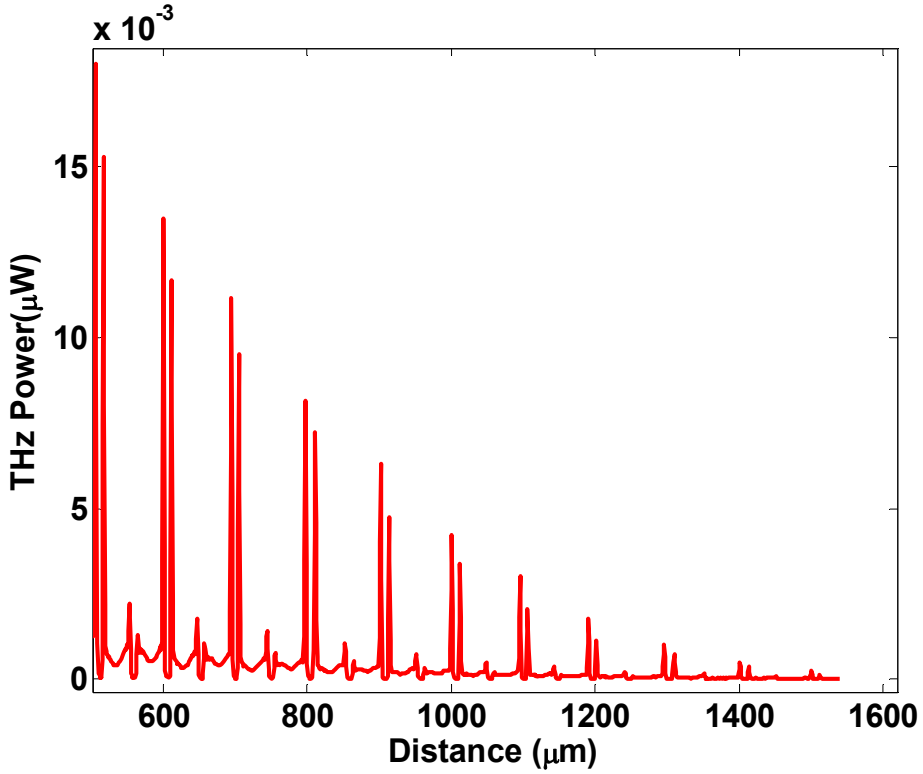

Figure 51. THz power vs. position of the scanned micro-lens array and the zoomed in anode scan.

7.2.2. Array scaling and Gaussian Beam profile

To estimate the power scaling of THz array, numerical analysis is necessary to assess the efficiency of constructive interference. Figure 52 shows the total average THz power obtained from the peak anode illumination. Three regions are observed, increasing, overlapped, and decreasing corresponding to the number of illuminated antenna elements.

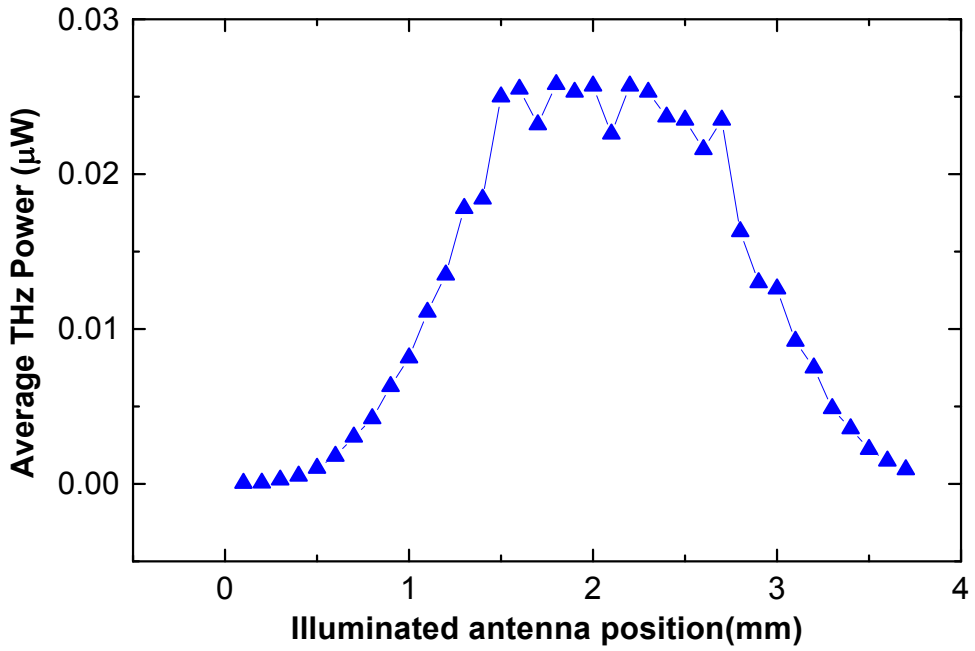

Figure 52 Average THz power at anode vs. number of antenna elements illuminated

The increasing region reveals that the THz power scales more than quadratically, seemingly in contradiction with the Larmor result and the array power scaling. The Gaussian beam profile results in larger optical power on the center of the micro-lens array. Hence, larger carrier densities exist at the focus of these lens elements. THz power is the highest at the center part of the lens and decreases as it deviated from the center illumination. This increases the THz power more than quadratically as more elements are illuminated.

A numerical analysis of Gaussian effect together with the anticipated quadratic behavior of the array and THz power is shown in Figure 53. The results follow the measured data closely. The normalized behavior of Figure 53 reveals that the measured data closely follow the slope of the numerical estimate. If the Gaussian profile of the excitation beam is excluded, the array follows the scaling law as expected, thus demonstrating that the array power does indeed scale quadratically with number of elements illuminated. The spot size at the lens array was measured and the total THz power was determined without any adjustable parameters.

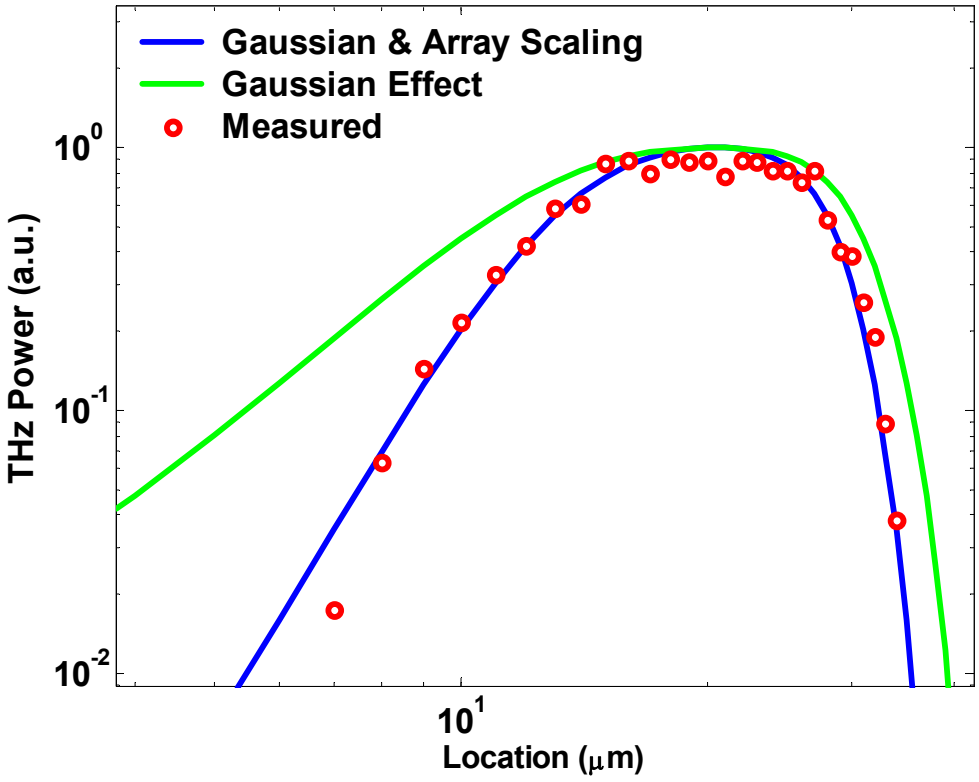

Figure 53. Measured response compared to the computed Gaussian illumination effects and combined Gaussian and array scaling.

7.2.3. Weak Array Field Strength

While the THz array demonstrated the power scaling with respect to the number of array elements, it did not to scale relative to the single pair line excitation performance

failing to reach anticipated mW power level. In order to directly compare the THz power, the 40 μm single pair THz source along with a 40 μm array was fabricated. Both the THz array and the single pair were designed on a single mask and processed on a single wafer. Both 40 μm gap single pair and 40 μm THz array pairs are illuminated by 75-fs pulses (800nm) generated by a Ti:Sapphire oscillator. A 20X microscope objective is used to focus the beam into ~6 μm spot.

Figure 54 shows the measured THz power vs optical excitation power for both the array and the single pair. While both results exhibited similar saturation behavior, the point excitation THz array produced significantly less THz power than the single pair. All the other experimental parameters remained the same for both measurements. Only the source is replaced leaving all other experimental setup unchanged. It is clear that the electric field strength of the THz array is weaker than the field strength of single pair THz source.

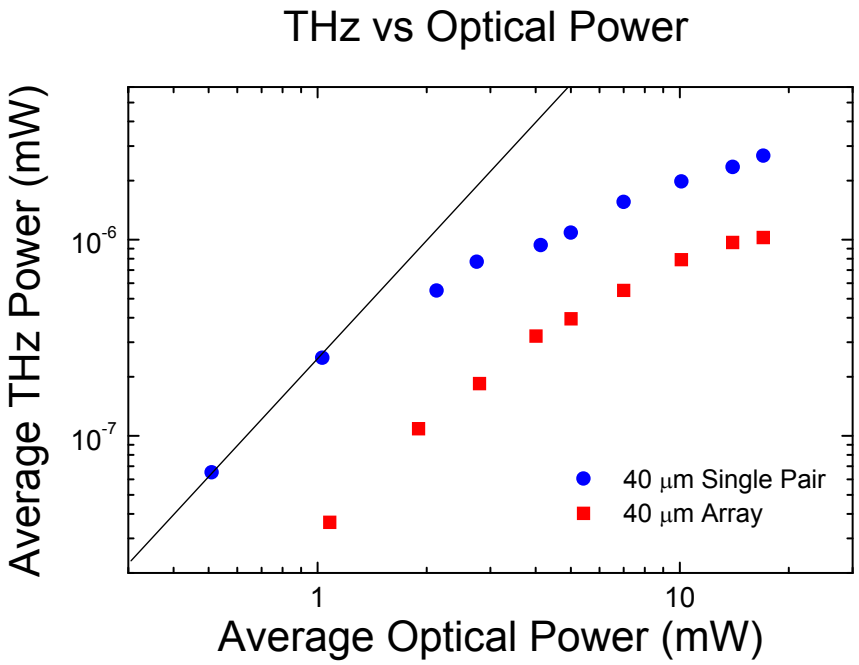

Figure 54. Experimentally observed THz power using a point excitation of 40 μm gap single pair source and a 40 μm gap array.

One of the characteristics of the field enhancement of TEF is a dependence on the electrode gap. It has been experimentally determined that the field enhancement is most pronounced at a 80-μm gap. 40-μm spacing also limited the amount of DC bias voltage only up to 40 V. The same set of experiments as previously described are carried out in

order to directly compare the 90-µm array, 40-µm single pair, and 90-µm single pair THz sources. Again, all the experimental and fabrication parameters remain the same except the wider 90 µm spacing of a single pair and the THz array design.

A 90-µm THz array again exhibited weaker THz power than other two single pair sources. Figure 55 shows that the point excitation of both 40 µm and 90-µm geometries generated comparable THz power. While a small discrepancy in THz power between the 90 µm and 40 µm single pair performance exists, it is not sufficient to explain the low power of the 90-µm array. This result further suggests that the THz array has less electric field strength than that of a single pair.

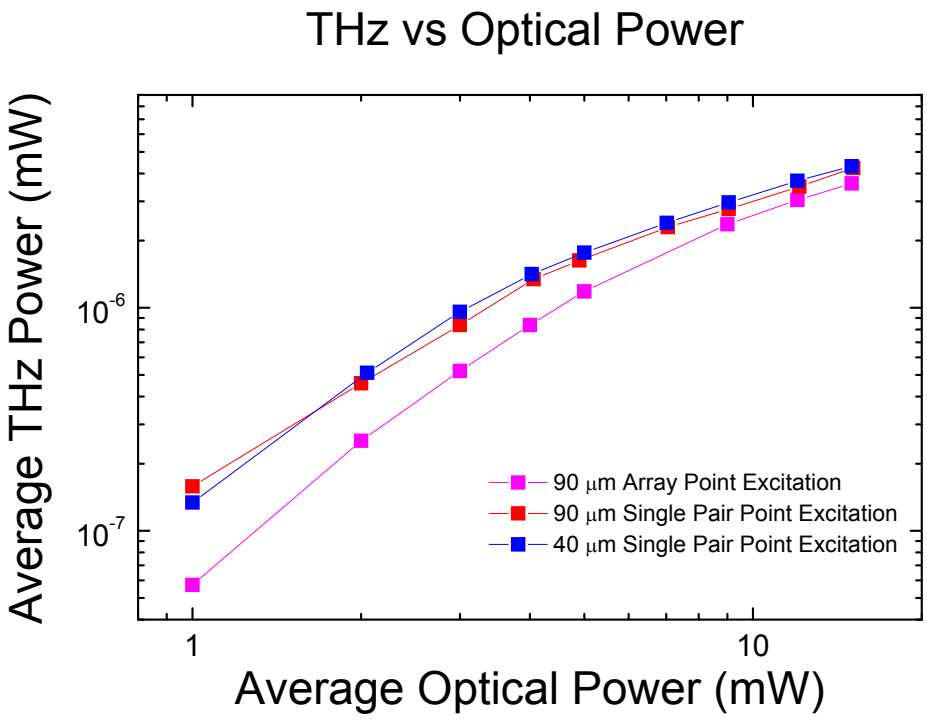

Figure 55. Experimentally observed THz power using a point excitation of 40 µm and 90 µm gap single pair sources, along with a 90 µm gap array.

On a separate experiment, the 90-µm array has been scanned perpendicular to the electrodes with a LabView-controlled Newport micro-actuator with 1 µm resolution. The

silicon lens was removed to avoid any position-dependent collection effects. Figure 56 shows the performance of each element of the 90 μm array. It clearly identifies the anode region exhibiting little difference among them with high signal to noise ratio. Mutual coupling between the array elements can cause the displaced phase center antenna main beam shapes to become amplitude and phase mismatched. The fact that there are no noticeable differences in performance of both the edge and center implies that there is negligible mutual coupling. Again, the weaker THz power performance of array seems to point to the weak field strength.

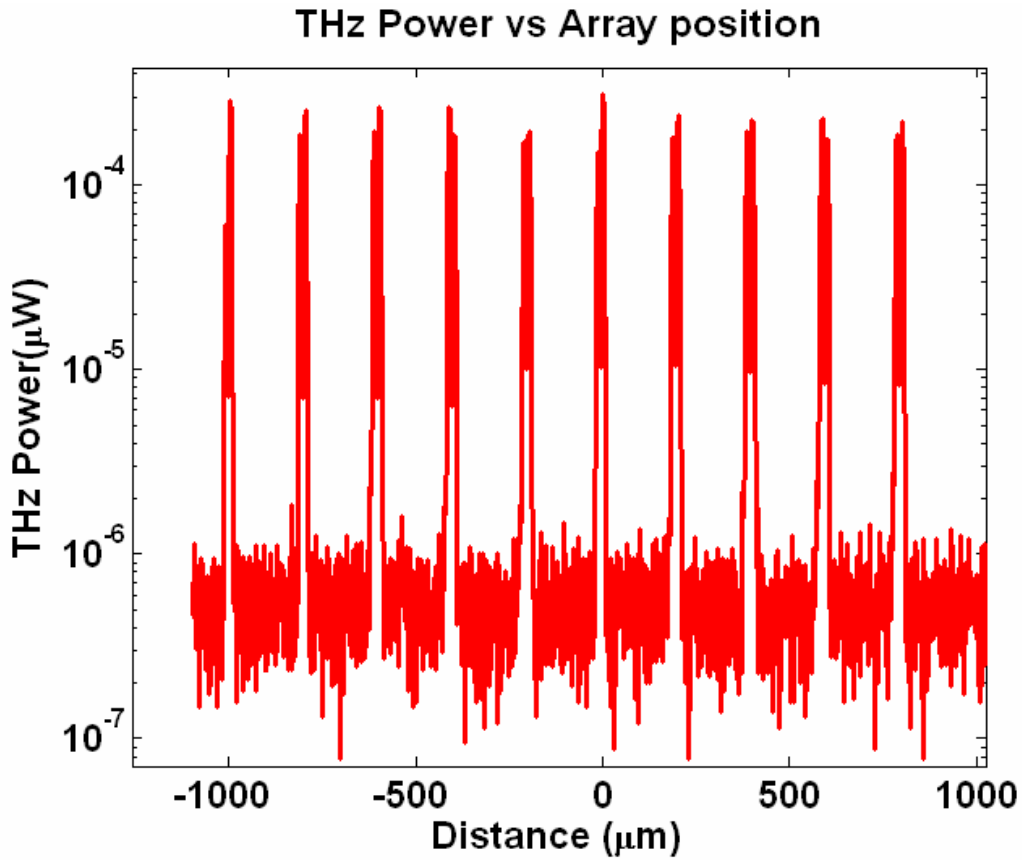

Figure 56. Experimentally observed point excitation THz power scan across the 90 μm THz array.

7.3. Capacitance Relation to THz array

The TEF THz array of both 40 μm and 90 μm geometries failed to produce the expected power. The experiment revealed that the magnitude of the TEF, while existing, decreased significantly. One possible reason for this unexpected weakening of TEF field in array format is capacitance. While the THz generation process itself is not sensitive to the total capacitance, regenerating TEF can be directly influenced by the total capacitance. The increased total capacitance can multiply the recovery time beyond the incoming optical pulse frequency of 82 MHz (12.2 ns). The metal deposit of the electrode on semiconductor is effectively a one-sided planar capacitor. Increasing the number of electrodes naturally increases capacitance. DC capacitance measurements, however, do not necessarily correspond directly with the capacitance under bias and under illumination.

7.3.1. Experimental Setup: Photocurrent Response

To estimate the capacitive behavior of THz PC sources under ultrafast excitations, a photocurrent measurement is constructed. The THz source array consists of conventional 10 μm wide coplanar metal electrode pairs, separated by 40 μm in an interdigitated format and deposited on semi-insulating GaAs. Two different arrays with 10 and 25 array elements are prepared under the same conditions. Also, one ten pair array is cleaved to make a three pair array source. An equivalent single pair is also measured. Each THz source is illuminated by 75-fs pulses (800nm) generated by a Ti:Sapphire oscillator. A point excitation using a microscope objective injects optical carriers near the anode. In order to provide a DC bias and extract AC current response from THz source, a bias tee is used. The bias tee is a three-port device that contains an

inductor and a capacitor. It allows a DC bias feed to a port that connects directly to a THz source, while the capacitor port filters out the DC part and collects the AC response. Upon optical pulse excitation, injected carriers generate a photocurrent that is directly measured by a sampling scope, a Tektronix 11801B with SD26 20 GHz sampling head through a bias tee. Both the bias tee and the scope have more than 20 GHz of bandwidth. The average optical power of 5 mW is used in all measurements.

7.3.2. Photocurrent Response Analysis

Figure 57 shows directly measured photocurrents from each THz source. There are several immediate observations. The first observation is the decreasing amplitude of peak with the increasing number of array pairs, which is consistent with the decreased field strength of the THz arrays measured. The second observation is that the rise and fall time of the photocurrent is increasing with the number of array pairs. This result can be explained by an increased capacitance under biased condition. Upon an optical excitation, the residing field collapses as the currents are collected through each electrode. It is obvious from the Figure 57 that even with 10 pairs the electrode rise time slows down significantly. This could be also a cause of reduced field enhancement if the TEF regeneration time requires a recharge of capacitance to reach equilibrium before the next pulse arrives. From another perspective, a photocurrent measurement can be interpreted as the impulse response of the THz array system. Since all other parameters including fabrication, metallization, annealing, and optical excitation conditions remain the same, the impulse response of the increased number of array is consistent with the increased capacitive behavior. Again, the amplitude discrepancy is a result of insufficient field recovery before the next impulse arrives.

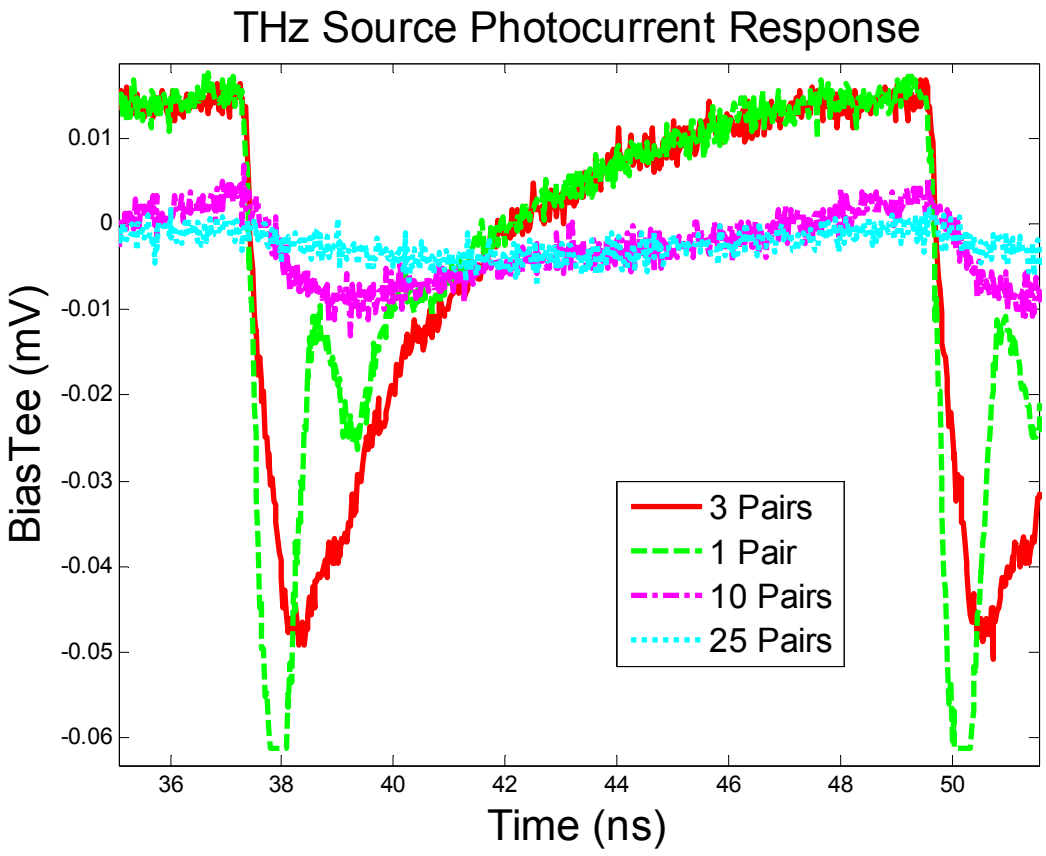

Figure 57 Photocurrent observed by a 5 mW point excitation: 1, 3, 10 and 25 pair of THz array pairs

It is possible that the interdigitated format of the THz array can change the carrier dynamics of TEF that causes weakening of TEF enhancement. In fact, this weakening could be due to both the geometry of array and the capacitance. Nonetheless, the capacitance factor seems to be consistent with THz array behavior.

7.3.3. THz Line Excitation Array Limitation

There are two factors in array limitation to consider. The first factor is a typical linear array limitation of distance between the elements and the number of array elements from the array factor. The second and the more difficult limitation is TEF field dynamics. If it is indeed the capacitance that limits TEF weakening, improving the array design can

effectively reduce the overall capacitance by inducing insulating region under the metal, such as pads, or reducing the width of the electrode. Also, the development of an ultrafast laser with a slower repetition of the pulse would allow larger field regeneration time.

7.3.4. Conclusion

The THz PC array has experimentally demonstrated power scaling with respect to the number of array elements. Numerical analysis including a Gaussian profile of the beam intensity demonstrates the expected quadratic behavior with a number of array elements. The THz array sources of both 40 μm and 90 μm geometries exhibited significantly weaker field even though it retained the anode field enhancement as expected in the TEF. THz radiation from the interferometric analysis shows THz emission is completed within the first two picoseconds of the optical excitation. Therefore, the capacitance of the system does not play a role in the THz radiation process. The increased capacitance appears to have an inverse relationship to weaker TEF. An alternate array design with reduced capacitance or a reduced pulse repetition is necessary to confirm this hypothesis.

CHAPTER 8: Conclusion and Suggested Future Works

THz photoconductive sources provide convenient room-temperature operation, simple geometry, and a broadband spectrum. They are not meant to compete against narrow band sources such as quantum cascade lasers. Besides, even with recent successes in reaching high operating powers, the low temperature operation issues of quantum cascade lasers are a difficult problem to solve in near future. However, the low efficiency of the THz photoconductive source is also a problem.

This document mainly discusses the trap-enhanced field effect and its field enhancement advantage in high efficiency THz power generation, as well as a spatially extended optical excitation. The optical-THz efficiency does not tell the whole story in most cases. The efficiency often neglects the system complexity involved in reaching the efficiency number. In practice, it is often system peripherals that require the most energy to operate, limiting the practical usefulness of real THz systems, even if the THz source itself has a high efficiency. Another important advantage of the TEF THz PC source is its compact structure and reasonably low bias voltage, which eliminates the need for a high voltage source.

The line excitation demonstrates an order of magnitude improvement in power by significantly reducing the space-charge screening without adding complexity. The THz efficiency quoted, ~0.01%, is the highest efficiency yet reported in THz PC sources. HDM analysis identifies the screening-effect influence on the TEF THz source. In

addition, the scalability of the line excitation is demonstrated. The power improvement is achieved without sacrificing any spectrum. In fact, the spectral analysis of the line excitation demonstrates extended low frequency content compared to that of the point excitation.

Regarding the THz line excitation array, it is disappointing to learn that its performance did not meet the expected power level. The overall weakening of the TEF is an unexpected result. The experimental data seem to point to the capacitance of the THz array design as the source of the problem. If the lower power is indeed due to elevated capacitance, there are several potential solutions to lower the capacitance, such as a two-step fabrication process to grow an insulating layer underneath the metal pads, or a narrower electrode metal width. A higher peak power and lower repetition rate laser can also address this problem. On the other hand, it is also possible that the interdigitated form of the array could interfere with the field enhancement dynamics. Future work should include both capacitance measurements at high bias and an investigation of the carrier dynamics of TEF in array form.

Related Publications

J. H. Kim, A. Polley, S. E. Ralph, “High efficiency terahertz photoconductive sources by use of spatially shaped excitation”, Lasers and Electro-Optics Society (IEEE-LEOS 2004, Puerto Rico), November 2004

A. Polley, J. H. Kim, S. E. Ralph, “Efficient photoconductive THz source with spatially shaped excitation”, Conference on Lasers and Electro-Optics/Quantum Electronics and Laser Science (CLEO/QELS 2005, Baltimore MD), May 2005

J. H. Kim, A. Polley, S. E. Ralph, "Efficient photoconductive terahertz source using line excitation," Opt. Lett. **30**, 2490-2492 (2005)

J. H. Kim, S. E. Ralph, “Enhanced low frequency content of THz source with line source excitation,” Lasers and Electro-Optics Society (IEEE-LEOS 2006, Montreal QB), November 2006, Oral Presentation.

J. H. Kim, D. Dennison, M. Knotts, S. E. Ralph, “Scalability of Line Excitation THz Arrays”, Conference on Lasers and Electro-Optics/Quantum Electronics and Laser Science (CLEO/QELS 2007, Baltimore MD), May 2007, Poster Presentation.

Appendix I: Fabrication Process

The fabrication process has only one mask level. A dark-field mask is used. The fabrication process has been developed, and the details given here, for a sample size that is one quarter of a 4" wafer. This process flow assumes that the user is familiar with the following equipment and general procedures. The equipments stated in this document is from the Georia Tech MiRC cleanroom.

1.1 Equipment:
CEE Model 100CB Spinner/Hotplate
Karl Suss MJB-3 Mask Aligner
CVC E-Beam Evaporator

2.1 Photolithography

2.1.1 Remove sample from wafer box.
2.1.1.1 Recall: 'Good' side is face down in wafer box.
2.1.1.2 Solvent clean is not performed.
2.1.2 Pre-heat the CEE spinner hotplate to 110 °C.
2.1.2.1 110 °C is a MiRC cleanroom reference.
2.1.2.2 Hotplate uniformity is ±0.30% (quoted by MiRC cleanroom).
2.1.3 Center wafer directly on CEE spinner chuck.
2.1.3.1 The 1" diameter chuck works best for the quartered sample.
2.1.4 Program the appropriate spin speeds.
2.1.4.1 Spread: 1000 rpm, 1000 rpm/sec, 5 sec
2.1.4.2 Spin: 4000 rpm, 1000 rpm/sec, 30 sec
2.1.5 Test the wafer centering.
2.1.5.1 Very slight 'wobble' is acceptable and will not affect the photoresist spread/spin (in other words, a *perfectly* centered wafer is not essential).
2.1.6 After wafer is properly centered on the spinner chuck, blow the sample clean with N_2.
2.1.7 Apply Shipley 1827 photoresist to wafer.
2.1.8 Run the spinner program.
2.1.9 Pre-bake wafer on hotplate at 110 °C for 60 sec.
2.1.9.1 Cool wafer on heat sink for 30 sec.
2.1.10 Measure the UV intensity of the right MJB-3 mask aligner at 405 nm.
2.1.10.1 Although Shipley 1827 positive photoresist is optimized for g-line exposure (436 nm), we use the h-line detector (405 nm) when measuring the power.
2.1.10.2 Typical UV intensity range: 2.5 mW/cm^3 – 6.0 mW/cm^3 (MiRC).

2.1.10.3 Mask specifications:
- Quartz/Chrome
- 4" x 4"
- 1.5 mm thick
- Mask material (quartz grade) shows good performance at h-line exposure.

2.1.11 Set appropriate exposure time for 165 mJ/cm^3 exposure energy.
2.1.11.1 Use the *Constant Intensity 1 (CI1)* option on the MJB-3 mask aligner.
2.1.11.2 Exposure time is found by dividing the desired exposure energy (165 mJ/cm^3) by the measured UV intensity (in mW/cm^3).
2.1.12 THz source mask should be solvent cleaned (TCE, acetone, methanol, isopropanol, DI water, N_2 blow dry) prior to using.
2.1.12.1 Inspect the mask each time for scratches or blemishes.
2.1.13 Align wafer with mask pattern.
2.1.13.1 THz source edge should be parallel to wafer cleave edge(<110> plane).
2.1.13.2 Make contact between mask and wafer.
2.1.14 Begin exposure. Do not look at the UV light!
2.1.15 When exposure is complete, remove wafer from chuck.
2.1.16 Develop in undiluted Shipley 354 developer for 35 – 40 sec using a constant swirling motion.
2.1.17 Rinse thoroughly under DI water faucet for at least 20 sec to stop the developing process.
2.1.18 N_2 blow dry.
2.1.19 Inspect with a high magnification microscope using yellow light (filter) for clearly defined edges and a thoroughly developed pattern.
2.1.19.1 If development is not complete, repeat steps 2.1.16-2.1.19 until it is finished.
2.1.20 Measure the thickness of the Shipley 1827 photoresist with a surface profiler.
2.1.20.1 Necessary only occasionally to verify that the photoresist thickness is consistent with the spin speed, bake time, and viscosity.
2.1.20.2 Typical Shipley 1827 photoresist thicknesses: 1.5 μm – 2.5 μm.

2.2 Metallization
2.2.1 Securely attach the sample to the appropriate e-beam evaporator chuck.
2.2.2 Vent the electron-beam evaporator chamber.

2.2.3 Load the sample.

2.2.3.1 Follow the proper procedures for the e-beam, which are outlined on the MiRC cleanroom webpage.

2.2.4 Pump down the e-beam chamber.

2.2.4.1 Let the system pump to a base pressure of ~1.0 x 10^{-6} Torr.

- Pump down takes ~30 minutes.
- Can pump to a lower pressure if desired.

2.2.5 Program the metal thicknesses according to the GTRI recipe.

2.2.5.1 IBM Recipe (used in the past fabrication process)

- GaAs substrate
- 50 Å Ni
- 100 Å Ge
- 800 Å Au
- 100 Å Ge
- 300 Å Ni
- 1000 Å Au

2.2.5.2 GTRI Recipe

- GaAs substrate
- 800 Å AuGe (88-12)
- 300 Å Ni
- 1000 Å Au

2.2.6 Follow appropriate procedure for evaporating metals and record all values from the front panel (pressure, current, voltage, power, evaporation rate, etc.).

2.2.6.1 A good evaporation rate is 1 Å/sec for Ni and Ge and 2 Å/sec for Au.

2.2.7 Allow 5 – 7 minutes for the chamber temperature to decrease.

2.2.8 Follow the e-beam power down procedure.

2.2.9 Vent the chamber.

2.2.10 Unload the sample and remove from the chuck.

2.2.11 Follow pump down procedure for the e-beam evaporator.

2.3 Metal Lift off

2.3.1 Prepare an acetone bath large enough to completely immerse the sample.

2.3.2 Soak the sample in the acetone.

2.3.2.1 Lift off time is as much as one hour, but usually less.

2.3.2.2 A light swirling motion somewhat decreases the lift off time.

2.3.2.3 In the case of a very difficult lift off, the ultra-sonic bath can be used for 1 – 2 minutes maximum. Normally, less than 1 minute is sufficient.

– If ultra-sonic bath is needed, sample must still be in an acetone bath.

2.3.3 Inspect the sample with a microscope to ensure that lift off is complete.

3.1 Mask Layout:

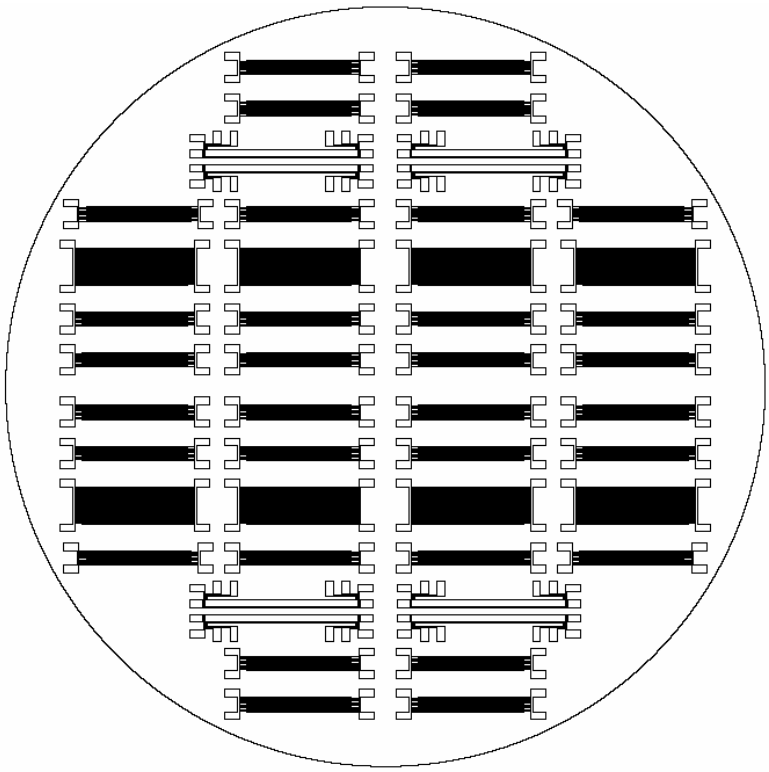

4.1 Array Layout:

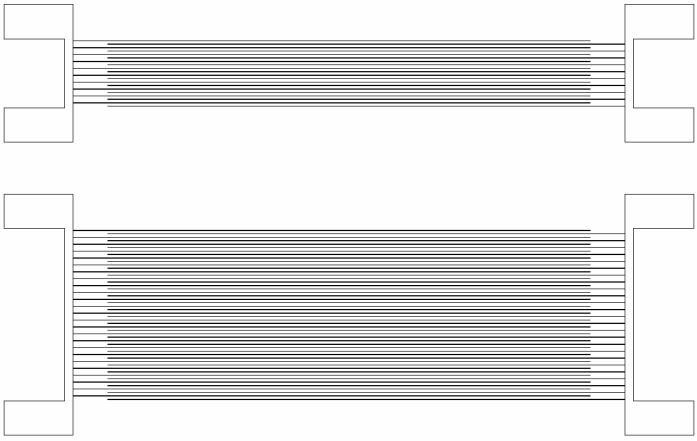

Appendix II: Hydrodynamic Model

The following information detailed description of the hydrodynamic model that is used to compare the point and line excitation total radiated power and efficiency. The contribution is primarily is done by Arup Polley.

It is well known that radiated electric fields are produced by time varying currents. Indeed, Terahertz signals are generated from transient photocurrents produced by femtosecond pulses. Method to assess the radiation necessarily begin with the Larmor result which describes the power radiated from an accelerated charge:

Thus, we wish to describe the time evolution of the current when a semiconductor is illuminated with ultra-short (<100fs) light pulses and determine the ensemble acceleration. It is anticipated that, due to the complex nature of the conduction band, the transient current waveform will not be determined solely by the temporal shape of the illuminating pulse. In fact the scattering mechanisms within the material play an important role in controlling the photocurrent dynamics and hence the radiated THz waveform and power.

Here we outline the description of transient photocurrents in GaAs, without including spatial effects. However, the results can be equally applied to other semiconductors, provided that the relevant transport parameters are available and the results can be generalized to be including within the framework of a completely self-consistent three dimensional solution.

There are generally three methods of solution to determine transient photocurrents in complex semiconductors:

1. Monte-Carlo: following thousands of individual particles to produce statistically relevant observable.
2. Direct solution of the Boltzmann Transport Equation (B.T.E) involves many simplifications to be manageable.
3. Moment balance method: reduce the B.T.E to three conservation (balance) equations, by the integration over all momentum space.

The moment balance equations require accurate descriptions of relaxation (scattering) rates in order to be useful. It has been shown (Shur 1976) (Carez et al 1980) that by using a Monte-Carlo procedure to calculate the scattering rates, the Moment balance method, which is orders of magnitude faster, can be accurate as well.

Moment balance equations and hydrodynamic model

Balance equations are used to analyze the semi-classical carrier transport by following the spatial and temporal variations of the particle, momentum and energy densities. Balance equations are derived from the Boltzman transport equation by integrating in momentum space first and then truncating higher order terms. For the scattering rates required in balance equations, the ensemble relaxation rates are employed. The Monte Carlo method is used to determine the ensemble relaxation rates.

To characterize the state of carriers in a valley three parameters are used: carrier density (n), velocity (**v**), and energy. The energy is subdivided into two parts: kinetic energy (energy due to drift velocity) and thermal energy (energy due to random career movement).

The scattering equations for three-band hydrodynamic model:

Particle scattering rates

$$\frac{dn_\Gamma}{dt} = -n_\Gamma\left(\frac{1}{\tau_{n\Gamma L}(\varepsilon_\Gamma)} + \frac{1}{\tau_{n\Gamma X}(\varepsilon_\Gamma)}\right) + \frac{n_L}{\tau_{nL\Gamma}(\varepsilon_L)} + \frac{n_X}{\tau_{nX\Gamma}(\varepsilon_X)}$$

$$\frac{dn_L}{dt} = -n_L\left(\frac{1}{\tau_{nL\Gamma}(\varepsilon_L)} + \frac{1}{\tau_{nLX}(\varepsilon_L)}\right) + \frac{n_\Gamma}{\tau_{n\Gamma L}(\varepsilon_\Gamma)} + \frac{n_X}{\tau_{nXL}(\varepsilon_X)}$$

$$\frac{dn_X}{dt} = -n_X\left(\frac{1}{\tau_{nX\Gamma}(\varepsilon_X)} + \frac{1}{\tau_{nXL}(\varepsilon_X)}\right) + \frac{n_L}{\tau_{nL\Gamma}(\varepsilon_L)} + \frac{n_X}{\tau_{nX\Gamma}(\varepsilon_X)}$$

momentum (velocity) scattering rates

$$\frac{dv_\Gamma}{dt} = -v_\Gamma\left(\frac{1}{\tau_{p\Gamma\Gamma}(\varepsilon_\Gamma)} + \frac{1}{\tau_{p\Gamma L}(\varepsilon_\Gamma)} + \frac{1}{\tau_{p\Gamma X}(\varepsilon_\Gamma)} + \frac{1}{n_\Gamma}\frac{dn_\Gamma}{dt}\right) + \frac{qF}{m^*_\Gamma(\varepsilon_\Gamma)}$$

$$\frac{dv_L}{dt} = -v_L\left(\frac{1}{\tau_{pLL}(\varepsilon_L)} + \frac{1}{\tau_{pL\Gamma}(\varepsilon_L)} + \frac{1}{\tau_{pLX}(\varepsilon_L)} + \frac{1}{n_L}\frac{dn_L}{dt}\right) + \frac{qF}{m^*_L(\varepsilon_L)}$$

$$\frac{dv_X}{dt} = -v_X\left(\frac{1}{\tau_{pXX}(\varepsilon_X)} + \frac{1}{\tau_{pX\Gamma}(\varepsilon_X)} + \frac{1}{\tau_{pXL}(\varepsilon_X)} + \frac{1}{n_X}\frac{dn_X}{dt}\right) + \frac{qF}{m^*_X(\varepsilon_X)}$$

Energy scattering rates

$$\frac{dw_\Gamma}{dt} = qv_\Gamma F - \frac{(w_\Gamma - E_0)}{\tau_{w\Gamma\Gamma}(\varepsilon_\Gamma)} - w_\Gamma\left(\frac{1}{\tau_{w\Gamma L}(\varepsilon_\Gamma)} + \frac{1}{\tau_{w\Gamma X}(\varepsilon_\Gamma)} + \frac{1}{n_\Gamma}\frac{dn_\Gamma}{dt}\right) + \frac{n_L}{n_\Gamma}\frac{\varepsilon_L}{\tau_{\varepsilon L\Gamma}(\varepsilon_L)} + \frac{n_X}{n_\Gamma}\frac{\varepsilon_X}{\tau_{\varepsilon X\Gamma}(\varepsilon_X)}$$

$$\frac{dw_L}{dt} = qv_L F - \frac{(w_L - E_0)}{\tau_{wLL}(\varepsilon_L)} - w_L\left(\frac{1}{\tau_{wL\Gamma}(\varepsilon_L)} + \frac{1}{\tau_{wLX}(\varepsilon_L)} + \frac{1}{n_L}\frac{dn_L}{dt}\right) + \frac{n_\Gamma}{n_L}\frac{\varepsilon_\Gamma}{\tau_{\varepsilon\Gamma L}(\varepsilon_\Gamma)} + \frac{n_X}{n_L}\frac{\varepsilon_X}{\tau_{\varepsilon XL}(\varepsilon_X)}$$

$$\frac{dw_X}{dt} = qv_X F - \frac{(w_X - E_0)}{\tau_{wXX}(\varepsilon_X)} - w_X\left(\frac{1}{\tau_{wX\Gamma}(\varepsilon_X)} + \frac{1}{\tau_{wX\Gamma}(\varepsilon_X)} + \frac{1}{n_X}\frac{dn_X}{dt}\right) + \frac{n_\Gamma}{n_X}\frac{\varepsilon_\Gamma}{\tau_{\varepsilon\Gamma X}(\varepsilon_\Gamma)} + \frac{n_L}{n_X}\frac{\varepsilon_L}{\tau_{\varepsilon LX}(\varepsilon_L)}$$

Here

n = Number density of carriers,

V = Ensemble velocity,

W/ε = Average energy,

$\tau_{wX\Gamma}$ = Energy scattering time from X band to Γ band,

F = Electric field strength,

E_0 = Equlibrium energy for the corresponding band,

q = Charge of an electron,

m^* = Effective mass.

In the hydrodynamic model three types of scattering times are used.

1. $\tau_{nX\Gamma}(\varepsilon)$ is the relaxation time for scattering of carriers with ensemble energy (total) ε from X band to Γ band. Similar relaxation times are used to find the change in the carrier density due to scattering.

2. $\tau_{pX\Gamma}(\varepsilon)$ is the momentum relaxation time for intervalley scattering from X band to Γ band. $\tau_{pXX}(\varepsilon)$ is for the intravalley momentum scattering in X band.

$$\text{Eg.}\ \frac{dv_\Gamma}{dt} = -v_\Gamma\left(\frac{1}{\tau_{p\Gamma\Gamma}(\varepsilon_\Gamma)} + \frac{1}{\tau_{p\Gamma L}(\varepsilon_\Gamma)} + \frac{1}{\tau_{p\Gamma X}(\varepsilon_\Gamma)} + \frac{1}{n_\Gamma}\frac{dn_\Gamma}{dt}\right) + \frac{qF}{m^*_\Gamma(\varepsilon_\Gamma)}$$

The negative sign in the first bracketed term implies that the loss of momentum in collision is directed opposite the average velocity, which again means that we assume full isotropy. Furthermore, we assume that the intervalley scattering completely randomizes momentum, hence there is no net momentum transferred from one valley to the other.

3. $\tau_{wX\Gamma}(\varepsilon)$ is the ensemble energy relaxation time for intervalley scattering from X to Γ. $\tau_{wX\Gamma}(\varepsilon)$ is associated with a negative sign in the equation, so it denotes the energy lost from X valley due to scattering from X to Γ valley. $\tau_{wLL}(\varepsilon_L)$ describes the relaxation towards the lattice temperature T_0 in intervalley scattering.

$\tau_{e\Gamma X}(\varepsilon_\Gamma)$ is also energy scattering time. It describes the rate of energy supplied by Γ valley to X valley. Note that $\tau_{e\Gamma X}(\varepsilon_\Gamma)$ and $\tau_{w\Gamma X}(\varepsilon_\Gamma)$ are different i.e. the energy lost in Γ is different from the energy gained by X. This is due to the energy exchange with phonons and due to the difference Δ in the references for the kinetic energy of the two valleys.

Eg.

$$\frac{dw_\Gamma}{dt} = qv_\Gamma F - \frac{(w_\Gamma - E_0)}{\tau_{w\Gamma\Gamma}(\varepsilon_\Gamma)} - w_\Gamma\left(\frac{1}{\tau_{w\Gamma L}(\varepsilon_\Gamma)} + \frac{1}{\tau_{w\Gamma X}(\varepsilon_\Gamma)} + \frac{1}{n_\Gamma}\frac{dn_\Gamma}{dt}\right) + \frac{n_L}{n_\Gamma}\frac{\varepsilon_L}{\tau_{\varepsilon L\Gamma}(\varepsilon_L)} + \frac{n_X}{n_\Gamma}\frac{\varepsilon_X}{\tau_{\varepsilon X\Gamma}(\varepsilon_X)}$$

$$\frac{dw_X}{dt} = qv_X F - \frac{(w_X - E_0)}{\tau_{wXX}(\varepsilon_X)} - w_X\left(\frac{1}{\tau_{wX\Gamma}(\varepsilon_X)} + \frac{1}{\tau_{wX\Gamma}(\varepsilon_X)} + \frac{1}{n_X}\frac{dn_X}{dt}\right) + \frac{n_\Gamma}{n_X}\frac{\varepsilon_\Gamma}{\tau_{\varepsilon\Gamma X}(\varepsilon_\Gamma)} + \frac{n_L}{n_X}\frac{\varepsilon_L}{\tau_{\varepsilon LX}(\varepsilon_L)}$$

Comparison of the scattering rates used in Monte Carlo simulation and hydrodynamic model

Carrier scattering rates used in the hydrodynamic model show a close match with the scattering rates used in Monte Carlo method.

Scattering rates used in the Monte Carlo method has a sharp turn on and these turn on energy indicate the difference in the reference energy levels of the valleys. For

e.g. ΔE between L and Γ is approximately 300 meV and the scattering rate from Γ to L increases sharply at around 300 meV. Similarly Γ to X scattering show a sharp turn on at ~500 meV as the energy gap between those two valleys is 500 meV.

The scattering rates used in the hydrodynamic model have a softer turn on compared to those used in Monte Carlo method. This broadening can be attributed to the fact that they are mean scattering rates as a function of mean energy of an ensemble of electrons.

1. **Scattering rates for gamma band**

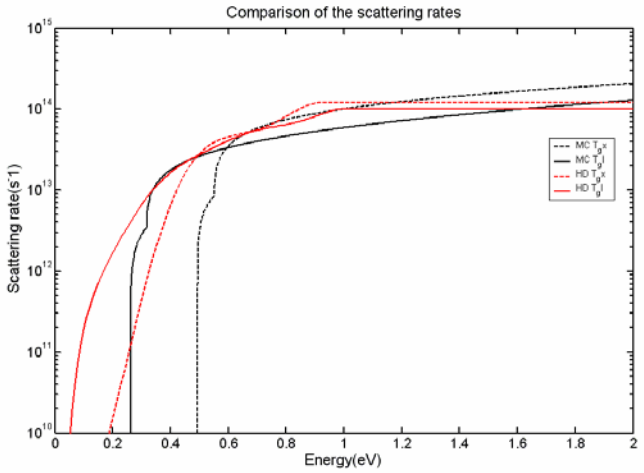

2. **Scattering rates for L band**

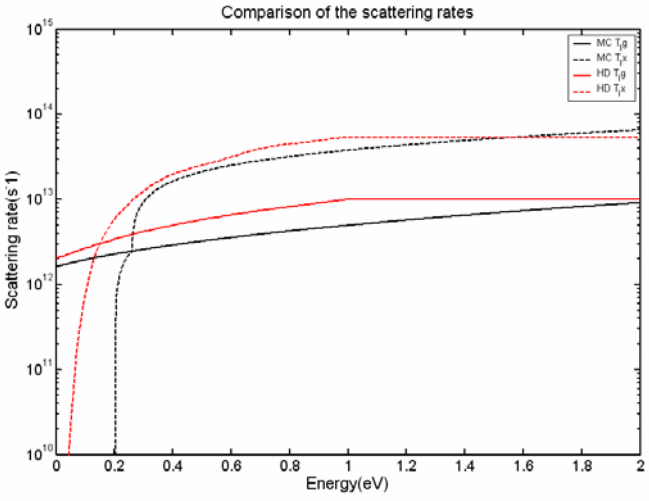

3. **Scattering rates for X band**

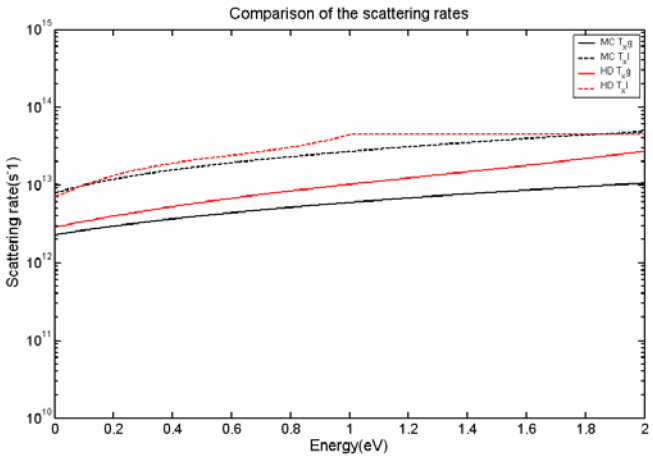

Hydrodynamic Results:

1. Comparison of drift velocity:

We compare the Moment balance method with Monte-Carlo for a particular stressful situation, namely less than 100 femtosecond illumination in the presence of a 40 kV/cm field. In this regime the carrier dynamics are highly nonlinear and scattering from and to both X and L band occurs quickly. We simulate this by using initial conditions of 96 meV excess energy and a field step of 40 kV/cm at t=0. The drift velocity of the electron ensemble as calculated in the moment balance method matches closely with the results of the Monte-Carlo method. We note that there are no adjustable parameters.

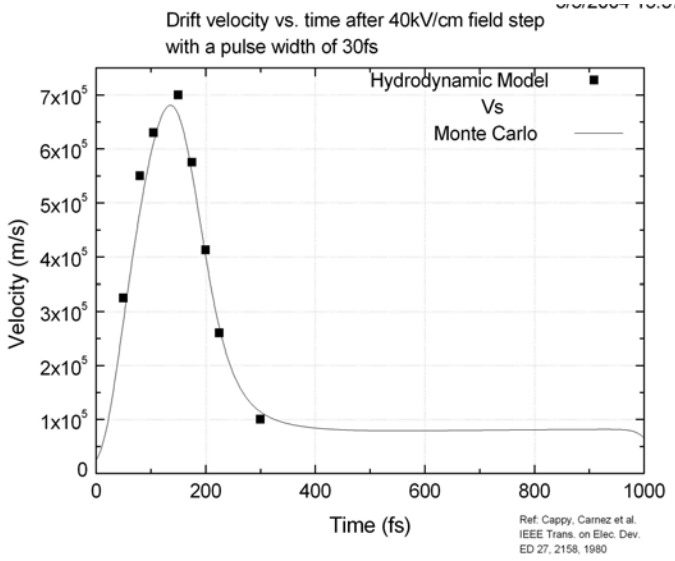

2. Field strength dependence of drift velocity

Drift velocity is a function of applied field strength. Acceleration and peak velocity are more of higher field strength as expected.

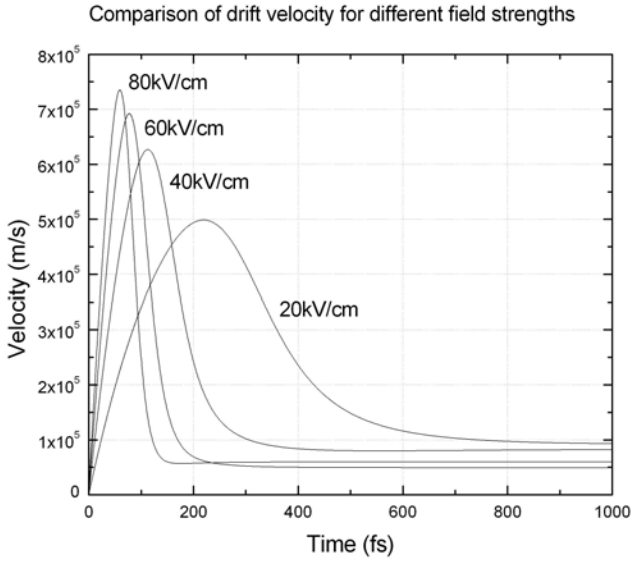

3. Wavelength dependence of drift velocity overshoot

Drift velocity also depends on the initial energy of the electrons in the gamma band. A higher initial energy implies a larger initial effective mass and a commensurately lower acceleration. Therefore, the drift velocity overshoot is larger for lower initial energies. This suggests a wavelength dependence effect.

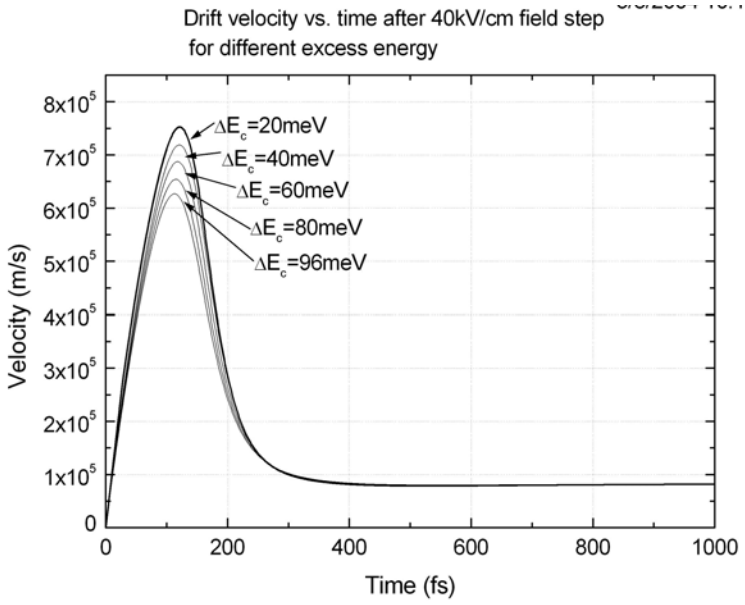
Drift velocity vs. time after 40kV/cm field step
for different excess energy
Velocity (m/s)
Time (fs)
ΔE_c=20meV
ΔE_c=40meV
ΔE_c=60meV
ΔE_c=80meV
ΔE_c=96meV
0
1x10^5
2x10^5
3x10^5
4x10^5
5x10^5
6x10^5
7x10^5
8x10^5
0
200
400
600
800
1000

4. TeraHertz power

TeraHertz power increases in a quadratic manner with increasing optical power.

Power is calculated using the Larmor's formula.

Larmor's formula for calculating power radiated of an accelerated charged particle:

$$P = \frac{1}{6\pi\varepsilon_0}\frac{n^2 q^2 a^2}{c^3}$$

From Larmor result we see,

- Power ∝ square of acceleration
- Power ∝ square of number of charge particles
- Power is independent of material permittivity

The assumptions of Larmor's result are,

- Point charge
- Applies to ensembles only when the electric fields produced at a distance by all point charges add in phase and that requirement is fulfilled if the ensemble spread is much smaller than the wavelength of interest. A frequency of 2 THz corresponds to 1500μm which is much greater than spot radius of 4μm.

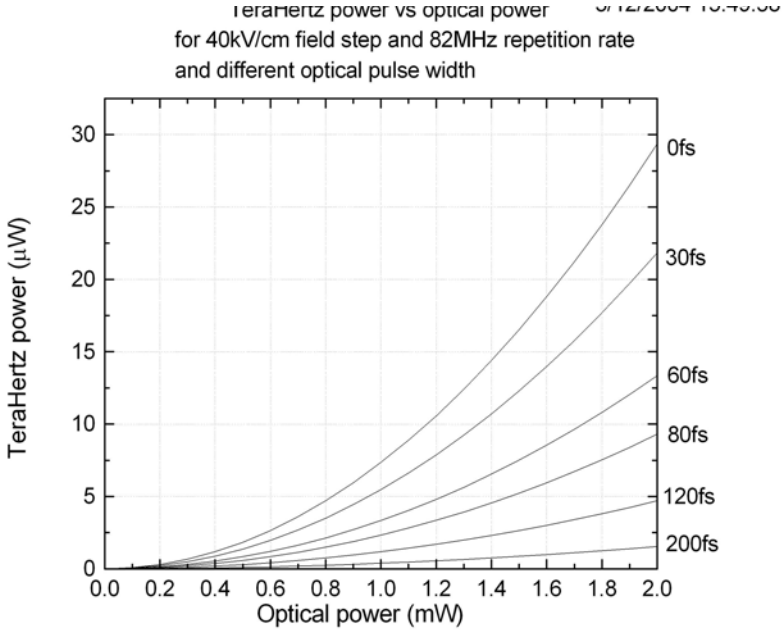

Terahertz power generated depends on the optical pulse width. Shorter pulses produce more power.

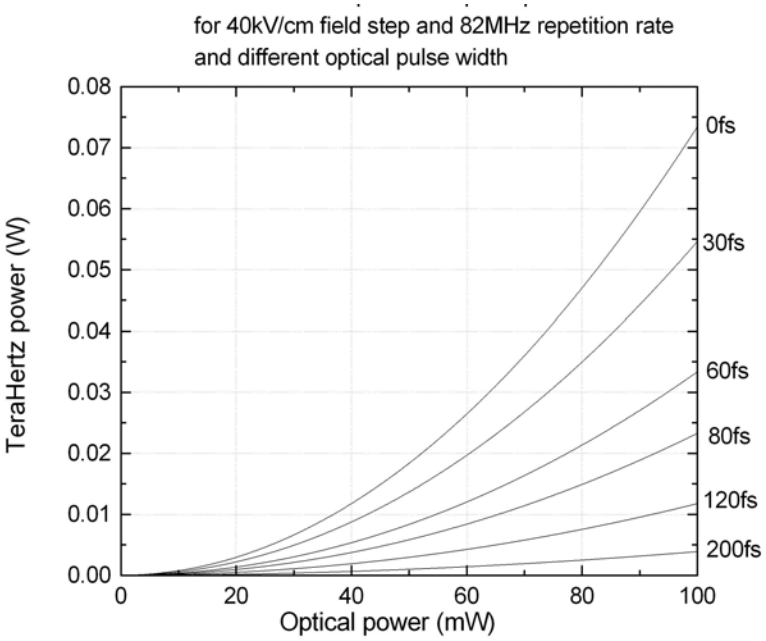

TeraHertz power has been plotted as a function of pulse width for different fixed average optical power.

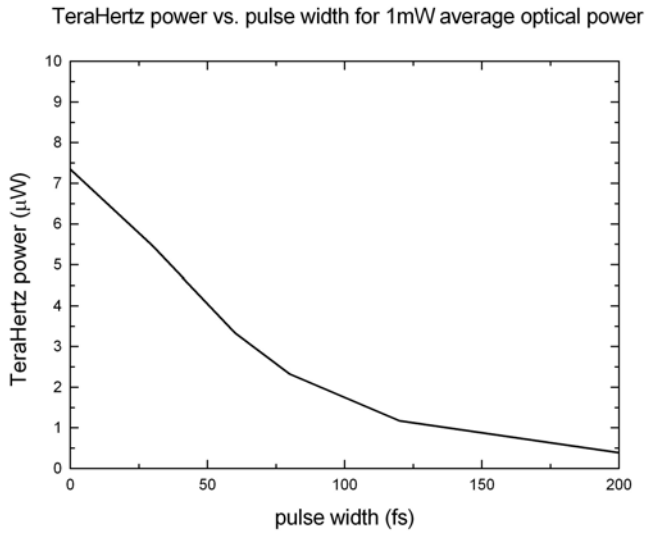

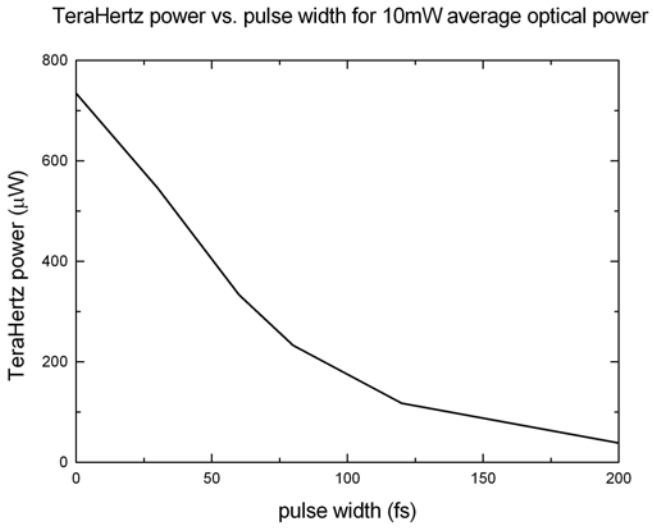

5. Screening effect of space charge

As the electrons drift (hole drift is negligible), the separated electron and holes produce space charge electric field, which screens the applied electric field and hence reduces its effect.

Screening electric field is calculated assuming that it does not affect the drift velocity of the electrons i.e. this is not a self-consistent calculation. However, it is a good measure of the onset of screening effect.

The following screening field strengths are calculated for a spot radius of 4μm. Screening field generated becomes comparable to the applied bias field with increasing optical power. This may explain the observed saturation of the TeraHertz power generation at higher optical power.

Screening field scales linearly with space charge density. For e.g. a line source of 100μm x 5μm has $1/20^{th}$ the carrier density i.e. $1/20^{th}$ the effective optical power or equivalently, a line source of 100μm x 5μm can have 20 times more power and suffer similar screening effect as 5μm x 5μm spot.

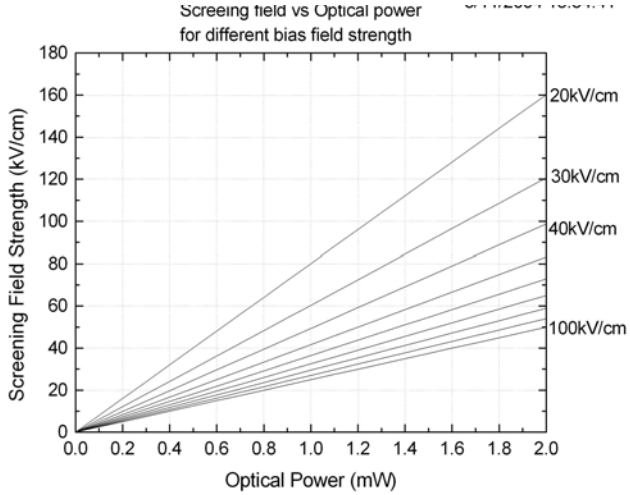

6. Case study: 80fs optical pulse

For optical pulse width of 80fs drift velocity, acceleration, instantaneous THz power and THz power spectral density are plotted.

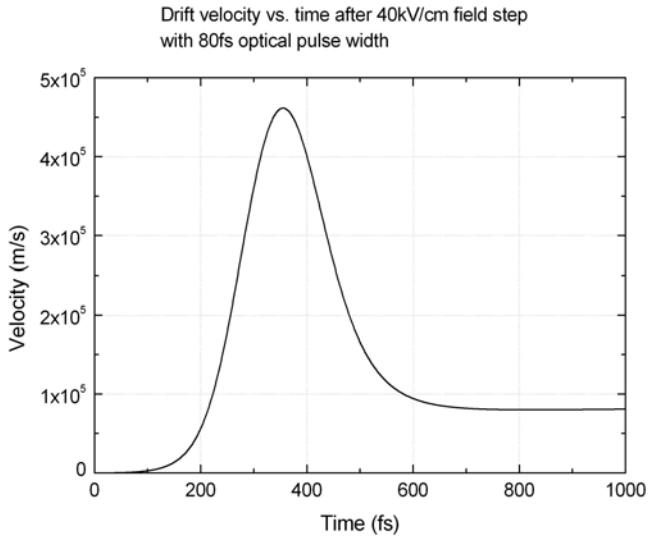

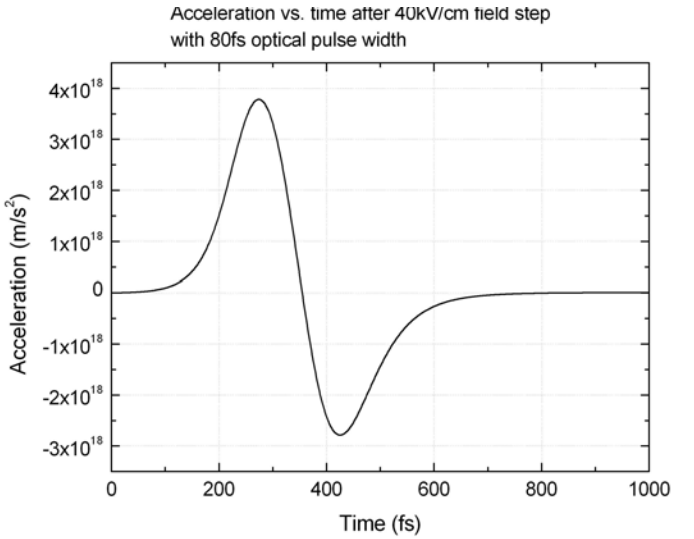

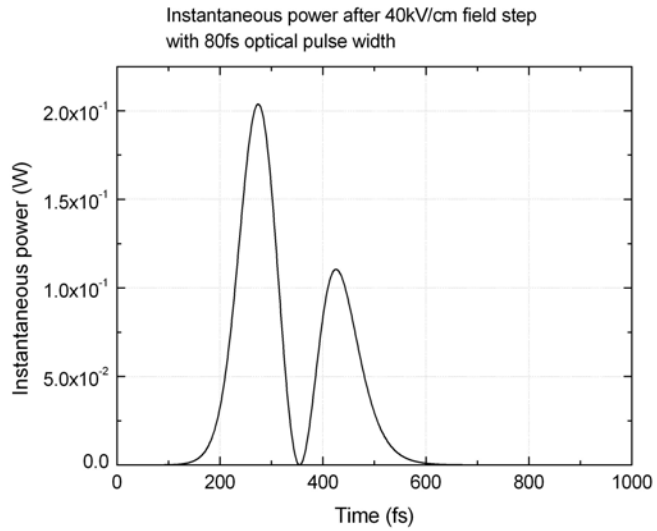

7. Power spectral density

Power spectral density of TeraHertz signal shows that short pulses generates higher power at all frequencies. But relative high frequency content for short pulses is more.

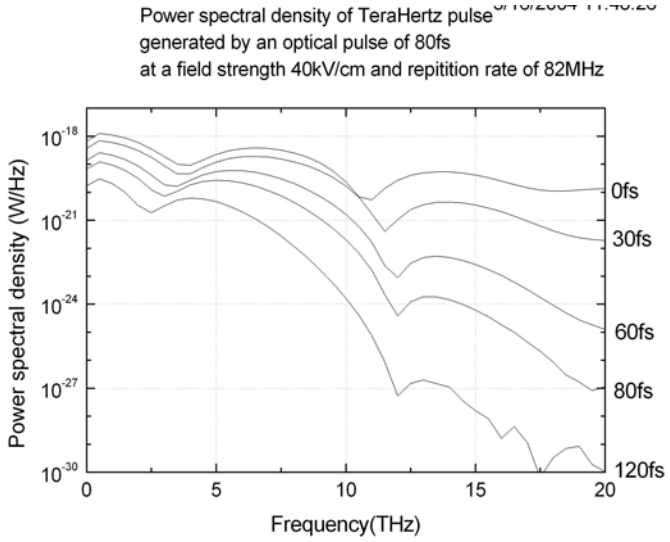

8. Steady state mobility as found from the Hydrodynamic simulation

Steady state drift velocity for the carriers is found for different bias field. It shows a characteristic velocity overshoot.

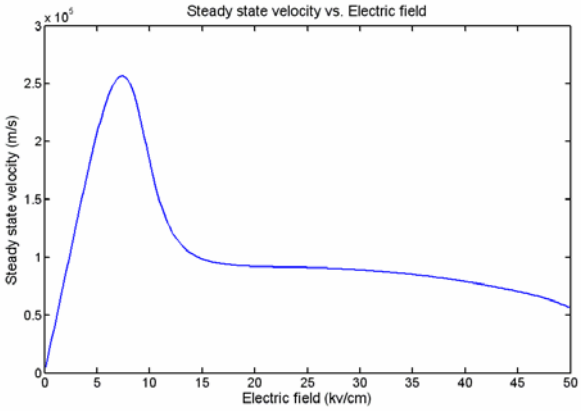

Steady state mobility = (Steady state velocity at a particular field) / (Electric field)

Steady state mobility for low field is around 4 k cm^2/V-s, which is consistent with the mobility of semi-insulating doped GaAs.

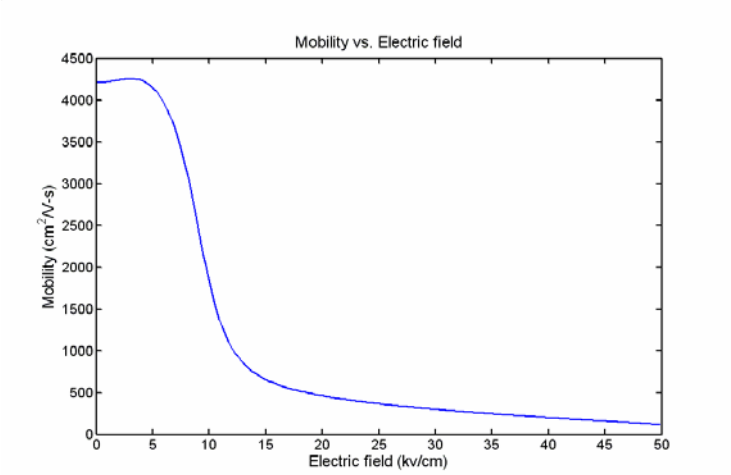

Multi-subband hydrodynamic model

The previous results do not include any spatial dependence of the photocurrents. Yet an accurate depiction of the interaction of these photocurrent and an antenna structure explicitly requires the spatial dependence of the electromagnetic fields. We wish to incorporate these results within a finite difference time domain (FDTD) analysis of the carrier dynamics interacting with the electrode and antenna structure.

Within an FTDT analysis, the combination of distinct grid points together with distinct carrier distributions coupling in and out of each grid point requires the inclusion of complex carrier distributions which cannot be modeled as a single ensemble average. Thus we must generalize the hydrodynamic model to allow for some fraction of carriers arriving from the neighboring grid points with different drift velocity and ensemble energy. The optical generation must also be allowed to vary across the grid. The assumption of Maxwellian distribution for the carriers may not be valid and the distribution may have significant structure To account for different distributions Gamma valley has been divided into several energy subbands. Withing each suband the model behaves as before and the sub-distribution is described by the ensemble averages of the hydrodynamic model. The carrier density, ensemble energy, and drift velocity of each band are updated separately in time step. The X and L valleys are not subdivided.

The results from multi-subband hydrodynamic model have been compared with the results from the 'standard' hydrodynamic model.

A few notes on the multi-subband hydrodynamic model

a. The Γ valley has been subdivided into 10 levels with 50 meV energy band (ΔE) for each. An electron enseble with a particular average energy resides in appropriate energy sublevel.

b. Electrons from one level can go to another level depending on the average energy of the carriers in that level. The drift velocity and carrier density of the levels are adjusted accordingly in the process of transition.

c. Electrons from all levels in the Γ valley can scatter to the L and X valley.

d. Electrons scattered from L and X valley finds a place in the highest energy level in the Γ valley.

e. <u>The energy scattering from L and X valley increases the average energy of electrons of all sublevels in Γ valley</u>.

Comparison of Multi-subband with standard Hydrodynamic model

Since THz power is proportional to the square of acceleration multiplied by the number of electrons present in the system, therefore n(t)$\mathbf{V_d}$(t) is of more interest than $\mathbf{V_d}$(t) alone.

Suppose,

$n(\varepsilon,t)$ = Carrier density in energy level ε at time t.

$V_d(\varepsilon,t)$ = Drift velocity of carriers with energy ε at time t.

We define $V(t) = \dfrac{\int_0^\infty V_d(\varepsilon,t)\,n(\varepsilon,t)\,d\varepsilon}{\int_0^\infty\int_0^\infty n(\varepsilon,\tau)\,d\varepsilon\,d\tau}$

$V(t)$ is normalized n(t)$\mathbf{V_d}$(t). In the next paragraph, we will call $V(t)$ by drift velocity.

Drift velocity for an impulse function is calculated from the standard hydrodynamic model. The impulse response is convolved with a hyperbolic secant pulse of full width at half maximum of 75 fs. In the multisubband hydrodynamic model same illumination is applied and drift velocity is calculated. The drift velocities calculated in two methods show striking similarity.

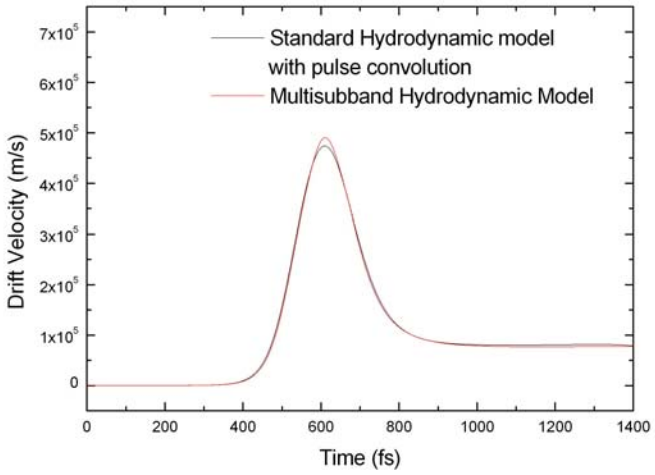

Multiple pulse illumination

The result of multiple pulse illumination has been determined using the multi-subband hydrodynamic model.

1. **Illumination**

The illumination is normalized with a pulse energy corresponding to 1mW average optical power at 82 MHz repetition rate.

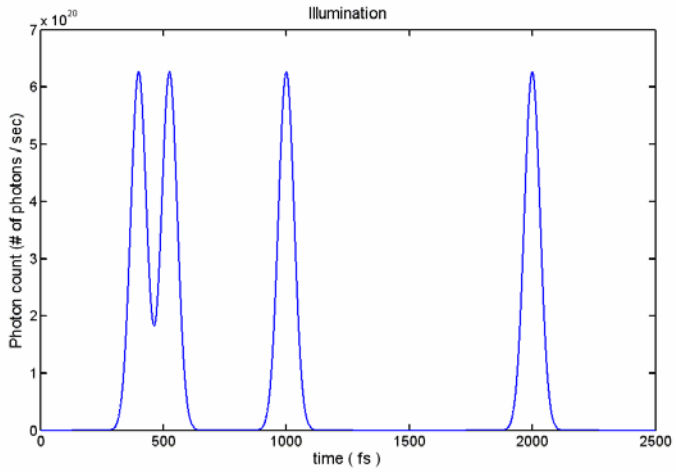

2. **Drift velocity**

Average velocity of the carriers present in the system at a particular time is plotted. The velocity peaks of the subsequent pulses go down because only the recent carriers contribute to overshoot.

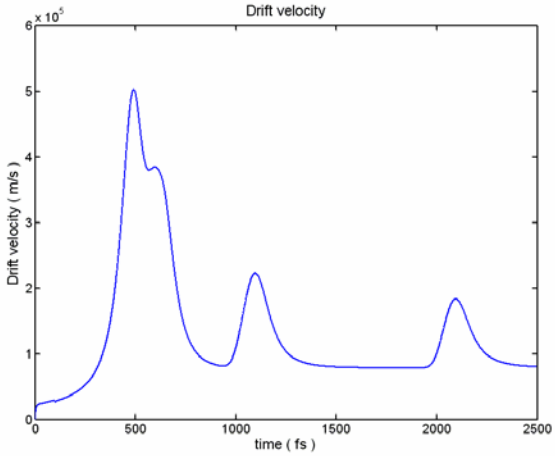

Drift velocity normalized to the carrier count in one pulse shows equal height velocity overshoots.

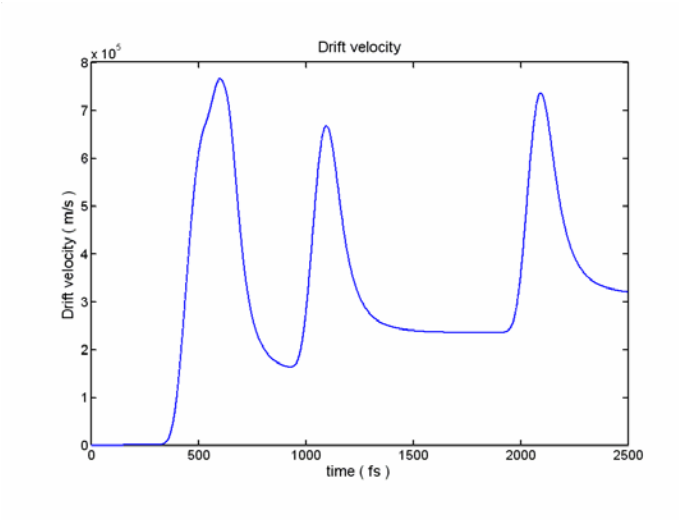

3. **Acceleration**

Acceleration is calculated from the second drift velocity. It shows that acceleration in case of the multiple illuminations is just the superposition of the accelerations produced by each of them. The peak and average terahertz power can be estimated from this acceleration data.

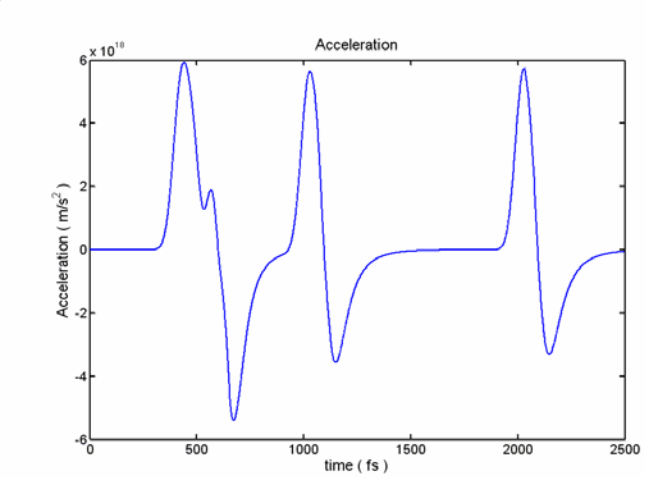

Appendix III: Interferometry from two separate sources

The following section is an insert from chapter 3 of a dissertation by Chen Yue describing method to retrieve a complex index from an interferometry using two separate sources.

Suppose the measured interferograms with and without samples are $I_s(x)$ and $I_o(x)$, where x is the relative delay of two THz sources. They are the convolutions of two sources and defined as

$$I_s(x) = \int_{-\infty}^{+\infty} E_1(x' - x, y', z') E_2^s(x', y', z') dx' dy' dz', \tag{3.1}$$

and

$$I_o(x) = \int_{-\infty}^{+\infty} E_1(x' - x, y', z') E_2^o(x', y', z') dx' dy' dz', \tag{3.2}$$

where $E_1(x, y, z)$ is the spatial envelop of the amplitude of the terahertz beam from source one, $E_2^o(x, y, z)$ and $E_2^s(x, y, z)$ the spatial envelops of the amplitude of the terahertz from source two without sample and with sample. The propagation direction of both beams is along the x-axis in the detection site. Since $E_1(x)$ and $E_2^o(x)$ are generated from two different GaAs chips, they are very similar but not identical. We want to prove that even though $E_1(x)$ and $E_2^o(x)$ are different, the general method of interferometry is still valid. Usually $E_2^s(x)$ is the transmitted signal of $E_2^o(x)$.

If the sample is uniform over the transmitted area, the integrations over y and z in $I_o(x)$ and $I_s(x)$ are the same. Thus the integration (3.1) and (3.2) can be written as

$$I_o(x) = A_o \int_{-\infty}^{\infty} E_1(x' - x) E_2^o(x') dx', \tag{3.3}$$

and

$$I_s(x) = A_o \int_{-\infty}^{\infty} E_1(x' - x) E_2^s(x') dx', \tag{3.4}$$

where A_o is a constant. The frequency spectra of $E_1(x)$, $E_2^o(x)$, and $E_2^s(x)$ are defined by Fourier transforms(FT):

$$E_1(\nu) = \int_{-\infty}^{\infty} E_1(x)\exp(i2\pi\nu x)dx = \rho_1(\nu)\exp(i\phi_1(\nu)), \tag{3.5}$$

$$E_2^o(\nu) = \int_{-\infty}^{\infty} E_2^o(x)\exp(i2\pi\nu x)dx = \rho_{2o}(\nu)\exp(i\phi_{2o}(\nu)), \tag{3.6}$$

and

$$E_2^s(\nu) = \int_{-\infty}^{\infty} E_2^5(x)\exp(i2\pi\nu x)dx = \rho_{2s}(\nu)\exp(i\phi_{2s}(\nu)). \tag{3.7}$$

The Fourier transforms $S(\nu)$ of the interferograms $I_o(x)$ and $I_s(x)$ are defined by

$$\begin{aligned} S_s(\nu) &= \int_{-\infty}^{\infty} I_s(x)\exp(i2\pi\nu x)dx = p_s(\nu) + iq_s(\nu) \\ &= \rho_s(\nu)\exp(i\phi_s(\nu)) \end{aligned}, \tag{3.8}$$

and

$$\begin{aligned} S_o(\nu) &= \int_{-\infty}^{\infty} I_o(x)\exp(i2\pi\nu x)dx = p_o(\nu) + iq_o(\nu) \\ &= \rho_o(\nu)\exp(i\phi_o(\nu)) \end{aligned}, \tag{3.9}$$

where ν is frequency in the unit of cm^{-1}, p and q are the real and imaginary parts of the Fourier transform. Assume the complex loss due to the present of the sample is

$$\tilde{L}(\nu) = L(\nu)\exp(i\phi_L(\nu)), \tag{3.10}$$

which is defined by

$$E_2^s(\nu) = \tilde{L}(\nu)E_2^o(\nu). \tag{3.11}$$

According to convolution theorem, we have

$$S_o(\nu) = E_1(\nu)E_2^o(\nu), \tag{3.12}$$

and

$$S_s(\nu) = E_1(\nu)E_2^s(\nu) = E_1(\nu)\tilde{L}(\nu)E_2^o(\nu). \tag{3.13}$$

From equations (3.8), (3.9), (3.12), and (3.13), we have

$$\rho_o(\nu) = \rho_1(\nu)\cdot\rho_{2o}(\nu), \tag{3.14}$$

$$\phi_o(\nu) = \phi_1(\nu) + \phi_{2o}(\nu), \tag{3.15}$$

$$\rho_s(\nu) = \rho_1(\nu)\cdot\rho_{2s}(\nu) = \rho_1(\nu)\rho_{2o}(\nu)L(\nu), \tag{3.16}$$

$$\phi_s(\nu) = \phi_1(\nu) + \phi_{2s}(\nu) = \phi_1(\nu) + \phi_{2o}(\nu) + \phi_L(\nu). \tag{3.17}$$

From equations (14) and (16), we have

$$L(\nu) = \frac{\rho_s(\nu)}{\rho_o(\nu)}, \tag{3.18}$$

$$\phi_L(\nu) = \phi_s(\nu) - \phi_o(\nu) = \tan^{-1}[\frac{q_s(\nu)}{p_s(\nu)}] - \tan^{-1}[\frac{q_o(\nu)}{p_o(\nu)}]. \tag{3.19}$$

Thus the complex loss $\widetilde{L}(\nu)$ of the sample can be calculated from the values of Fourier transforms of the measured interferograms. In the above definition, $\widetilde{L}(\nu)$ is the general loss which may be due to reflection, absorption, or any other scattering. The specific meaning of $\widetilde{L}(\nu)$ depends on the experimental setup.

When no sample is in the beam 1, the interferogram $I_o(x)$ is a convolution of $E_1(t)$ of source1 and $E_2(t)$ of source 2. The temporal shapes of $E_1(t)$ and $E_2(t)$ can not be determined in this setup. But the FT of $I_o(x)$ is the product of $E_1(\nu)\, and\, E_2^o(\nu)$, which is well-defined.

When the sample is in the beam 1, $E_1^s(t)$ is the transmitted signal. For semiconductor materials, the complex loss is determined by photoconductivity of the sample which determines the reflection on interface and the absorption due to free carriers, as we will see in following discussion. When the material is not highly-doped, the dispersion of the index of refraction is small within the THz spectrum. Thus the absorption coefficient and dispersion of index can be obtained from the measurement of $I_o(x)$ and $I_s(x)$ by

$$\alpha(\nu) = -\frac{2}{d}\ln L'(\nu), \tag{3.20}$$

and

$$n(\nu) = 1 + \frac{\phi_L'(\nu)}{2\pi d\nu}, \tag{3.21}$$

where d is the thickness of the sample, $L'(\nu)\, and\, \phi_L'(\nu)$ are the modifications of $L(\nu)\, and\, \phi_L(\nu)$ after considering the reflection in the interfaces.

By definition, the complex dielectric constant ε (the response function) is

$$\varepsilon = (n_r + in_i)^2, \tag{3.22}$$

where the real index n_r is just the expression (3.21) and the imaginary index is related to absorption coefficient by

$$n_i = \frac{c\alpha(\nu)}{4\pi\nu}, \tag{3.23}$$

where c is the speed of light in the sample. Generally, the frequency dependence of ε is determined by several factors: (1) interaction with lattice: photon-phonon (optical) scattering; (2) interaction with free carriers: photon-carrier scattering; (3) interaction with bound electrons: resonant and nonresonant transitions excited by photons. The strength of each kind of interaction depends on the property of materials. In the FIR frequency range, the contribution of resonant electronic transitions is shallow donor or exciton transitions. The dephasing time and lifetime of excited states can be obtained using THz technique. The photon-phonon interaction is an interesting phenomena since the FIR photon energy and optical phonon energy are similar. In the THz spectrum (less than 3 THz) and room temperature, these two interactions are not in the resonant region. Thus we only consider the absorption from free carrier scattering. Then ε can be expressed as

$$\varepsilon = \varepsilon_\infty + \frac{i\sigma}{\omega\varepsilon_o}, \tag{3.24}$$

where the functional form of σ is completely general. In the THz region, the Drude model is a good description of the conductivity in semiconductors[3.8]. Then σ(ω) can be generally expressed as

$$\sigma(\omega) = \frac{i\varepsilon_o\omega_p^2}{(\omega + i\Gamma)}, \tag{3.25}$$

where ε_o is the vacuum dielectric constant, Γ is the damping rate, and ω_p is the plasma frequency of the free electron or hole gases. They can be expressed as

$$\Gamma = \frac{e}{m^*\mu}, \tag{3.26}$$

and

$$\omega_p = \sqrt{\frac{Ne^2}{\varepsilon_o m^*}}, \tag{3.27}$$

where m^* is the effective carrier mass, e the electron charge, N the carrier density, and μ the carrier mobility. Thus with the Drude model the carrier density and mobility can be

determined by the static THz spectroscopy. The specific form of the absorption coefficient in the Drude model can be written as a function of wavelength λ as

$$\alpha = \frac{Ne^2 \lambda^2 \Gamma}{m^* 8\pi^2 n_r c^3}. \tag{3.28}$$

Appendix IV: Detector Power Calibration

Liquid He cooled Bolometer

Currently liquid He cooled bolometer with lock in amplifier is the most sensitive power detection system in THz regime. The bolometer entrance is consist of polyethylene window, followed by Winston cone and lower pass filter before it reaches the bolometric material. The Winston cone focuses the incoming radiation. The polyethylene window and the filter are designed to block unwanted background noise. Upon the incident, the bolometric element changes the resistance that directly influences output voltage. While the bolometer is quite sensitive in THz regime comparing to other detectors such as Golay cell and pyroelectric detector, we have found that the vender calibration was not correct. In order to access the efficiency properly, we have calibrated the bolometer. The procedure is as followed. First, a blackbody source, calibrated HeNe laser and other calibrated fiber source are used to confirm a thermal (Coherent LM-10) and the silicon (Coherent LM-2) power detector. Then a pyroelectric detector was calibrated with a fix modulation frequency against calibrated detectors. Based on the vender specification, the spectral response of the pyroelectric detector is assumed uniform up to THz frequency. The bolometer detector is then calibrated to the pyroelectric detector.

Pyroelectric Calibration Procedure

The following procedures were taken to get responsivity of Molectron (Currently under Coherent) Pyroelectric detector (P4-43).

Stanford Research Systems 850 lock-in amplifier.

A ND-OD3 filter was placed in front of HeNe laser by Spectra Physics Model 120S (~4 mW). The power using calibrated detector Newport 1835C with wavelength set at 632.8nm was measured 55 μW. A chopper frequency of 9 Hz was chosen to maximize the responsivity of the pyroelectric detector. A chopper running at 9 Hz and pyroelectric detector output read by SRS 850 was 0.58 V

Responsivity (Power / SRS850 Voltage) = 55 μW / 0.58 V

$= 9.48 \times 10^{-5}$ W/V (Power/ SRS850 Voltage)

Bolometer Calibration Procedure

Bolometer detector by Infrared Laboratory, Inc, Model number HD-3 with amplifier model number LN6-6.

A chopper was set to 100 Hz. THz reading in SRS850 (standard output reading X value) from Bolometer is set to 0.74 V. Bolometer was replaced with Pyroelectric detector. The chopper frequency was reset to 9 Hz. Pyroelectric output in SRS850 read 3.2 mV

Responsivity of Bolometer (Power/ Lock in Voltage) at 100 Hz; Gain = 200

$= 3.2*10^{-3} *9.48 \times 10^{-5} /0.74 = 4.10*10^{-7}$ W/V (Power/SRS850 Voltage)

Assumptions

There are a several assumptions made in above calculations. The first is that the responsivity of pyroelectric detector does not depend on wavelength. The second is the linear responsivity for pyroelectric. The third is that the power collected at the bolometer and the pyroelectric are the same. The sample chopper was used throughout the experiment.

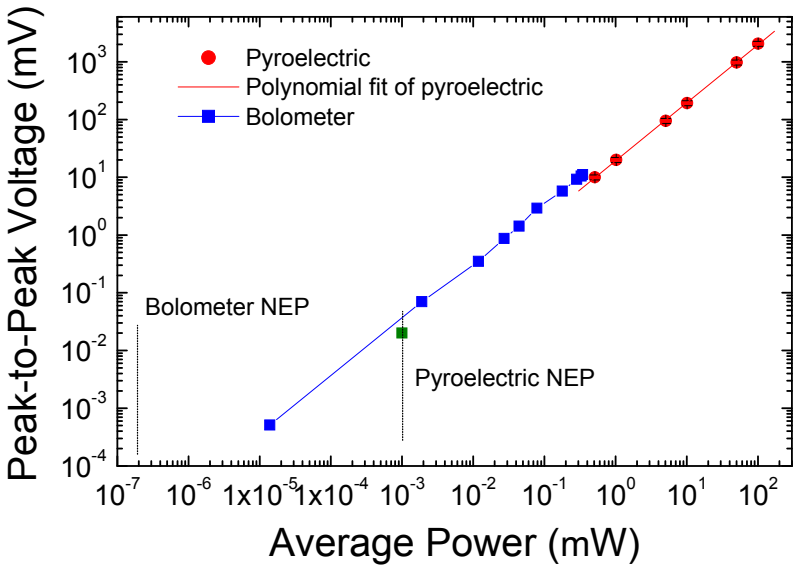

Figure 58. Dynamic range of noise equivalent power for Pyroelectric detector and Bolometer.

Appendix V: Sentaurus Simulation Code

```
File {
      Grid    = "StructureDope_msh.grd"
      Doping  = "StructureDope_msh.dat"

         Plot    = "./Sample_des.dat"
         Output  = "./Sample_des.log"
         Current = "./Sample_des.plt"
         Parameter = "./GaAs.par"

}

Electrode {
         { Name="Anode" Voltage=0.0 Schottky Barrier = 0.55 }
         { Name="Cathode" Voltage=0 Schottky Barrier = 0.55 }

}

Plot {
      Potential Electricfield SpaceCharge
         eDensity hDensity eCurrent hCurrent
         eMobility hMobility eVelocity hVelocity
         AvalancheGeneration

}


Math(Electrode="Anode"){
         Nonlocal(Length=1e-5) *length specified in cm
         }
Math(Electrode="Cathode"){
         Nonlocal(Length=1e-5) *length specified in cm
         }

Math {
         Extrapolate
         Derivatives
         RelerrControl
         IncompleteNewton (UpdateFactor = 0.1 RhsFactor = 1000)

}
```

```
Physics {
        Hydrodynamic
        *PostTemperature
        Fermi
        EffectiveIntrinsicDensity (BandGapNarrowing( OldSlotboom) )
        IncompleteIonization
       Mobility(HighFieldsat(TransferredElectronEffect) Enormal PhuMob DopingDep )


        *Recombination (Avalanche(ElectricField) eAvalanche(CarrierTempDrive)
hAvalanche(Eparallel) CDL Auger(WithGeneration) Band2Band SRH )

        Thermionic

        Traps(Donor Level EnergyMid=0.691 fromCondBand
        Conc=2e16 eXsection=6.7e-16 hXsection=2e-18)

}

Physics (Electrode = "Anode"){BarrierLowering Recombination(eBarrierTunneling
hBarrierTunneling)}
Physics (Electrode = "Cathode"){BarrierLowering Recombination(eBarrierTunneling
hBarrierTunneling)}


Solve {
        Coupled ( Iterations=100 ) { Poisson  }
        Quasistationary ( InitialStep=0.01 Minstep=0.001 MaxStep=1
                Increment=0.2 Goal { Name="Anode" Voltage=200 }
                Plot {Range = (0 1) Intervals=300}) {
                Coupled {Poisson Hole Electron}
                CurrentPlot
         }
}
```

REFERENCES

1 P. H. Siegel, “THz instruments for space”, *IEEE Trans. on Antenna and Propagation,* **55**, v11, 2957 (2007).

2 E. Pickwell and V. P. Wallace, “Biomedical applications of terahertz technology, ”*J. Phys. D: Appl. Phys* **39**, 301 (2006).

3 W. L. Chan, J. D., and D. M. Mittleman, “Imaging with terahertz radiation,”*Reports on Progress in Physics*, **70**, 1325 (2007).

4 M. T. Reiten, D. Grischkowsky and R. A. Cheville, "Properties of surface waves determined via bistatic terahertz impulse ranging," *Appl. Phys. Lett.*, **78**, 1146 (2001).

5 B. Williams, S. Kumar, Q. Hu, and J. Reno,”High-Power terahertz quantum-cascade lasers,” *Electron. Lett.* **42,** 89 (2006).

6 G. P. Williams, “Filing the THz gap-high power sources and applications”, *Rep. Prog. Phys.* **69,** 301 (2006)

7 M. Exter and D. Grischkowsky, “Characterization of an optoelectronic terahertz beam system,” *IEEE Trans. Microwave Theory Tech.*, **38**, 1684, (1990).

8 P. Uhd Jepsen and S. R. Keiding, “Radiation patterns from lens-coupled terahertz antennas”, *Opt. Lett.* **20**, , 807 (1995)

9 D. H. Auston, “Picosecond optoelectronic switching and gating in silicon,” Appl. Phys. Lett. **26**, 101 (1975).

10 A G Davies, E H Linfield and M B Johnston, “The development of terahertz sources and their applications,” *Phys. Med. Biol.* **47** 3679 (2002).

11 P. C. M. Planken, H.J. Bakker, “Towards time-resolved THz imaging”, *Appl. Phy. A*, vol **78**, 465-469 (2004)

12 S. E. Ralph and D. Grischkowsky, “Trap-enhanced electric fields in semi-insulators: The role of electrical and optical carrier injection”, *Appl. Phys. Lett*. **59**, 1972, (1991).

13 A. Dreyhaupt, S. Winnerl, M. Helm, T. Dekorsy, “Optimum excitation conditions for the generation of high-electric-field terahertz radiation from an oscillator-driven photoconductive device”, *Opt. Lett.*. Vol. **31**, 1546-1548 (2006)

14 T. Hattori, K. Egawa, S. Ookuma and T. Itatani, “Intense Terahertz Pulses from Large-Aperture Antenna with Interdigitated Electrodes”, *JJPL*, Vol **45**, 12, L422-L424 (2006)

15 Zhang XC, Auston DH, “Optoelectronic measurement of semiconductor surfaces and interfaces with femtosecond optical”, *Journal of Appl. Phys*. **71** 326 (1992)

16 E H Linfield, A G Davies, M B Johnston, and A Dowd, “Terahertz generation at semiconductor surfaces”, *Central Laser Facility Annual Report 2001/2002*

17 L. Xu, X. –C. Zhang, and D. H. Auston, “Terahertz radiation from large aperture Si p-i-n diodes”, *Appl. Phys. Lett*. **59** (26), 1991

18 A. Leitenstorfer, S. Hunsche, J. Shah, M. C. Nuss, and W. H. Knox, “Detectors and sources for ultrabroadband electro-optic sampling: Experiment and theory”, *App. Phys.* (1999), **74** (11), 1516.

19 N. Sarukura, H. Ohtake, S. Izumida, Z. L. Liu,”High average-power THz radiation from femtosecond laser-irradiated InAs a magnetic field and its elliptical polarization characteristics,” *J. Appl. Phys. (1998), **84**, 654*

20 J.N. Heyman, P. Neocleous, D. Hebert, P. A. Crowell, T. Muller, K. Unterrainer, “Terahertz emission from GaAs and InAs in a magnetic field”, *Phys. Rev. B (*2001**),** **64**, 085202

21 Y. Cai, I. Brener, J. Lopata, J. Wynn, L. Pfeiffer, and J. Federici, “Design and performance of singular electric field terahertz photoconducting antennas” *Appl. Phys. Lett*. **71**, 2076, (1997).

22 Darmo, J. Muller, T. Strasser, G. Unterrainer, K. Le, T. Stingl, A., ”Voltage-controlled intracavity terahertz generator for self-starting Ti : sapphire lasers” *Opt. Lett.* **27** : 1941 (2002).

23 S. R. Andrews, A. Armitage, P. G. Huggard, and A. Hussain, “Optimization of photoconducting receivers for THz spectroscopy”. *Phys. Med. Bio*l., **47**, 3705, (2002).

24 D. Grischkowsky, "Optoelectronic Characterization of Transmission Lines and Waveguides by THz Time-domain Spectroscopy," *J. Sel. Topics Quant. Elec*., Vol. **6**, 1122-1135 (2000)

25 G. S. Smith, *An Introduction to Classical Electromagnetic Radiation* (Cambridge University Press, Cambridge, 1997)

26 W. Sha, J.-K. Rhee, T. B. Norris, and W. J. Schaff, “Transient carrier and field dynamics in quantum-well parallel transport: From the ballicstic to the quasiequilibrium regime,” *IEEE J. Quantum Electron*. **28**, 2445 (1992).

27 J. E. Pederson, V. G. Lyssenko, J. M. Hvam, P. U. Jepsen, S. R. Keiding, C. B. Sorensen, and P. E. Lindelof, ”Ultrafast local field dynamics in photoconductive THz antennas,” *Appl. Phys. Lett* **62**, 1256 (1993).

28 J. Shan and T. F. Heinz, Terahertz radiation from semiconductors,” *Topics Appl. Phys.* **92**, 1 Springer Verlag, (2004).

29 R. Kersting, K. Unterrainer, G. Strasser, H. F. Kauffmann, E. Gornik, “Few-cycle THz emission from cold plasma oscillations,” *Phys. Rev. Lett*. **79**, 3038, (1997).

30 G. Rodriguez and A. J. Taylor, “Screening of the bias field in terahertz generation from photoconductors,” Opt. lett. **21** ,14, 1046 (1996)

31 J. T. Darrow, X.-C. Zhang, and D. H. Auston, “Power Scaling of larage-aperture photoconductive antennas”, *Appl. Phys. Lett.* **58**

32 J. T. Darrow, X, Zhang, D. H. Auston, J. D. More, “ Saturation Property of Large-Aperture Photoconducting Antennas” IEEE Journal of Quantum Electronics, **28**, no.6 (1992).

33 C. W. Siders, J. L. W. Siders, and A. J. Taylor, S.-G. Park, M. R. Melloch, and A. M. Weiner, “Generation and characterization of terahertz pulse trains from biased, large-aperture photoconductors” *Opt Lett*., **24**, No 4, 241-243 (1999)

34 P. K. Benicewicz, J. P. Roberts, and A. J. Taylor, “Scaling of terahertz radiation from large-aperture biased photoconductors”, *J. Opt. Soc. Am. B*, **11**, 2533, (1994).

35 D.J. Kane and R. Trebino, ``Characterization of Arbitrary Femtosecond Pulses Using Frequency-Resolved Optical Gating," *IEEE J. Quan. Electron.*, vol. 29, pp. 571-579 (1993)

36 R. W. Boyd, “Nonlinear Optics,” 2nd Ed, Academic Press, (2003).

37 Y. Cai, I. Brener, J. Lopata, J. Wynn, L. Pfeiffer, and J. Federici, “Design and performance of singular electric field terahertz photoconducting antennas” Appl. Phys. Lett. 71, 2076, (1997).

38 G. Zhao, R. N. Schouten, N. van der Valk, W. Th. Wenckebach, and P. C. M. Planken “Design and performance of a THz emission and detection setup based on a semi-insulating GaAs emitter” Rev. Sci. Instrum. 73(4) 1715, (2002).

39 E. H. Rhoderick and R. H. Williams, "Metal_semiconductor Contacts", (Clarendon Press, Oxford), 2nd Ed, 1988

40 M. Murakami, "Development of Ohmic contact materials for GaAs integrated circuits," Material Science Reports 5 (1990) 273-317.

41 S. M. Sze,"Metal-Semiconductor Contacts", in *Physics of Semiconductor Devices*, 2nd Ed. 1981, pp 250-254

42 P.M. Solomon and K. Weiser, "On the rectifying ability of a p-type semi-insulating junction", J. Appl. Phys. **70** (10), 1991, pp 5408-5419

43 N. Braslau, "Alloyed ohmic contacts to GaAs,' J. Vac. Sci. Technol., 19(3), 803 (1981).

44 Zheng, "Shallow ohmic contact formation by sequential deposition of Pd/AuGe/Ag/Au on GaAs and rapid thermal annealing," J. Appl. Phys. **71**(7), April, 3566 (1992)

45 SENTAURUS Device User's Manuals, Synopsys (2006)

46 C. Groves, R. Ghin, J. P. R. David an dG. J. Rees, " Temperature Dependence of Impact Ionization in GaAs", IEEE Electron device **(50)** 10 Oct 2003, p2027.

47 S. Coleman, D. Grischkowsky, "Parallel plate THz Transmitter," *Appl. Phys Lett.* 84**,** 654, (2004).

48 J. H. Kim, A. Polley, S. E. Ralph, "Efficient photoconductive terahertz source using line excitation" *Opt. Lett.* **30**, 2490 (2005)

49 D. You, R. R. Jones, P. H. Bucksbaum, D. R. Dykaar, "Generation of high-power sub-single-cycle 500-fs electromagnetic pulse," *Opt. Lett.* **18**, 290, (1993).

50 G. Zhao, R. N. Schouten, N. van der Valk, W. Th. Wenckebach, and P. C. M. Planken, Rev. Sci. Instrum. **73** (4), 1715 (2002).

51 P. Uhd Jepsen, R.H. Jacobsen, and S.R. Keiding, J. Opt. Soc. Am. B **13**, 2424 (1996).

52 J. T. Darrow, X. –C. Zhang, D. H. Auston, and J. D. Morse, IEEE J. Quantum Electron. **28**, 1607 (1992).

53 K. Bløtekjær, "Transport equations for electrons in two-valley Semiconductors," *IEEE Trans. Electron Devices.* **17**, 38, (1970).

54 K. Bløtekjær, IEEE Trans. Electron Devices. **17**, 38 (1970).

55 D. L. Woolard, R.J. Trew and M. A. Littlejohn, “Hydrodynamic hot-electron transport model with Monte Carlo-generated transport parameters,” *Solid-State Electronics*, **31**, 571, (1988).

56 S E. Ralph and D. Grischkowsky, “THz spectroscopy and source characterization by optoelectronic interferometry,” *Appl. Phys. Lett*. **60**, 1070-1072 (1992)

57 M. van Exter, Ch. Fattinger and D. Grischkowsky, “TeraHz Time Domain Spectroscopy of Water Vapor”, *Optics Letters*, Vol.**14**, 1128-1130 (1989)